Springer ThesesRecognizing Outstanding Ph.D. Research

Daniele Gaggero

Cosmic Ray Diffusion in the Galaxy and Diffuse Gamma Emission



Springer Theses

Recognizing Outstanding Ph.D. Research

For further volumes: http://www.springer.com/series/8790

Aims and Scope

The series "Springer Theses" brings together a selection of the very best Ph.D. theses from around the world and across the physical sciences. Nominated and endorsed by two recognized specialists, each published volume has been selected for its scientific excellence and the high impact of its contents for the pertinent field of research. For greater accessibility to non-specialists, the published versions include an extended introduction, as well as a foreword by the student's supervisor explaining the special relevance of the work for the field. As a whole, the series will provide a valuable resource both for newcomers to the research fields described, and for other scientists seeking detailed background information on special questions. Finally, it provides an accredited documentation of the valuable contributions made by today's younger generation of scientists.

Theses are accepted into the series by invited nomination only and must fulfill all of the following criteria

- They must be written in good English.
- The topic should fall within the confines of Chemistry, Physics, Earth Sciences, Engineering and related interdisciplinary fields such as Materials, Nanoscience, Chemical Engineering, Complex Systems and Biophysics.
- The work reported in the thesis must represent a significant scientific advance.
- If the thesis includes previously published material, permission to reproduce this must be gained from the respective copyright holder.
- They must have been examined and passed during the 12 months prior to nomination.
- Each thesis should include a foreword by the supervisor outlining the significance of its content.
- The theses should have a clearly defined structure including an introduction accessible to scientists not expert in that particular field.

Daniele Gaggero

Cosmic Ray Diffusion in the Galaxy and Diffuse Gamma Emission

Doctoral Thesis accepted by GALILEO GALILEI School of Graduate Studies in Basic Science, University of Pisa, Italy



Author
Dr. Daniele Gaggero
Instituto Nazionale di Fisica Nucleare
(INFN)—Sezione di Pisa
Largo Pontecorvo 3
Pisa 56127
Italy

Supervisors
Dr. Dario Grasso
Instituto Nazionale di Fisica Nucleare
(INFN)—Sezione di Pisa
Largo Pontecorvo 3
Pisa 56127
Italy

Prof. Dr. Ronaldo Bellazzini Instituto Nazionale di Fisica Nucleare (INFN)—Sezione di Pisa Largo Pontecorvo 3 Pisa 56127 Italy

ISSN 2190-5053 ISSN 2190-5061 (electronic) ISBN 978-3-642-29948-3 ISBN 978-3-642-29949-0 (eBook) DOI 10.1007/978-3-642-29949-0

Springer Heidelberg New York Dordrecht London

Library of Congress Control Number: 2012939123

© Springer-Verlag Berlin Heidelberg 2012

This work is subject to copyright. All rights are reserved by the Publisher, whether the whole or part of the material is concerned, specifically the rights of translation, reprinting, reuse of illustrations, recitation, broadcasting, reproduction on microfilms or in any other physical way, and transmission or information storage and retrieval, electronic adaptation, computer software, or by similar or dissimilar methodology now known or hereafter developed. Exempted from this legal reservation are brief excerpts in connection with reviews or scholarly analysis or material supplied specifically for the purpose of being entered and executed on a computer system, for exclusive use by the purchaser of the work. Duplication of this publication or parts thereof is permitted only under the provisions of the Copyright Law of the Publisher's location, in its current version, and permission for use must always be obtained from Springer. Permissions for use may be obtained through RightsLink at the Copyright Clearance Center. Violations are liable to prosecution under the respective Copyright Law.

The use of general descriptive names, registered names, trademarks, service marks, etc. in this publication does not imply, even in the absence of a specific statement, that such names are exempt from the relevant protective laws and regulations and therefore free for general use.

While the advice and information in this book are believed to be true and accurate at the date of publication, neither the authors nor the editors nor the publisher can accept any legal responsibility for any errors or omissions that may be made. The publisher makes no warranty, express or implied, with respect to the material contained herein.

Printed on acid-free paper

Springer is part of Springer Science+Business Media (www.springer.com)

Supervisors' Foreword

The original work presented in this thesis constitutes an important contribution to modern Cosmic Ray (CR) physics, made during one of the most exciting periods of this field.

The first part introduces a new high performing numerical code (DRAGON) to model CR propagation in our Galaxy. The code is then exploited to perform a combined analysis of the CR light nuclei and antiprotons data enabling to constrain their propagation properties with unprecedented accuracy.

The second part is dedicated to a detailed theoretical interpretation of a set of crucial experimental results on cosmic electron and positron spectra which appeared recently (PAMELA and Fermi-LAT most noticeably). These new data have baffled our earlier understanding of CR science. The author convincingly argues, using also the tools developed in the first part of the thesis, for the evidence of a new spectral component which could arise from local astrophysical sources like pulsars or by Dark Matter annihilation or decay. Both scenarios are described in detail and their relative merits discussed in-depth.

The thesis is very mature, the methods carefully explained and presented very clearly and completely, providing enough detail to be an important reference document for any future work in this area.

Pisa, Italy, 6 March 2012

Dr. Dario Grasso Prof. Dr. Ronaldo Bellazzini

Acknowledgments

I really want to thank first of all my supervisor Dario Grasso who followed me in these years with great care, patience, and expertise. I am also indebted to my collaborators and friends who shared with Dario and me the hard work and efforts of these years and gave a major contribution to all the results that I presented in this work: Giuseppe Di Bernardo, Carmelo Evoli, Luca Maccione. Without them most of this work would not have been possible.

A great "thank you" goes to all the Fermi collaboration, in particular the Pisa group guided by Ronaldo Bellazzini. It was really stimulating to work with them in such an important experiment and in a very prolific period for the entire astroparticle field.

I dedicate this work to my family and all the friends in Pisa and Viareggio who permitted me to really enjoy the period of the Graduate Studies with countless evening walks, beers, hikes, trips, dinners....

Contents

| I | Intr | oduction | J |
|---|------|----------------------------------------------------------|------|
| | Refe | erences | 5 |
| 2 | Cos | mic Ray Diffusion in the Galaxy | 7 |
| | 2.1 | Introduction | 7 |
| | 2.2 | History of CR Measurements | 7 |
| | 2.3 | The Interstellar Environment of Our Galaxy | ç |
| | | 2.3.1 Introductory Considerations | ç |
| | | 2.3.2 The Interstellar Gas | 10 |
| | | 2.3.3 SNRs and Pulsars | 17 |
| | | 2.3.4 The Magnetic Field | 19 |
| | 2.4 | CR Propagation: The Diffusion Equation | 21 |
| | | 2.4.1 Introductory Considerations | 21 |
| | | 2.4.2 Diffusion Equation | 22 |
| | Refe | erences | 26 |
| 3 | Nun | nerical Codes that Solve the CR Diffusion Equations | 29 |
| J | 3.1 | Numerical Approach to the Solution of CR Diffusion | ر کے |
| | 5.1 | Equation | 29 |
| | 3.2 | DRAGON Code: A Detailed Description | 31 |
| | | erences | 33 |
| | KCI | itelices | 5. |
| 4 | Pro | pagation of CR Nuclei: Our Results | 35 |
| | 4.1 | Introduction | 35 |
| | 4.2 | How to Test Diffusion Models: B/C, Antiprotons. Previous | |
| | | Results | 35 |
| | 4.3 | Our Maximum Likelihood Analysis on B/C | |
| | | and Antiproton Data | 42 |
| | | 4.3.1 Our Method and Results | 40 |

x Contents

| | | 4.3.2 Discussion on B/C Analysis | 47 |
|---|------|------------------------------------------------------------|-----|
| | | 4.3.3 Discussion on \bar{p}/p and Joint Analysis | 49 |
| | 4.4 | Our Preferred Model | 50 |
| | 4.5 | Minimal and Maximal Models | 51 |
| | 4.6 | Discussion | 53 |
| | | 4.6.1 Comparison with Other Results | 53 |
| | | 4.6.2 Systematic Uncertainties | 55 |
| | Refe | erences | 56 |
| 5 | The | Leptonic Field | 59 |
| | 5.1 | Introduction | 59 |
| | 5.2 | Propagation of CR Electrons | 59 |
| | 5.3 | Pre-Fermi Measurements of CR Electron | |
| | | and Positron Spectrum | 64 |
| | 5.4 | Astrophysical Explanations of the Pre-Fermi Leptonic | |
| | | Excesses | 66 |
| | 5.5 | Dark Matter Interpretation | 69 |
| | | 5.5.1 Introduction | 69 |
| | | 5.5.2 Interpretation of PAMELA and ATIC Data | 72 |
| | 5.6 | Fermi Measurement of CR Electron+Positron Spectrum | 74 |
| | 5.7 | Interpretation of 2009 Dataset | 79 |
| | | 5.7.1 Single Component Models | 79 |
| | | 5.7.2 Pulsar Models | 83 |
| | | 5.7.3 Dark Matter Models | 88 |
| | | 5.7.4 Comparison with Other Interpretations | 90 |
| | 5.8 | Interpretation of 2010 Dataset and Anisotropy Upper Limits | 93 |
| | | 5.8.1 Introduction | 93 |
| | | 5.8.2 Single Component Models | 93 |
| | | 5.8.3 Double Component Models | 98 |
| | | 5.8.4 Contribution from Nearby Pulsars and SNRs | 99 |
| | | 5.8.5 Compatibility with Upper Limits on Anisotropy | 103 |
| | 5.9 | Fermi Preliminary Measurement of CR Positron Spectrum | 105 |
| | Refe | erences | 107 |
| 6 | Diff | use Gamma Ray Emission from the Galaxy | 111 |
| | 6.1 | Outline | 111 |
| | 6.2 | Introduction | 111 |
| | | 6.2.1 How Diffuse γ Rays are Produced | 111 |
| | | 6.2.2 Brief Overview of Pre-Fermi γ-Ray Observations | 113 |
| | | 6.2.3 Open Problems After EGRET Era | 113 |
| | 6.3 | Fermi-LAT View of Gamma-Ray Sky | 114 |
| | 6.4 | Spatial-Dependent Diffusion Coefficient as a Solution | |
| | | to the Gradient Problem | 117 |

Contents xi

| | 6.4.1 The Idea | 117 | | | | | |
|---------------------------------------------------------------|-----------------------------------------------|-----|--|--|--|--|--|
| | 6.4.2 The Method | 118 | | | | | |
| | 6.4.3 Results | 119 | | | | | |
| | References | 125 | | | | | |
| 7 | Conclusions and Future Plans | 127 | | | | | |
| Appendix A: The Diffusion Equation in Cylindrical Coordinates | | | | | | | |
| Appendix B: DRAGON Code: A Description | | | | | | | |
| Aj | ppendix C: Solution of the Transport Equation | | | | | | |
| | for a Pulsar-Like Source | 143 | | | | | |
| In | dex | 145 | | | | | |

Chapter 1 Introduction

Cosmic Rays (CRs) are energetic particles that continuously hit the top of the Earth atmosphere at the considerable rate of $\sim 10^4$ m⁻² s⁻¹. The exact composition depends on which part of the spectrum is considered, but we can say that approximately 86% of these particles are protons, 11% are alpha articles, 1% consists of stable nuclei, up to Uranium, then 2% are electrons and a non negligible fraction (about 1%) consists of antiparticles (positrons and antiprotons).

The energetic spectrum is non-thermal and—for the hadronic part—almost featureless from ~ 1 GeV to the highest recorded energies (about 10^{20} eV): it can be well described by a power-law with spectral index equal to -2.7 up to $\simeq 10^{15}$ eV (the so-called "knee"); above the knee a steepening of the slope is observed, up to $\sim 10^{18}$ eV (the "ankle") where a hardening is detected; it is generally believed that the ankle traces the change from CRs of Galactic origin to CRs coming from outside our Galaxy.

The study of Cosmic Rays was a very important and prolific research field in the first half of twentieth century since it permitted the discovery of many new particles: in fact, CRs interact with the atmosphere of the Earth and produce showers of secondary particles, such as pions, muons, positrons, which could be detected and identified for the first time.

Nowadays, CR study is still a very relevant sector because, as I will show in detail, there are many open problems regarding their origin and properties, and the open questions in this field are related to many interesting astrophysical issues and with some of the most intriguing puzzles of modern physics, such as the nature of Dark Matter.

The standard picture that is commonly accepted by the scientific community can be summarized in the following way. CRs from 1 GeV to the knee originate in our Galaxy and are accelerated in Supernova Remnants via first-order Fermi mechanism; the energy spectrum that comes out of this phase (the *injection*) is a power-law. Then, the accelerated particles propagate in the insterstellar medium, and are deflected by the galactic magnetic field (GMF); since the GMF has a turbulent component whose amplitude is comparable with the regular one, they follow an erratic path and their

2 1 Introduction

motion is well described by a diffusion equation: in fact the correlation length is smaller than the Larmor radius; since the particles diffuse more quickly at higher energies, the effect of diffusion is to steepen the spectrum. During their flight, these particles may also be stochastically re-accelerated by the interaction with Alfvén waves¹ and drifted by convective winds, these effects being greater at lower energies; moreover, the leptonic part (electrons and positrons) suffers severe energy losses due to synchrotron emission and Inverse Compton scattering on the Interstellar Radiation Field (ISRF), while the hadronic part interacts with interstellar gas and produces by spallation lighter nuclei (which are called secondary CRs when propagation in the Galaxy is considered, and must not be confused with secondary particles that are produced in the atmosphere).

Once they reach the Solar System, CRs interact with the solar wind: this effect is called "solar modulation" and consists of a deflection through the magnetic field which is frozen into the solar wind plasma, an adiabatic energy loss and a convection by the outward motion of the particle stream which constitutes the wind. This effect depends on the solar cycle and originates an anticorrelation between the flux of CRs and the sunspots number count; of course it affects the less energetic part of the spectrum, being almost negligible above 10 GeV.

At last, CR particles arrive in the proximity of the Earth, where they can be detected by space (Fermi-LAT, PAMELA, the forthcoming AMS-02) or balloon experiments (CREAM, TRACER, and many others).

Many aspects of this picture are still unclear.

- Origin. Although the FIRST order Fermi acceleration mechanism mentioned above appears the most likely for many reasons, direct evidence of hadronic acceleration in a SNR is still missing. Moreover, little is known of the spectrum that should emerge from the acceleration, both for the hadronic and for the leptonic part; however, the leptonic spectrum is expected to be steeper due to energy losses at the source.
- **Propagation**. Many aspects of CR diffusion are still unclear; in particular, the absolute value and energy dependence of the diffusion coefficient are not known yet with the desired precision; also the effectiveness of reacceleration and convection is not known. In general, all low-energy effects, including solar modulation, due to the large amount of free parameters involved in their description, are still poorly understood. That is the reason why it is interesting to look at high energies, where the dominant mechanism that acts is diffusion and it is easier to build theoretical models, but—on the other hand—since at higher energies the fluxes are lower, measures are affected by larger statistical uncertainties and can provide less strong constraints on models themselves. Due to all these difficulties, it has been quite hard so far to create a comprehensive model of CR propagation which fits all observed fluxes: for example, an important open problem is the compatibility between light nuclei and antiproton measurements (see for example [1]).

¹ Alfvén waves are travelling oscillations of ion density and magnetic field in a magnetized plasma. They are present in the ionized component of the interstellar medium.

1 Introduction 3

I will describe in the first part of this thesis work how we succeeded in building a comprehensive model which provides a good fit of most CR light nuclei and antiproton spectra making use of a new numerical code called DRAGON designed by our group to solve the CR diffusion equation and compute all the relevant processes (spallation, energy losses) that are involved in CR propagation. The model parameters were determined through a combined maximum likelihood analysis based on light nuclei and antiproton-to-proton ratio data; the analysis focused on the high-energy part of the measurements, following a very different strategy with respect to the previous analyses that can be found in the literature.

- Interaction with Heliosphere. The details of the interaction of Cosmic Rays with solar wind is a challenging topic: it is very important because it helps to explain the low-energy part of the observed CR fluxes. Currently, most calculations are made in the *force-field* approximation (Gleeson and Axford 1968 [2]) in which a single free parameter is involved, the modulation potential, whose value is fixed by comparison with observed fluxes.
- Interaction with Earth atmosphere. Even if I will not go through these issues, it is interesting to mention that the interaction with the atmosphere is a wide field of research, since CRs are believed to be involved—as catalyzers—in cloud formation, and also in the development of lightings. Connections with climatology have also been argued, and this is currently a hot matter of debate.
- **Signals of new physics**. Part of CR fluxes that reach the Earth may arise from exotic processes, different from those described above.

This intriguing possibility is supported in particular by Particle Dark Matter models which predict the existence of weakly interacting particles that constitute the so called *dark mass* of our Galaxy, i.e., the portion of galactic matter which does not radiate, whose presence is inferred from dynamical observation and whose nature is still unknown. These particles might be indirectly revealed because, through annihilation or decay, they should convert into ordinary particles which should add to the "standard" cosmic rays originating from Supernovae.

This possibility has been considered with particular attention in the last 3 years, since several experiments reported relevant excesses of some components of CR flux with respect to model predictions: the debate that arose from these measurements was particularly exciting.

First of all, in 2008, ATIC observed [3] a sharp spectral feature around 500 GeV in the electron+positron spectrum. A great number of papers were written in that year to explain the nature of this excess, but such feature was not confirmed by Fermi-LAT, which published in May, 2009 [4] a measure of the electron+positron spectrum of unprecedented accuracy, marking a very important point in the history of this kind of measure: Fermi-LAT spectrum appeared almost featureless in a wide range (from 20 GeV to 1 TeV), but considerably harder than previous measurements, therefore still showing an excess at high energy with respect to model predictions, whose parameters were tuned on older measurements. The measure was then refined and extended to lower energy in 2010 [5].

On the positron side, PAMELA collaboration observed [6] a rising positron-toelectron ratio; this rise was recently confirmed by the Fermi collaboration too. 4 1 Introduction

This kind of behaviour is in strong contrast with models: in fact, in a scenario in which positrons are created as secondary products by the interaction of primary CR nuclei with interstellar gas, the positron-to-electron ratio should be decreasing with energy, unless one assumes a very steep electron injection spectrum, hardly compatible with pre-Fermi data and now ruled out by Fermi-LAT measurements. All these "excesses" were interpreted by many authors as indications of extra primary sources of electrons and/or positrons, either of astrophysical nature (e.g. pulsars) or exotic (Dark Matter annihilation or decay).

I will discuss these different scenarios with particular emphasis on the interpretation of Fermi-LAT dataset which, due to the high statistics and the precise evaluation of systematic effects, appears as the most reliable. I will show in detail what we discussed in our publications that followed Fermi-LAT measurement [7]: we found that a simple phenomenological model, in which a primary extra component of electrons and positrons is added to a diffuse conventional emission, is compatible with all the existing observations (including recent measurements of upper limits on CRE anisotropy reported by Fermi-LAT).

Concerning the nature of this extra-component, the debate is still open. We pointed out that, under simple assumptions, the observed pulsars—that are known as electron+positron pair emitters—are natural candidates; on the other hand, the hypothesis of a Dark Matter origin for the extra electrons and positrons is losing part of its appeal for the reasons I will explain in detail in this work, but it remains a fascinating possibility which must not be considered ruled out yet.

It is important to point out that all these open problems require a multi-messenger approach to be solved: i.e., it is important to look not only at CR charged particles, but also at secondary radiation originating from CRs through various mechanism such as synchrotron, bremmstrahlung, Inverse Compton, decay of pions produced via interaction with IS gas.

In particular, gamma-rays and radio waves can help to test model predictions. In this perspective Fermi-LAT mission has a crucial role: the high-statistics full sky gamma-ray maps released by Fermi collaboration cover a wide energy range (from the MeV region up to hundreds of GeV) and are a very important tool to test CR propagation models since the diffuse gamma emission traces CR distribution throughout the Galaxy and not only at Solar System position.

An important open problem that already existed in pre-Fermi era (when COSB and more recently EGRET data were released) concerning modelling of diffuse gamma-rays is the so called *gradient problem*. The gradient problems consist in the discrepancy between the Galactic distribution of emissivity per H atom, which is a measure of the CR flux distribution, and the observed pulsar distribution (which traces CR sources) that turns out to be much steeper. The problem is still present in Fermi-LAT data and several explanations have been proposed by many authors (e.g. a very large diffusion halo, a flatter CR source distribution in the outer Galaxy, the presence of a convective wind); I will show that the assumption of a spatially varying diffusion coefficient, as expected by simple physical considerations, may provide a natural solution to the problem.

1 Introduction 5

In the forthcoming years other developments are expected, as new experiments will start their activity: in particular, AMS-02 space mission will be very important since it will be able to distinguish between electrons and positrons and therefore confirm PAMELA claim of a positron excess.

Of course, also currently operating satellite missions, i.e., Fermi-LAT and PAMELA, will release new and more accurate data: in conclusion, exciting times will arrive for CR studies in the near future.

References

- A.W. Strong, I.V. Moskalenko, V.S. Ptuskin, Cosmic-ray propagation and interactions in the galaxy. Annu. Rev. Nucl. Part. Sci. 57, 285–327 (2007)
- L.J. Gleeson, W.I. Axford, Solar modulation of galactic cosmic rays. Astrophys. J. 154, 1011 (1968)
- J. Chang et al. [ATIC collaboration], An excess of cosmic ray electrons at energies of 300–800GeV. Nature 456, 362–365 (2008)
- 4. A.A. Abdo et al. [Fermi Collaboration], Measurement of the cosmic ray $e^+ + e^-$ spectrum from 20GeV to 1TeV with the fermi large area telescope. Phys. Rev. Lett. **102**(18), 181101 (2009)
- M. Ackermann et al. [Fermi Collaboration], Fermi LAT observations of cosmic-ray electrons from 7 GeV to 1 TeV. Phys. Rev. D 82(9), 092004 (2010)
- O. Adriani et al. [PAMELA Collaboration], An anomalous positron abundance in cosmic rays with energies 1.5–100 GeV. Nature 458, 607–609 (2009)
- D. Grasso, S. Profumo, A.W. Strong, L. Baldini, R. Bellazzini, E.D. Bloom, J. Bregeon, G. Di Bernardo, D. Gaggero, N. Giglietto, T. Kamae, L. Latronico, F. Longo, M.N. Mazziotta, A.A. Moiseev, A. Morselli, J.F. Ormes, M. Pesce-Rollins, M. Pohl, M. Razzano, C. Sgro, G. Spandre, T.E. Stephens, On possible interpretations of the high energy electron-positron spectrum measured by the fermi large area telescope. Astropart. Phys. 32, 140–151 (2009)

Chapter 2 Cosmic Ray Diffusion in the Galaxy

2.1 Introduction

In this chapter I will describe the physics that stands behind the problem of CR propagation.

- Since the battlefield in which CR propagation takes place is the interstellar medium (ISM) of our Galaxy, I will first present a complete description of the Galactic environment and its components, with particular attention to the interstellar gas, the magnetic field (related to CR diffusion and spallation) and the distribution of pulsars and Supernova Remnants (related to CR origin); I will point out the deep interplay that exist between these components that continuously interact one another: the gas triggers star formation, massive stars quickly generate Supernova explosions that accelerate CRs, the gas returns back again in the ISM and the released energy triggers the turbulence that is responsible of the CR random walk.
- With this scenario in mind, I will treat in a formal way the problem of CR propagation in the Galactic plasma as a kinetic physics problem and I will show that the interaction with CRs with the magnetised medium that permeates the Galaxy is naturally described by a diffusion-reacceleration equation.

2.2 History of CR Measurements

It took almost 40 years to understand what Cosmic Rays actually are.

The first signature of their existence was discovered in 1912 by Victor Hess, who was awarded with the Nobel prize for that. Hess observed that the level of ionisation in the atmosphere decreased with elevation up to about 1,000 m (as expected if the only source of ionizing radiation were natural radioactivity on Earth surface) but, above that altitude, it increased considerably, and at \simeq 5,000 m he measured a value several times that observed at sea level: his conclusion was that there was some kind of unknown high energy radiation penetrating the atmosphere from outer space. His

discovery was confirmed by Robert Millikan in 1925, who gave the radiation the name *Cosmic Rays* (CRs).

For many years after this important discovery the cosmic origin of the radiation was in doubt: the increased ionisation rate could be due, for example, to some kind of radioactive emanation from the upper atmosphere. Moreover, the radiation was believed to consist of γ rays, since at that time gamma radiation was believed to be the most penetrating.

Only after the discovery of the geomagnetic effect in 1927 it was clearly shown that CRs were charged particles. A complete picture of the composition of CRs was obtained at the end of the 1940s, when it was clear that they were mainly composed of protons, that all heavier nuclei were present in minor quantities, and that also relativistic electrons contributed to the radiation in a quantity that did not exceed 1%.

During the 1930s and the 1940s particle physicists were very interested in CRs and several new particles were discovered in the cosmic radiation, e.g. the positron (1932, Carl Anderson) and the muon (1936, Carl Anderson); on the other hand, the importance of CRs for astrophysics was not completely understood and little was known on their origin.

Enrico Fermi gave a very important contribution to the Astrophysics of Cosmic Rays when he proposed in 1949 a hypothesis on their origin [1]. The idea is that charged particles may be reflected by the moving interstellar magnetic fields either gaining or losing energy, depending on whether the magnetic "mirror" is approaching or receding. Since in a typical environment the probability of a head-on collision is greater than a head-tail one, the particles would, on average, be accelerated. This random process is now called *second-order Fermi acceleration* because the mean energy gain per bounce depends on the square of the mirror velocity.

In 1977 theorists showed that Fermi acceleration by Supernova remnant shocks is particularly efficient, because in this case the motions are not random. In this new mechanism, a charged particle ahead of the shock front can pass through the shock and then be scattered by magnetic inhomogeneities behind it; the particle gains energy from this bounce and comes back across the shock, where it can be scattered by magnetic inhomogeneities ahead of the shock. This enables the particle to bounce back and forth again and again, gaining energy each time. Because the mean energy gain depends linearly on the shock velocity, this process is now called *first-order Fermi acceleration* and is believed to be the mechanism that permits CRs to reach the very high energies recorded by the experiments.

Another important step forward was in the early 1950s when the synchrotron nature of a large part of cosmic radio emission was established: as a result, it became possible to obtain information of the leptonic component of CRs through the Galaxy: in this way the connection between CR science, Astrophysics and Astronomy was strengthened by a large amount.

In more recent times, CR Astrophysics has evolved a lot, and CR propagation has been studied extensively through numerical simulations; moreover, the development of gamma astronomy with the pioneering COS-B mission (1975), the very important EGRET satellite mission (1991–2000) and now Fermi-LAT (launched in 2008 and

still operating) permitted to obtain more and more detailed maps of the Galaxy in gamma rays, tracing therefore the CR interactions through the Galaxy.

Nowadays, CRs are considered with interest also by particle physicists once again. In fact one of the most fascinating open problems in Physics is the existence of Particle Dark Matter, a hypothesized gas of neutral weakly interacting particles that would account for the unobserved mass of the Galaxy and can only be inferred from dynamical calculations: many authors believe that the signature of the existence of these new particles can be found in CR spectra. This issue is currently under debate; a Dark Matter interpretation of CR measurements is today less appealing than a couple of years ago for many reasons (I will be more precise in the forthcoming chapters); nevertheless, this possibility increased the interest on a problem which is relevant on its own: the accurate and self-consistent prediction of all observed fluxes of CR electrons, positrons, antiprotons and light nuclei of astrophysical origin; indeed, any excess with respect to these predictions can be easily interpreted in terms of annihilation or decay of exotic particles into standard particles, although it is quite difficult to disentangle such an explanation from alternative scenarios of astrophysical origin.

In order to predict CR fluxes and spectra it is crucial to understand the CR propagation in the Galactic magnetic field, the distribution of CR sources, and therefore a detailed knowledge of the structure of the Galaxy is required. In the following paragraph I will present a short review on the main properties of our Galaxy together with a brief history of the most important discoveries in Galactic astronomy and astrophysics. Then, in Sect. 2.4 I will derive the equations describing CR propagation in such an environment.

2.3 The Interstellar Environment of Our Galaxy

2.3.1 Introductory Considerations

The word *Galaxy* derives from the ancient Greek term $\gamma\alpha\lambda\alpha\xi i\alpha\varsigma$ literally meaning *Milky* (so it is really a synonym of Milky Way): in fact, it appeared to the naked eyes of a terrestrial observer as a faint band of diffuse white light stretching all the way around the sky. For a great number of centuries little was known about its actual nature, which nevertheless was guessed by many philosophers and astronomers: e.g. the Greek philosopher Democritus (450–370 B.C.) proposed that it could consist of distant stars, and the Andalusian astronomer Ibn Bājjah (Twelfth century) said that it was made up of many stars that almost touch one another. However, the actual proof of the actual composition of the Milky Way came in 1610 when Galileo Galilei with the help of the telescope finally discovered that it is actually composed of a very large number of faint stars.

A more refined comprehension of the structure of our Galaxy came much later, when Harlow Shapley (1885–1972) began to study globular clusters and noticed

that, unlike ordinary stars, they do not spread uniformly along the Milky Way, but concentrate instead towards the direction of the Sagittarius; he also found that they have a roughly spherical distribution, the center of which, he argued, should approximately coincide with the center of the Galaxy itself: these observations led him to the important conclusion that the Sun is located very far from the Galactic center. Further kinematic studies by Bertil Lindblad (1895–1965) and Jan Oort (1900–1992) supported this result.

Nowadays, it is commonly accepted that we live within a very large system of stars called the Galaxy, similar to billions of other similar systems existing in the observed Universe. The Galaxy consists of a thin disk with radius \simeq 25–30 kpc and thickness \simeq 400–600 pc, and the faint band that originated the term Milky Way is simply the disk seen transversally; there is also a spherical system which is itself composed of a bulge with radius $\simeq 2-3$ kpc and a dark matter halo extending out to more than 30 kpc away from the center. The position of our Solar System is in the disk, $\simeq 15$ pc above the midplane and $\simeq 8.5$ kpc away from the center (see [2] and references therein). The stars belonging to the disk rotate around the center in nearly circular orbits; at the Sun's orbit, the rotation velocity is $\simeq 220 \,\mathrm{km/s}$: such a speed corresponds to a rotation period of about 240 million years. Disk stars also have a velocity dispersion that causes them to oscillate about a perfectly circular orbit, both in the Galactic plane and in the vertical direction. Instead, the stars that are in the bulge and in the halo rotate more slowly and often have eccentric trajectories. Radio-astronomical observations of interstellar hydrogen indicate that the Milky Way possesses a spiral structure: this is known since the pioneering works of J. Oort [3]; moreover, recent infrared images of the Galactic center region clearly display the signature of a bar: in Fig. 2.1 I put an illustrative image of a recently hypothesized barred spiral pattern based on very recent infrared observations (see e.g. [4, 5]) (Fig. 2.2).

2.3.2 The Interstellar Gas

It is important for our purposes to point out that the Galaxy is not only made of stars: indeed the environment in which CR propagation—which is the main topic of our work—takes place is the interstellar medium. It was evident from the first long-exposure photograph of the Galaxy taken by Edward Barnard (1857–1923) that several *dark zones* are present along the Milky Way and it was soon realized that these apparent holes in the star distribution are due to the presence, along the line of sight, of *clouds* of interstellar matter that obscure the starlight coming from behind. To be precise, the dust contained in these clouds is actually responsible for the absorption and scattering of photons coming from background stars, and therefore for their removal from the line of sight. Further studies demonstrated how the space between these very dense clouds was itself filled with a less opaque interstellar gas.

Today we know that interstellar matter contains about 10–15 % of the total mass of the disk. This gaseous, dust-bearing material concentrates near the plane and along

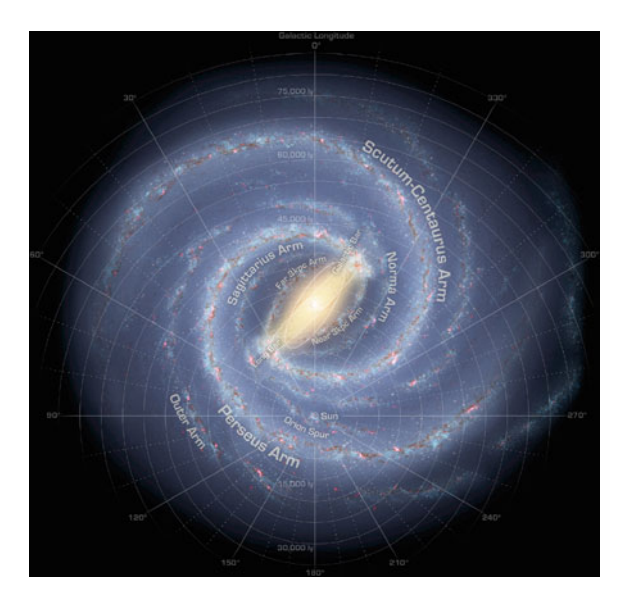


Fig. 2.1 Artist's view of a possible configuration of the Milky Way barred spiral pattern. Taken from the Astrophysical Picture of the Day (APOD) of June 6th, 2008 http://apod.nasa.gov/apod/ap080606.html. Illustration Credit: R. Hurt (SSC), JPL-Caltech, NASA. Notice that the Sun is located in an interarm region called *Orion spur* where some important star formation regions—e.g. Orion Nebula—are located (See Sect. 5.7.1 for a discussion on the role of this region on CR propagation). The two main arms are the Sagittarius and Perseus arms. This proposed pattern is slightly different from previous studies in which a four-arms structure was considered: the other two arms (Sagittarius—Carina and Norma) appear in this study as minor arms

the spiral arms and plays an important role in CR physics and in the whole field of high energy astrophysics since

- The magnetic field which is trapped inside the ionized part of this gas is responsible for CR diffusion, as we will see in the forthcoming paragraphs.
- The interaction of CRs with this material, through the process of *spallation*, originates secondary CRs of lower mass; the comprehension of this phenomenon is very important because secondary cosmic ray observations are used to test CR propagation models, as we will see in Chap. 4.
- Finally, the interactions of CR protons, helium, and heavier nuclei with IS gas creates pions; neutral pions decay forming gamma-rays, so a relevant portion of the gamma ray emission of the Galaxy actually traces the spatial distribution of the interstellar medium, as we will see in Chap. 6.

The interstellar gas appears to be very inhomogeneous: half of its mass is concentrated in discrete clouds which occupy a very small portion of the total volume (about 1%).

The interstellar gas can be subdivided in three *phases*:

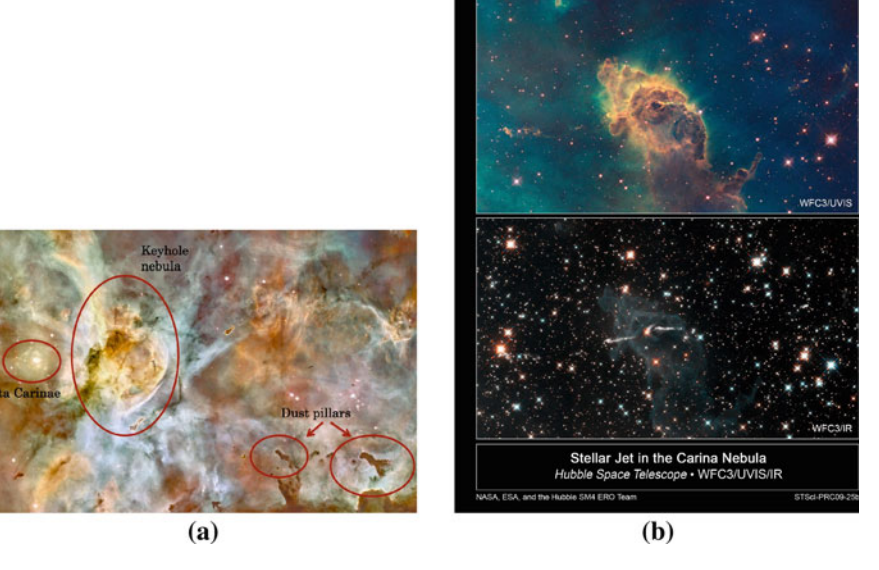


Fig. 2.2 a One of the largest star forming regions of our Galaxy, the Carina molecular complex. The super-massive star Eta Carinae (more than 100 solar masses) is one of the most energetic ones in the Galaxy; the Keyhole Nebula—discovered by Herschel in the nineteenth century—also houses several of the most massive stars known; the entire Carina Nebula is over 300 light-years wide and is located about 7500 light-years away in the constellation of Carina. This is the most detailed image of this region ever taken: it is actually a composition of 48 high-resolution frames taken by the Hubble Space Telescope two years ago. Image taken from http://apod.nasa. gov/apod/ap090524.html. Credit: NASA, ESA, N. Smith (U. California, Berkeley) et al. and The Hubble Heritage Team (STScI/AURA). b We show here a 2 light-years wide pillar of gas and dust within the giant Carina complex. The outlines are shaped by the winds and radiation of the young and hot massive stars already present in the Carina region; the interior of the structure, instead, hosts several stars in the process of formation, that are revealed in the more penetrating image in the lower panel, taken in the Infrared band, where also two narrow jets blasting outward from an infant star can be seen. Both visible light (upper) and near-infrared (lower) images were made using the Hubble Space Telescope's newly installed Wide Field Camera 3. Image taken from http://apod.nasa.gov/apod/ap091001.html. Credit: NASA, ESA, and the Hubble SM4 ERO Team

• Molecular gas. This phase presents the highest level of clumpiness, since it is mostly confined in very cold and dense complexes called *molecular clouds*. These clouds are very cold (~10 K) and the densest regions within them can reach a number density ~10⁶ cm⁻³, which is extremely tenuous for terrestrial standards (14 orders of magnitude smaller than the average density of the lower atmosphere) but quite large if compared to the typical value of the insterstellar matter (~0.1–1 cm⁻³). As we will see below, these objects play a crucial role in the Galactic "ecosystem" since they are the typical environment where star formation occurs. As far as chemical composition is concerned, the molecular gas mainly consists of Hydrogen; unfortunately the H₂ molecule is not directly observable both at optical and radio wavelengths: since it does not possess a permanent

electric dipole moment and has a very small moment of inertia, all its permitted transitions lie outside the observable domain. The CO molecule, instead, has a rotational transition at a radio wavelength of 2.6 mm: for this reason, the corresponding emission line has become the primary tracer of molecular interstellar gas. CO radio surveys permitted to reconstruct three-dimensional maps of the molecular Hydrogen distribution through the Galaxy: this is not an easy task since, for each line of sight, it requires to analyse the CO emission spectrum, convert doppler shifts into relative velocity, and—knowing the Galactic rotational curve—mapping each part of the spectrum to a position in the Galaxy. I will go through all the details and explain the tricky aspects of these procedures in Chap. 6.

An important milestone in the history of this kind of observations was the complete CO survey of the whole Galaxy (described in [6]) based on a combination of data from the Millimeter-wave Telescope at Cerro Tololo (Chile) and the Columbia Telescope in New York City; using this important dataset Bronfman et al. [7] were able to derive the radial and vertical distribution of molecular gas in the Galaxy; in Fig. 2.5 the radial gas distribution is shown together with models for pulsar and OB star distribution; concerning the vertical one, it is generally modelled as a Gaussian: $n_{gas} \propto \exp \left[-(z-z_0(R))^2 \cdot \ln(2)/z_{1/2}(R)\right]$, with the height scale $z_{1/2}(R)$ ranging from 58 to 83 pc in the inner Galaxy (being 80 pc at Solar position). More recently H. Nakanishi and Y. Sofue [8] computed a 3D map of the molecular and atomic gas in our Galaxy, revealing hints of the spiral arms structure; an even more detailed work was performed by M. Pohl et al. [9] who derived a 3D distribution of the molecular gas that points out, as supported by many radio observations, the presence of a bar besides the spiral pattern: this is one of the most accurate mapping of the interstellar gas in our Galaxy computed so far. These models are shown in Fig. 2.3.

• Atomic gas. The neutral phase of Hydrogen is not observable in the optical wavelength: particle collisions are so infrequent in the interstellar environment that nearly all H atoms have their electron in the ground energy state, and so all electromagnetic transitions between the ground level and an excited state lie in the UV (Lyman series). Neutral Hydrogen (HI) is therefore observed with radio telescopes: in fact, the interaction between the magnetic moment of the electron and that of the proton leads to a splitting of the electronic ground level into two extremely close energy levels, in which the electron spin is either parallel (upper level) or antiparallel (lower level) to the proton spin: the transition between these levels results in a 21 cm line that lies in the domain of Radio Astronomy. Nowadays, 21-cm emission line measurements covering the whole sky have been able to yield the Hydrogen space-averaged density as a function of position in the Galaxy. These maps show how HI too is organized in a spiral pattern, like H₂, and also its structure is quite complex, with overdensities and holes: for example, our Solar System itself is now believed to lie in a sort of cavity with a noticeable underdensity of neutral Hydrogen (the so called *local bubble*), whose origin is likely to be connected with the Supernova explosion that originated the nearby Geminga pulsar.

Concerning large-scale distribution (see [2] and references therein) HI extends up to 30 kpc away from the Galactic center, and the vertical distribution is broader

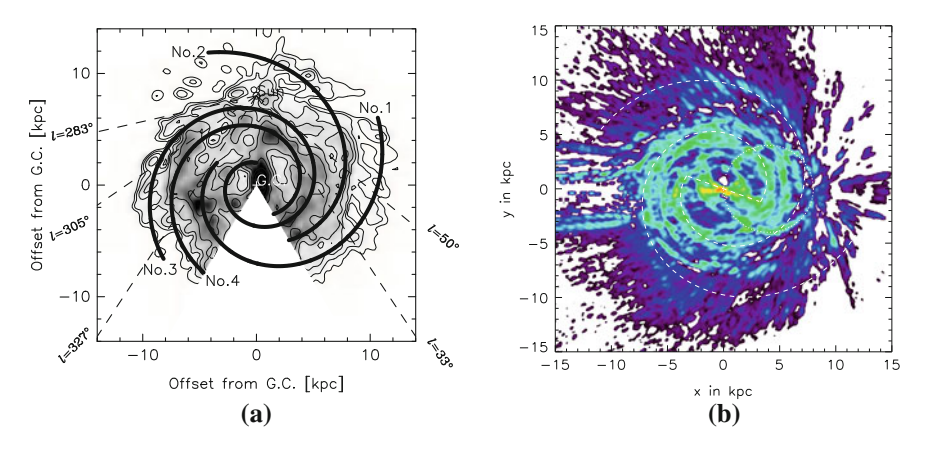


Fig. 2.3 3D gas distributions from Nakanishi and Sofue [8] and Pohl et al. [9]. a Gas distribution from Nakanishi and Sofue 2006. b Gas distribution from Pohl et al. 2008

compared to the H₂: the thickness of the HI layer is \sim 100 pc for R < 3 kpc, \simeq 230 pc for 3 < R < 8.5 kpc (twice the H₂) and then grows more than linearly with R in the outer Galaxy, reaching \sim 3 kpc at the outer Galactic boundary.

• Ionized gas. Ionized gas can be observed in the Optical band because of radiative recombination of Hydrogen and Helium ions with free electrons to excited states, and consequent radiative de-excitation; of special importance are the Hydrogen Balmer lines produced by electronic transitions from an excited state (n > 2) to the first excited state (n = 2): in fact, each recombination of a free proton with a free electron into an excited Hydrogen atom leads, sooner or later, to the emission of Balmer photon. In this way it is possible to map the HII distribution: ionized Hydrogen is detected in compact regions (HII regions) around massive stars, because of their emission of UV ionizing photons; moreover, diffuse ionized gas exterior to these regions exists in all directions around us. More recent, high-resolution maps display a complex structure made of patches, filaments and loops of enhanced Balmer H emission, superimposed on a fainter background. Unfortunately, due to the obscuration effect of the interstellar dust, the region that can be probed with H is limited to a cylindrical volume of radius $\sim 2-3$ kpc around the Sun.

For more distant regions, astronomers rely on a totally different phenomenon: the *dispersion of pulsar signals*. It is well known that electromagnetic waves travelling through an ionized medium interact with the free electrons in such a way that their group velocity decreases with increasing wavelengths. This occurs to pulsar emission too: the lower frequency part of the emission propagates more slowly through interstellar space and, therefore, arrives later at the observer; the resulting spread in the arrival times is a measurable quantity (called *Distance Measure*, DM) and can be shown to be directly proportional to the column density of free

¹ The H line corresponds to a transition between n = 3 and n = 2.

electrons between the pulsar and the observer. In this way it is possible to map the ionized gas density in a much wider region.

The DM database allowed to investigate both the radial and vertical distribution of ionized gas; it has been known for a long time that the scale height of this component is much broader than both H₂ and HI; for example in Reynolds 1991 [10] it is modelled as the sum of two Gaussians: $n_{\rm HII} = 0.015 \exp(|z|/70 \,\mathrm{pc}) + 0.025 \exp(|z|/900 \,\mathrm{pc}) \,\mathrm{cm}^{-3}$.

More recently, an important contribution to the distribution of ionized gas came from the work of J. M. Cordes and T. J. Lazio [11] who developed NE2001, a 3D model for the spatial distribution of free electrons based on a large collection of DMs of pulsars and extragalactic objects. The derived electron density consists of several components: a thin disk, a thick disk, a contribution from spiral arms and in addition a large number of source complexes, which is, however, not complete; the ionized gas at high latitudes is primarily due to the thick disk component with a scale-height of about 1 kpc and a mid-plane density of about 0.034 cm⁻³. The face-on map of the Galaxy obtained in this work clearly shows the spiral arm pattern.

The interstellar gas must not be considered as a static, stand-alone entity completely independent from the other components of the Galaxy. Conversely, it is animated by turbulent motion, is strongly coupled to the chaotic magnetic fields that deflect the CR path, and experiences a continuous interchange with the stellar population: in the densest regions of giant molecular complexes star formation takes place, then the material is processed inside the stars themselves, enriched with heavy elements and finally returns to the interstellar space either in a continuous way (through stellar winds) or by Supernova explosions.

A detailed understanding of all these processes is required to fully understand the origin and propagation of CRs, so I will go through a review of them (see e.g. [12])

The Giant Molecular Clouds (GMCs) are the most important environments from this point of view. GMCs contain most of the molecular Hydrogen present in the Galaxy. One may ask how these immense structures (with masses ranging from $\sim 10^4$ to $\sim 10^7$ solar masses) can survive in the severe environment of interstellar space, filled with energetic radiation (e.g. UV photons) that are able to dissociate the weak molecular bounds. Actually the neutral Hydrogen and the dust present in the outer layers contribute to absorb and scatter the ionizing radiation: the deep interior of the cloud is therefore protected and is composed by H_2 and other molecules (CO, OH). The temperature of the internal regions is $\sim 10\,\mathrm{K}$, fixed by the balance between the heating due to CR ionization and the cooling due to CO radio emission. The structure of a GMC is highly clumped: a high-resolution imaging can reveal dense *clumps* within a cloud, each clump being similar in its shape to the whole complex: this *self-similarity* has led to a fractal description of cloud structure, at least down to some lower characteristic length scale [13, 14] (Fig. 2.4).

The process of star formation starts when a cloud or a part of it is dense enough that the gas pressure is insufficient to support it: the cloud or the clump then undergoes

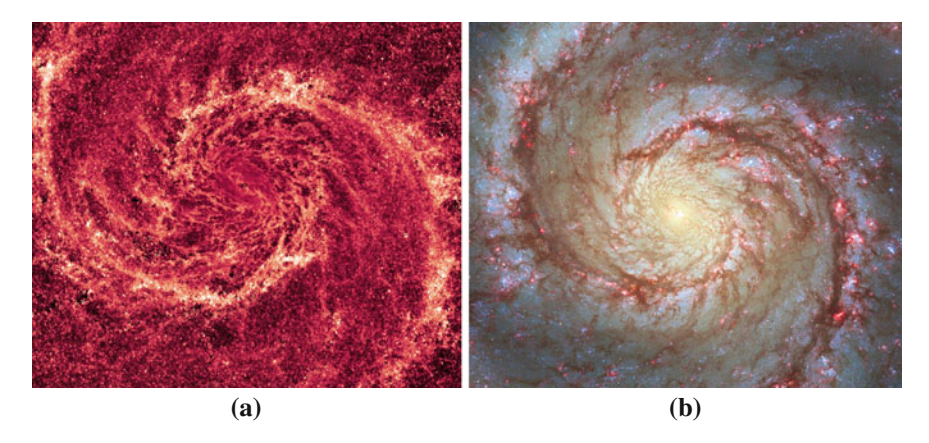


Fig. 2.4 a This image of the nearby M51 galaxy (the Whirlpool Galaxy) in *infrared* light highlights the dust that traces the dense star-forming molecular gas. The light coming from stars was digitally removed to better isolate the gaseous structures, which appear to be concentrated along spiral arms. **b** The optical image of the same galaxy reveal how HII regions originated by young, massive O and B stars—that appear as *red* diffuse spots in the picture—also concentrate in spiral arms, in correspondence with the molecular dust-rich complexes visible in the infrared, where most star formation takes place. Images taken from http://apod.nasa.gov/apod/ap110126.html. Credit. Infrared: NASA, ESA, M. Regan and B. Whitmore (STScI), R. Chandar (U. Toledo); Optical: NASA, ESA, S. Beckwith (STScI), and the Hubble Heritage Team (STScI/AURA)

gravitational collapse; this process can be triggered by some violent events: e.g. a collision with another cloud, or a Supernova explosion. ²

$$\rho \left[\frac{\partial \vec{v}}{\partial t} + (\vec{v} \cdot \vec{\nabla}) \vec{v} \right] = -\vec{\nabla} p + \rho \vec{g} + \frac{1}{4\pi} (\vec{\nabla} \times \vec{B}) \times \vec{B} \tag{2.1}$$

it is possible to derive the Virial theorem:

$$\frac{1}{2}\ddot{I} = 2(T - T_s) + M + W \tag{2.2}$$

where

- I it the momentum of inertia
- T, is defined by the following equation: $T \equiv \int_V \left(\frac{3}{2}P_{th} + \frac{1}{2}\rho v^2\right) dV$ and represents the internal kinetic energy, with a random microscopic component (thermal energy) and a macroscopic contribution (due to turbulent motions) that is often dominant.
- T_S , defined by: $T_S \equiv \frac{1}{2} \oint_S P_{ext} \vec{r} \cdot d\vec{S}$ takes into account the pressure of the external medium that surrounds the cloud.
- W is the gravitational energy.
- *M* is the magnetic term: $M = \frac{1}{8\pi} \int (B^2 B_0^2) dV$, where B_0 is the intensity of the field present in the surrounding medium.

According to which term prevails, the cloud or a part of it is considered self-gravitating (if the internal pressure due to thermal and turbulent motions is balanced by the gravitational field of the

 $^{^2}$ A quantitative description of these phenomena is based on magneto-hydro-dynamics (MHD). From the MHD equation of motion:

It is important to point out that stars always form in groups. The most massive and energetic ones, although less numerous than the low-mass ones, play a very important role in the evolution of the environment that gave birth to them: these stars, belonging to O and B spectral type, are very bright, and emit copious amounts of ultraviolet radiation that rapidly ionizes the surrounding interstellar gas of the giant molecular cloud, forming the so-called *HII regions*; moreover, they are very short-living and don't move very far from the sites they were formed; their life ends with a dramatic Supernova explosion and originates a compact object (a pulsar or a black hole) and an Supernova Remnant that finally merges with the surrounding Interstellar Medium.

2.3.3 SNRs and Pulsars

The picture described so far contains some elements that are very important for our purposes, in fact it shows how the sites where a lot of gas is present and Star Formation takes place (the Giant Molecular Clouds) are often associated with other astrophysical environments such as pulsars and Supernova Remnants (SNRs) that are crucial in CR physics.

SNRs, as we pointed out, have long been considered as the primary candidates for the origin of Galactic Cosmic Rays, and the diffusive shock acceleration described in the previous paragraph is widely accepted as the main acceleration mechanism.

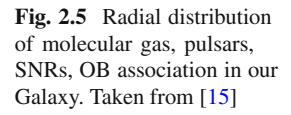
Many observational data support this theory: SNRs are bright radio, X and gamma-ray emitters, whose spectra have been extensively studied. In particular, is is very interesting to examine the gamma-ray emission spectra, both in the GeV region (and very accurate data are being collected in current years by Fermi-LAT) and in the TeV region (with ground experiments, such as H.E.S.S., MAGIC, etc.) because these datasets can help to distinguish between two scenarios, that we will describe in a quantitative way in Chap. 6 when we discuss gamma-ray diffuse emission from the Galaxy:

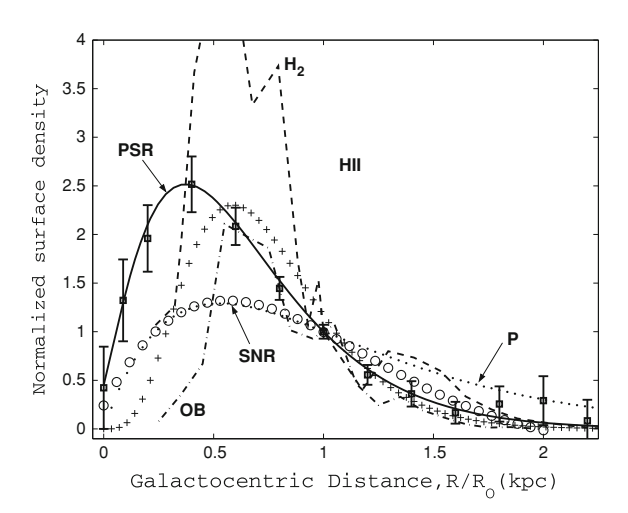
- A *leptonic* scenario in which gamma-rays are emitted by accelerated *electrons* via Synchrotron (in the radio domain) and Inverse Compton emission (in the Gamma domain).
- A *hadronic* scenario in which gamma-rays are emitted by accelerated *protons* and *nuclei* that interact with the surrounding gas, produce pions, and eventually gamma rays via π^0 decay.

In some remnants the *hadronic* picture seem to give a better fit of the data: this is the case, for example, of Cas A (Fermi-LAT recently reported [16] that the spectrum

⁽Footnote 2 continued)

cloud itself) or pressure-confined (if the external medium with its pressure does the same job). Star-forming clouds or clumps are generally self-gravitating. When the density gets too high, due to an external perturbation, the gravitational term becomes dominant and the cloud undergoes a collapse, which is the first step of star formation.





is better fit by a hadronic model); an extensively studied remnant is also RX J1713.7-3946, a shell-type SNR interacting with a molecular cloud, whose very high energy emission measured by HESS is well correlated with CO emission: the gamma photons should be therefore produced by π^0 decay [17].

So, SNRs should be the sites where the acceleration of the bulk of CR protons takes place; of course the definitive proof of such an interpretation would be the observation of neutrino emission by existing or forthcoming experiments such as IceCube or NEMO (in fact in a hadronic scenario also charged pion decay is present, and this process produces neutrinos).

For these reasons a detailed knowledge of the SNR distribution in our Galaxy is very important to model the CR source term. An updated catalogue [18] is available online [19]: it contains observational data for 274 Supernova Remnant in our Galaxy. Unfortunately, the difficulties related to SNR observations make the list very incomplete and the accuracy of distance estimates very low, so it is not easy to derive a map of SNRs in our Galaxy. Since the spatial distribution of SNRs is not known with precision, and therefore the source term of CR propagation, it is then useful to consider the above outlined deep link existing between CR sources and well known astrophysical environments and objects such as pulsars or OB associations whose distribution is known with better precision.

For example, as far as *pulsars* are concerned, the ATNF catalogue available at [20] is a very useful resource; it includes all published rotation-powered pulsars, including those detected only at high energies; a complete description can be found at [21].

This large number of accurate measurements permitted to derive a spatial distribution of pulsars (see for example [15, 22]). Considering what we have showed up to this point, these curves are often used as source terms for CR propagation models; in Fig. 2.5, taken from [15], a comparison between the derived radial distribution of

Pulsars, SNRs, OB stars and molecular Hydrogen is plotted: the reader can see very clearly the strong correlation that I pointed out in this paragraph.

Now we can briefly discuss another element that plays an important role in CR physics and permeates the whole Galaxy: the magnetic field.

2.3.4 The Magnetic Field

Magnetic fields are embedded in the ionized gas that permeates our Galaxy and are a fundamental component of the interstellar medium (ISM): they are essential in the formation of stars, they provide the pressure balance that prevents gravitational collapse of our Galaxy; they also undoubtedly play a role in the creation of galaxies as well as the formation of galaxy clusters. It is interesting to point out that, in our Galaxy, the energy density of interstellar magnetic fields is comparable to the energy density of diffuse starlight, of Cosmic Rays, and of the kinetic energy density of interstellar gas: this is an important hint of the interplay between all these components.

There are several techniques that permit to investigate the structure of the magnetic field in the interstellar medium (see [24] for a quick review). The most useful effect that permits to probe the large scale structure is the *Faraday Rotation of Linearly Polarised Radiation*: pulsars and extragalactic sources, usually external galaxies, emit linearly polarised radiation which rotates as it passes through regions that are filled with free electrons with and an embedded magnetic field; the amount of this rotation ψ defines the *Rotation Measure*, RM via the following equation:

$$\psi = \lambda^2 \int n_e \vec{B} \cdot d\vec{l} = \lambda^2 \cdot RM \tag{2.3}$$

The observation of the RM permits to calculate the magnetic field component along the line of sight, relying on a model for the electron density distribution (such as NE2001 by Cordes and Lazio).

The Galactic magnetic field consists of two components: a regular part and a turbulent part.

The regular field is itself subdivided into a disk field and a halo field.

It is generally accepted that our Galaxy has an organized large-scale disk field similar to other nearby Galaxies (see [23] and references therein); the field more or less follows the spiral pattern; the models for the field orientation in the Galactic plane are generally classified into an axi-symmetric spiral (ASS) with no dependence on the azimuthal angle or a bi-symmetric spiral (BSS); two different ASS models together with a BSS models are pictured in Fig. 2.6.

Little is known, unfortunately, on the halo field. In [23] the following parametrization is adopted, in cylindrical galactocentric coordinates:

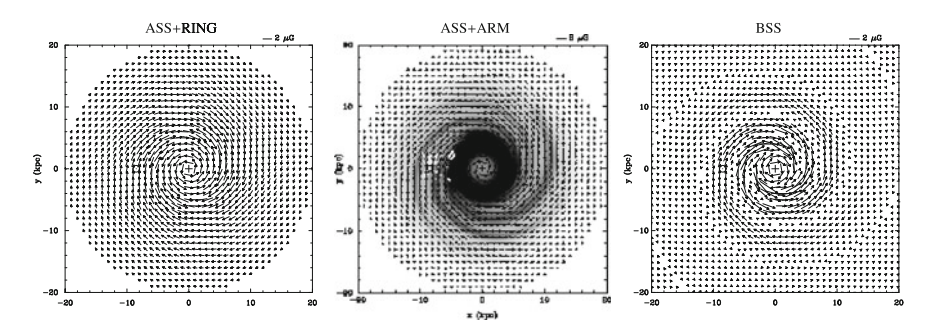


Fig. 2.6 Three different disk magnetic field models. Taken from [23]

$$B_{\phi}^{H}(R,z) = B_0 \frac{1}{1 + \left(\frac{z - z_0}{z_1}\right)^2} \frac{R}{R_0} \exp\left(\frac{R - R_0}{R_0}\right)$$
 (2.4)

with the follwing choice for the parameters: $z_0 = 1.5$ kpc, $z_1 = 0.2$ –0.4 kpc for z– z_0 , $B_0 = 10 \,\mu\text{G}$, $z_0 = 4$ kpc.

In [25] these parameters are revised. In fact, the above values would lead to a strong toroidal field with large values at high Galactic latitudes: such a field would produce—via interaction with CR electrons—a strong synchrotron emission which is not observed in the radio maps of the Galaxy. So, the new values of $z_0 = 1.5 \,\mathrm{kpc}$, $z_1 = 0.2$ –4 kpc for z– z_0 , $B_0 = 2 \,\mu\mathrm{G}$, $z_0 = 4 \,\mathrm{kpc}$ are considered. These numbers give a spatial distribution of B compatible with Synchrotron observation.

This is only one of the possible parametrizations, and actually there is a very large uncertainty on the shape and scale height of the halo field, which—as we will see—is a very important ingredient of a model for CR diffusion.

Besides the regular magnetic field, the existence of a random component is very important: in fact, as we will prove in the next paragraph, the interaction with this component forces the CRs to undergo a random walk instead of simply propagating in spirals along the regular field lines.

The equations of Magneto-hydro-dynamics (MHD) imply that, for very low resistivity, the field lines are *frozen* in the plasma and follow its motion (this is called the Alfvén theorem of *flux Freezing*): so the random component of the magnetic field is related to the turbulent motion in the interstellar gas, which is observed over a wide range of scales, from $\sim 100\,\mathrm{pc}$ down to $\sim 10^{-6}\,\mathrm{pc}$ or less [26].

A simple and very powerful model for turbulence in fluids was developed by Kolmogorov [27]. This model applies to a generic turbulent fluid: some driving energy is injected at large scales and then cascades to smaller scales by interactions between *eddies* of different size; the cascade is local in Fourier space (i.e. each eddy provides energy only to a slightly smaller one) and proceeds at a rate independent of scale; finally energy is dissipated by viscosity at the smallest scales. This model implies a power spectrum

$$E(k) = C\epsilon^{2/3}k^{-5/3} \tag{2.5}$$

where ϵ is the energy transfer rate and k is the inverse of the length scale. This equation describes, under very general hypotheses, how turbulent kinetic energy is distributed as a function of the scale considered.

Another model for the energy spectrum of turbulence was built by Kraichnan [28] and takes into account the presence of magnetic field. The energy spectrum for Kraichnan MHD turbulence is:

$$E(k) \propto k^{-3/2} \tag{2.6}$$

Nowadays it is commonly accepted that the driving energy is injected in the ISM at large scale by Supernova explosions; the spectrum, instead, is not known with precision, and it is uncertain if a Kolmogorov-like or a Kraichnan-like dependence on the scale is a good description of turbulent energy distribution over all the length scales. Armstrong et al. [29] collected a large number of independent observations on local Interstellar Medium on a very wide range of scales: from $\sim\!10^6\,\mathrm{m}$ to $\sim\!10^{18}\,\mathrm{m}$ and found that low-scale fluctuations can be connected to large scale ones via a Kolmogorov-like power spectrum, but the Kraichnan hypotesis is not excluded.

2.4 CR Propagation: The Diffusion Equation

2.4.1 Introductory Considerations

There are two important observations that must be taken into account in order to build a model describing CR propagation.

- The first one is the high level of isotropy of CRs compared to the strong anisotropy
 of the sources that—as we saw in the previous paragraph—are mainly distributed
 on the Galactic plane and should in principle lead to an increased flux towards the
 central regions of the Galaxy.
- The second one is the large abundance of some light elements (namely Li, Be, B) compared, e.g., to the solar abundances; this discrepancy can find an explanation in the process of *spallation* that we presented in the previous paragraph, i.e. the interaction of heavy CRs with interstellar gas that originates lighter nuclei. Simple calculations show that, in order to explain the observed abundances of these elements, a CR should go through a column density of $\sim 5 \, \text{g/cm}^2$ before reaching us: this number, compared to the average column density along a line of sight in the Galaxy $\sim 10^{-3} \, \text{g/cm}^2$, leads to the conclusion that CR propagation can't occur along straight lines: there must be some mechanism to confine the particles within the Galaxy.

A very simple model to describe CR confinement is the so called *leaky box model*: in this simplified phenomenological picture CRs are assumed to propagate freely within a cylindrical box and reflected at the boundaries; the loss of particles is

parametrized assuming the existence of a non-zero probability of escape for each encounter with the boundary.

The equation is very simple:

$$\frac{\partial N}{\partial t} = \frac{N}{\tau_{\rm esc}(E)} + Q(E) \tag{2.7}$$

where $\tau_{\rm esc}(E)$ is the escape time, which is shorter at higher energy, and Q is the source term.

Leaky box models are very useful to provide an effective description of some general properties of CR physics—and we will adopt them to prove simple features of propagated primary and secondary spectra—but a more realistic description of the mechanism CR confinement is needed. We discussed in the previous paragraph the existence of a magnetic field in the Galaxy, with a regular and a random component: now we will show that the interaction of CRs with such field provides the confining mechanism and this process can be described by a diffusion equation.

2.4.2 Diffusion Equation

The problem we have to solve is the interaction of a collection of relativistic charged particles with an astrophysical magnetized plasma (the problem is described in detail in [26], and we refer to that book for a complete derivation of the results summarized here).

Since in the astrophysical context the collision term is negligible, we have to solve the well known *Vlasov equation*:

$$\frac{\partial f(\vec{x}, \vec{p}, t)}{\partial t} + \vec{v} \frac{\partial f}{\partial \vec{x}} + \vec{F} \frac{\partial f}{\partial \vec{p}} = 0$$
 (2.8)

Since the force acting on those particles is the Lorentz force the equation can be written as:

$$\frac{\partial f(\vec{x}, \vec{p}, t)}{\partial t} + \vec{v} \frac{\partial f}{\partial \vec{x}} + Ze\left(\vec{E} + \frac{\vec{v}}{c} \times \vec{H}\right) \frac{\partial f}{\partial \vec{p}} = 0$$
 (2.9)

The common approach is the *quasi-linear approximation*, based on the separation of electric and magnetic fields into their average values and the random fluctuations, corresponding to an ensemble of waves with random phases:

- $\vec{H} = \vec{H}_0 + \vec{H}_1$, where $\langle \vec{H} \rangle = \vec{H}_0$ and $\langle \vec{H}_1 \rangle = 0$.
- $\vec{E} = \vec{E}_0 + \vec{E}_1$, where $\langle \vec{E} \rangle = 0$ and $\langle \vec{E}_1 \rangle = 0$ (the electric field average is of course zero: there is no net charge).

Also the distribution function is distinguished between the average f_0 and the fluctuating part f_1 .

Averaging Eq. 2.9 over the ensemble of waves and assuming their amplitude to be small, we obtain:

$$\frac{\partial f_1}{\partial t} + (\vec{v} \cdot \vec{\nabla}) f_1 + \frac{Ze}{c} (\vec{v} \times \vec{H}_0) \frac{\partial f_1}{\partial \vec{p}} = -Ze \left(\vec{E} + \frac{\vec{v}}{c} \times \vec{H}_1 \right) \frac{\partial f_0}{\partial \vec{p}}$$
(2.10)

At this point, it is useful to write the random fields as a Fourier integral:

$$\vec{E}(t,\vec{r}) = \sum_{\alpha} \int \vec{E}^{\alpha}(\vec{k}) e^{-i\omega^{\alpha}(\vec{k})t + i\vec{k}\cdot\vec{r}} d^{3}x$$

$$\vec{H}_{1}(t,\vec{r}) = \sum_{\alpha} \int \vec{H}_{1}^{\alpha}(\vec{k}) e^{-i\omega^{\alpha}(\vec{k})t + i\vec{k}\cdot\vec{r}} d^{3}x$$
(2.11)

where the summation is over the various types of waves propagating in the plasma. Introducing cylindrical coordinates p_{\parallel} , p_{\perp} and ϕ in momentum space (see [26] for further details) after some manipulations it is possible to obtain the following condition for an effective particle-wave scattering:

$$\omega^{\alpha}(\vec{k}) - k_{\parallel}v_{\parallel} - s\omega_H = 0 \tag{2.12}$$

where s is a integer. This is a *resonance condition*: it tells that the frequency of the wave (with Doppler effect taken into account) must be a multiple of the cyclotron frequency of the particle in the regular magnetic field H_0 ; in other words, particle-wave scattering occurs only with waves whose wavelength is comparable with the Larmor radius of the Cosmic Ray.

The waves we are interested in are Alfvén and magnetosonic waves.

Alfvén waves are travelling oscillation of the plamsa velocity and the magnetic field. The mechanism generating such waves can be pictured in the following way: a perturbation in the plasma velocity perpendicular to the external field \vec{H}_0 "bends" the magnetic field lines like a guitar string; the magnetic tension provides the restoring force; the oscillation created this way propagates with wave vector \vec{k} parallel to the external magnetic field line, with a dispersion relation

$$\omega(\vec{k}) = \pm |k_{\parallel}| v_A \tag{2.13}$$

where

$$v_A \equiv \frac{H_0}{4\pi\rho} \tag{2.14}$$

is the Alfvén velocity.

Although the Alfvén wave propagates in the direction of the magnetic field, waves exist at oblique incidence too and smoothly change into the *magnetosonic wave*: this kind of perturbation is longitudinal and very similar to actual sound waves, in fact

the propagation is perpendicular to the magnetic field and the restoring force is the magnetic pressure which is itself directed perpendicularly to the field.

Implementing the interaction of CR particles with Alfvén waves under a number of simplifying assumptions (in particular: a time scale larger than the scattering rate, the isotropy of the distribution function, an equal scattering rate for the regular field direction and the opposite one) one can obtain an equation of this kind [26]:

$$\frac{\partial f_0}{\partial t} = \frac{\partial}{\partial z} D_{xx} \frac{\partial f_0}{\partial z} + \frac{1}{p^2} \frac{\partial}{\partial p} p^2 D_{pp} \frac{\partial}{\partial p} f_0 + Q$$
 (2.15)

where Q is a source term.

This is a diffusion-reacceleration equation in which the following coefficients are used:

$$D_{xx} = \frac{v^2}{2} \int_0^1 \mathrm{d}\mu \frac{1 - \mu^2}{2\nu_\mu} \tag{2.16}$$

$$D_{pp} = p^2 (v_A/v)^2 \int_0^1 \mathrm{d}\mu (1 - \mu^2) \nu_\mu \tag{2.17}$$

In this equation we introduced the following terms:

- $\mu \equiv \cos \theta$ where θ is the pitch angle, i.e. the angle between \vec{p} and \vec{H}_0 ,
- ν_{μ} is the scattering rate, defined by the equation:

$$\nu_{\mu} \simeq 2\pi^2 |\omega_H| \frac{K_{\text{res}} W^{\alpha}(k_{\text{res}})}{H_0^2} \tag{2.18}$$

where ω_H is the cyclotron angular frequency, k_{res} is the angular wavenumber at resonance, $W^{\alpha}(k_{\text{res}})$ is the the wave energy density (calculated at resonance).

This equation shows how the transport of CR particles in a turbulent magnetized plasma is well described by a *diffusion* in space, along the direction of the regular magnetic field, accompanied by a *stochastic reacceleration* of the particle, which is more effective for larger values of v_A .

Now, if we assume that the energy spectrum of the waves has a power-law behaviour:

$$W(k) \propto \left(\frac{k}{k_0}\right)^{-s} \tag{2.19}$$

making use of Eqs. 2.18, 2.16 shows this energy dependence:

$$D_{xx} \propto \frac{H_0^2}{H_{\text{random}}^2} \left(\frac{2\pi r_H}{\lambda_0}\right)^{2-s} \tag{2.20}$$

where r_H is the Larmor radius of the particle in the magnetic field H_0 ; r_H depends on the particle rigidity in the following way:

$$r_H \sim 10^{-6} \frac{R[\text{GV}]}{B[\mu\text{G}]} pc$$
 (2.21)

After a simple calculation based on the assumption of a Kolmogorov-like turbulence in a typical environment with $H_0 = 5 \mu G$ one can obtain (see [26]):

$$D_{xx} \simeq 3 \cdot 10^{28} \frac{H_0^2}{H_r^2} \frac{v}{c} \left(\frac{R}{7\text{GV}}\right)^{(0.3)} \text{cm}^2/\text{s}$$
 (2.22)

From this formula one can estimate $D \simeq 10^{28} - 10^{29} \, \text{cm}^2/\text{s}$ at some GeV, i.e. a reasonable value that—as we will see—permits to reproduce the observed CR spectra.

As we discussed in the previous paragraph, the nature of the actual turbulence spectrum in the interstellar medium is currently matter of debate; it is not known if a unique power law (Kolmogorov-like, Kraichnan-like or different from the two) describes the power spectrum of the inhomogeneities in the interstellar plasma from the $\sim \! 100 \, \mathrm{pc}$ scale down to $\sim \! 10^{-6} \, \mathrm{pc}$, i.e. the scales corresponding to resonant scattering with particles from $\sim \! 10^{17} \, \mathrm{eV}$ down to $\sim \! 1 \, \mathrm{GeV}$. For this reason, the turbulent spectrum is considered as a free parameter and therefore the rigidity dependence of the diffusion equation: for a Kolmogorov turbulence Eq. 2.20 leads to $D \propto R^{1/3}$, while for a Kraichnan turbulence we have $D \propto R^{1/2}$.

So far we showed how, the framework of quasi-linear theory, i.e. for small turbulence, the resonant scattering on a weakly turbulent field leads mainly to a diffusion *along* the field; in this theory the perpendicular diffusion coefficient turns out to be very small:

$$\frac{D_{\perp}}{D_{\parallel}} = \frac{1}{1 + \left(\lambda_{\parallel}/r_L\right)^2} \tag{2.23}$$

where λ_{\parallel} is the mean free path in the regular field direction which is much greater than r_L .

However, in the typical conditions of interstellar space, the turbulence level is high: $A \equiv \frac{H_{\rm random}}{H_0} \sim 1$ and so the quasi-linear theory does not provide a satisfactory description of the diffusion in the perpendicular direction: we expect indeed that in such conditions parallel and perpendicular diffusion have comparable strength because the contribution of the regular field, which defines a favourite direction, becomes less important.

Moreover, we expect that in the perpendicular direction another mechanism called *field line random walk* (see e.g. [30]) is active, a mechanism that has been known for more than 40 years but whose modelization is quite hard: the idea is that, even though particles tend to random walk along the regular magnetic field lines, since the field lines themselves are braided and mixed in the orthogonal direction, the result

is a movement of the particles in the direction normal to the average regular field direction.

Considering non-linear effects is quite complicated and may alter some of the result described above. In particular, very recent works (e.g. [31]) show how a steeper dependence of the diffusion coefficient upon rigidity ($D \propto R^{0.6}$) may be obtained in presence of a Kolmogorov spectrum of turbulence, in contrast with the predictions of non linear theory (which would bring $D \propto R^{0.33}$).

Separating the contribution from parallel and perpendicular diffusion, the CR diffusion equation can be written in the general form, with respect to a generic regular magnetic field orientated along (b_r, b_ϕ, b_z) :

$$\frac{\partial f_0}{\partial t} = \frac{\partial}{\partial x_i} D_{ij} \frac{\partial f_0}{\partial x_i} + \frac{1}{p^2} \frac{\partial}{\partial p} p^2 D_{pp} \frac{\partial}{\partial p} f_0 + Q$$
 (2.24)

where we introduced the diffusion tensor:

$$D_{ij} \equiv (D_{\parallel} - D_{\perp}) b_i b_j + D_{\perp} \delta_{ij} \tag{2.25}$$

In order to clarify the reason of such a decomposition, notice that, i the coordinate system is chosen so that the regular magnetic field lies along one of the axes, e.g. the x axes, the diffusion tensor becomes diagonal and its elements are simply $D_{xx} = D_{\parallel}$, $D_{yy} = D_{zz} = D_{\perp}$.

In the case of our Galaxy it is convenient to adopt cylindrical coordinates. Under the simplifying hypothesis that the regular field is directed along ϕ , and assuming azimuthal simmetry, the diffusion equation simplifies to the following form (see Appendix A for the details of the calculation):

$$\frac{\partial f(r,z,p)}{\partial t} = \phi \frac{\partial f}{\partial r} + \psi \frac{\partial f}{\partial z} + \alpha \frac{\partial^2 f}{\partial r^2} + \beta \frac{\partial^2 f}{\partial z^2} + \frac{1}{p^2} \frac{\partial}{\partial p} p^2 D_{pp} \frac{\partial}{\partial p} f_0 + Q$$
(2.26)

where $\alpha = \beta = D_{\perp}$, $\phi = \frac{1}{r}D_{\perp} + \frac{\partial D_{\perp}}{\partial r}$ and $\psi = \frac{\partial D_{\perp}}{\partial z}$.

References

- 1. E. Fermi, On the origin of the cosmic radiation. Phys. Rev. 75, 1169–1174 (1949)
- K.M. Ferrière, The interstellar environment of our galaxy. Rev. Mod. Phys. 73, 1031–1066 (2001)
- J.H. Oort. A summary and assessment of current 21-cm results concerning spiral and disk structures in our galaxy. In URSI Symposium 1: Paris Symposium on Radio Astronomy, ed. by R.N. Bracewell, vol. 9 of IAU Symposium 1959. p. 409

References 27

4. R.A. Benjamin. The spiral structure of the galaxy: something old, something new... In *Massive Star Formation: Observations Confront Theory*, 2008. ed. by H. Beuther, H. Linz, T. Henning. Astronomical Society of the Pacific Conference Series. vol. 387, p. 375

- E. Churchwell, B.L. Babler, M.R. Meade, B.A. Whitney, R. Benjamin, R. Indebetouw, C. Cyganowski, T.P. Robitaille, M. Povich, C. Watson, S. Bracker, The spitzer/GLIMPSE surveys: a new view of the milky way. Publ. Astron. Soc. Pac. 121, 213–230 (2009)
- T.M. Dame, H. Ungerechts, R.S. Cohen, E.J. de Geus, I.A. Grenier, J. May, D.C. Murphy, L.-A. Nyman, P. Thaddeus, A composite CO survey of the entire milky way. Astrophys. J. 322, 706–720 (1987)
- L. Bronfman, R.S. Cohen, H. Alvarez, J. May, P. Thaddeus, A CO survey of the southern milky way—the mean radial distribution of molecular clouds within the solar circle. Astrophys. J. 324, 248–266 (1988)
- 8. H. Nakanishi, Y. Sofue, Three-Dimensional distribution of the ISM in the milky way galaxy:II. The molecular gas disk. Publ. Astron. Soc. Jpn. **58**, 847–860 (2006)
- 9. M. Pohl, P. Englmaier, N. Bissantz, Three-Dimensional distribution of molecular gas in the barred milky way. Astrophys. J. 677, 283–291 (2008)
- R.J. Reynolds, Ionized disk/halo gas—insight from optical emission lines and pulsar dispersion measures. ed. by H. Bloemen. IAU Symposium, 1991. The Interstellar Disk-Halo Connection in Galaxies, vol. 144, pp. 67–76
- J.M. Cordes, T.J.W. Lazio, NE2001.I. A new model for the galactic distribution of free electrons and its fluctuations. ArXiv Astrophysics e-prints, 2002
- C.F. McKee, The dynamical structure and evolution of giant molecular clouds. In NATO ASIC Proceedings of 540: The Origin of Stars and Planetary Systems, 1999. ed. by C.J. Lada, N.D. Kylafis. p. 29
- 13. D. Chappell, J. Scalo, Multifractal scaling, geometrical diversity, and hierarchical structure in the cool interstellar medium. Astrophys. J. **551**, 712–729 (2001)
- N. Sánchez, E.J. Alfaro, E. Pérez, Determining the fractal dimension of the interstellar medium.
 In Revista Mexicana de Astronomia y Astrofisica Conference Series, volume 35 of Revista Mexicana de Astronomica y Astrofisca, 27, 76–77 (2009)
- I. Yusifov, I. Küçük, Revisiting the radial distribution of pulsars in the galaxy. Astron. Astrophys. 422, 545–553 (2004)
- 16. A.A. Abdo et al. [Fermi collaboration]. Astrophys. J. Lett. **710**, L92–L97 (2010)
- F. Aharonian, [H.E.S.S. Collaboration]. A detailed spectral and morphological study of the gamma-ray supernova remnant RX J1713.7-3946 with HESS. Astron. Astrophys. 449, 223– 242 (2006)
- D.A. Green, A revised galactic supernova remnant catalogue. Bull. Astron. Soc. India 37, 45–61 (2009)
- D.A. Green. A catalogue of galactic supernova remnants. http://www.mrao.cam.ac.uk/surveys/ snrs/
- R.N. Manchester, G.B. Hobbs, A. Teoh, M. Hobbs, The Australia telescope national facility pulsar catalogue. http://www.atnf.csiro.au/people/pulsar/psrcat/
- R.N. Manchester, G.B. Hobbs, A. Teoh, M. Hobbs, The Australia Telescope National Facility Pulsar Catalogue. Astron. J. 129, 1993–2006 (2005)
- D.R. Lorimer, The galactic distribution of radio pulsars. In 35th COSPAR Scientific Assembly, 2004. ed. by J.-P. Paillé. vol. 35, p. 1321
- X.H. Sun, W. Reich, A. Waelkens, T.A. Enßlin, Radio observational constraints on Galactic 3D-emission models. Astron. Astrophys. 477, 573–592 (2008)
- 24. J.C. Brown, The magnetic field of the milky way galaxy. In Astronomical Society of the Pacific Conference, 2010. ed. by R. Kothes, T.L. Landecker, A.G. Willis. Astronomical Society of the Pacific Conference Series, vol. 438, p. 216
- X.-H. Sun, W. Reich, The Galactic halo magneticfield revisited. Res. Astron. Astrophys. 10, 1287–1297 (2010)
- V.S. Berezinskii, S.V. Bulanov, V.A. Dogiel, V.S. Ptuskin, Astrophysics of Cosmic Rays, (North holland, Amsterdam, 1990)

- 27. A.N. Kolmogorov, The local structure of turbulence inincompressible viscous fluid for very large Reynolds numbers. Royal Soc. Lond. Proc. Ser. A **434**, 9–13 (1991)
- R.H. Kraichnan, Inertial-range spectrum of hydromagnetic turbulence. Phys. Fluids 8, 1385– 1387 (1965)
- 29. J.W. Armstrong, B.J. Rickett, S.R. Spangler, Electron density power spectrum in the local interstellar medium. Astrophys. J. **443**, 209–221 (1995)
- J. Giacalone, J.R. Jokipii, The transport of cosmic rays across a turbulent magnetic field. Astrophys. J. 520, 204–214 (1999)
- 31. A. Shalchi, R. Schlickeiser, Evidence for the nonlinear transport of Galactic cosmic rays. Astrophys. J. Lett. **626**, L97–L99 (2005)

Chapter 3 **Numerical Codes that Solve the CR Diffusion Equations**

3.1 Numerical Approach to the Solution of CR Diffusion Equation

As we discussed in the previous section, we are dealing with a diffusion-reacceleration equation (Eq. 2.26).

Expressing the equation in terms of the CR density N(r, z, p) instead of the distribution function f(r, z, p) we obtain:

$$\frac{\partial N(r,z,p)}{\partial t} = \phi \frac{\partial N}{\partial r} + \psi \frac{\partial N}{\partial z} + \alpha \frac{\partial^2 N}{\partial r^2} + \beta \frac{\partial^2 N}{\partial z^2} + \frac{\partial}{\partial p} p^2 D_{pp} \frac{\partial}{\partial p} \frac{N}{p^2} + Q(r,z,p)$$
(3.1)

where
$$\alpha = \beta = D_{\perp}$$
, $\phi = \frac{1}{r}D_{\perp} + \frac{\partial D_{\perp}}{\partial r}$ and $\psi = \frac{\partial D_{\perp}}{\partial z}$.

where $\alpha=\beta=D_{\perp},\,\phi=\frac{1}{r}D_{\perp}+\frac{\partial D_{\perp}}{\partial r}$ and $\psi=\frac{\partial D_{\perp}}{\partial z}$. This equation can be solved analitically under simplified assumptions, and I will discuss later some interesting results obtained with semi-analytical codes that solve the propagation problem; of course the numerical solution permits, instead, to adopt any desired spatial distribution for CR sources and diffusion coefficient, and is therefore preferred in our opinion:

The usual method consists in approximating the derivatives with finite differences; a widely used technique adopted for the discretization is the so called Cranck-Nicholson (Numerical recipes in C homepage) scheme: I will show how it works with a one dimensional example.

Let's consider this equation:

$$\frac{\partial N}{\partial t} = D \frac{\partial^2 N}{\partial x^2} \tag{3.2}$$

The Cranck-Nicholson scheme consists in an average of the implicit and explicit Forward Time Centered Space (FTCS) discretization:

$$\frac{N_i^{n+1} - N_i^n}{\Delta t} = \frac{D}{2} \left[\frac{(N_{i+1}^{n+1} - 2 \cdot N_i^{n+1} + N_{i-1}^{n+1}) + (N_{i+1}^n - 2 \cdot N_i^n + N_{i-1}^n)}{(\Delta x)^2} \right]$$
(3.3)

where the index *i* refers to the spatial grid while the indexes n+1 and n refer to the evaluation of the quantities at time $t+\Delta t$ and t.

This method was shown to be unconditionally stable (i.e. stable for all values of Δt). The accuracy is second order in both space and time.

The algorithm must be generalized to the case of our interest, i.e. a partial differential equation with two spatial partial derivatives; the generalized methods that are generally adopted are the *Operator Splitting* (OS) and the more accurate *Alternate Direction Implicit* (ADI).

The Operator Splitting procedure is simple.

If we are dealing with an equation of the form

$$\frac{\partial N}{\partial t} = \mathcal{L}N\tag{3.4}$$

where the operator \mathcal{L} is a sum of m pieces: $\mathcal{L} = \mathcal{L}_1 + \mathcal{L}_1 + ... + \mathcal{L}_m$ and if we know, for each \mathcal{L}_i , a differencing scheme \mathcal{U} that permits to update the variable N from timestep n to n+1, the method consists in applying in sequence the updating scheme to all operators:

$$N^{n+1/m} = \mathcal{U}_1(N^n, \Delta t)$$

$$N^{n+2/m} = \mathcal{U}_2(N^n, \Delta t)$$
...
$$N^{n+1} = \mathcal{U}_m(N^n, \Delta t)$$
(3.5)

In our case, we can apply the OS to Eq. 3.1 with a triple splitting: (1) the radial derivatives; (2) the z derivatives; (3) the momentum derivatives.

The discretization of first part is:

$$\frac{N_{i,j,k}^{n+1} - N_{i,j,k}^{n}}{\Delta t} = \frac{1}{2} \phi \left(\frac{N_{i+1,j,k}^{n+1} - N_{i-1,j,k}^{n+1}}{2\Delta r} + \frac{N_{i+1,j,k}^{n} - N_{i-1,j,k}^{n}}{2\Delta r} \right) + \frac{1}{2} \alpha \left(\frac{N_{i+1,j,k}^{n+1} - 2N_{i,j,k}^{n+1} - N_{i-1,j,k}^{n+1}}{(\Delta r)^{2}} + \frac{N_{i+1,j,k}^{n} - 2N_{i,j,k}^{n} - N_{i-1,j,k}^{n}}{(\Delta r)^{2}} \right) + Q_{i,i,k}^{n} \tag{3.6}$$

where the indexes i, j, k refer to the r, z and p grid respectively while n+1 and n refer to the evaluation of the quantities at time $t+\Delta t$ and t.

Separating terms referring to different timesteps we obtain:

$$\left(-\frac{\alpha\Delta t}{2(\Delta r)^2} - \frac{\phi\Delta t}{4\Delta r}\right) N_{i+1,j,k}^{n+1} + \left(1 + \frac{\alpha\Delta t}{(\Delta r)^2}\right) N_{i,j,k}^{n+1} + \left(\frac{\alpha\Delta t}{2(\Delta r)^2} + \frac{\phi\Delta t}{4\Delta r}\right) N_{i-1,j,k}^{n+1} \\
= \left(-\frac{\alpha\Delta t}{2(\Delta r)^2} + \frac{\phi\Delta t}{4\Delta r}\right) N_{i+1,j,k}^{n} + \left(1 - \frac{\alpha\Delta t}{(\Delta r)^2}\right) N_{i,j,k}^{n} + \left(\frac{\alpha\Delta t}{2(\Delta r)^2} - \frac{\phi\Delta t}{4\Delta r}\right) N_{i-1,j,k}^{n} \\
+ Q_{i,j,k}^{n} \tag{3.7}$$

This is a tridiagonal system of equation that can be easily solved: in this way it is possible to compute $N_{r,z,p}^{n+1}$. The same procedure is then applied to the z and momentum derivative. The process ends when a convergence condition becomes satisfied: I will describe in next section the criteria we implemented in our code.

The ADI method is a refinement of the Operator Splitting technique. There are two main differences: (1) the timestep for each fractional step is only 1/m of the full timestep; (2) in each substep the updating scheme includes algebraically all the pieces of the total operator \mathcal{L} .

3.2 DRAGON Code: A Detailed Description

When we started our project, GalProp (The galprop code for cosmic-ray transport and diffuse emission production), with its almost 15 years of development behind it, was by far the most important and complete code that computed CR propagation and gamma-ray production in our Galaxy.

We decided to write our own code because we wanted to work with a spatially variable diffusion coefficient, which was not possible with the public version of GalProp since the spatial dependence introduces new terms in the equation and therefore relevant differences in the code itself; we also liked to have a deep insight of what the code was actually doing and of the effect of each parameter, and this is difficult with a code written by a third part; moreover we desired a quick and compact program suitable for performing a large number of runs, doing statistical analyses. Finally, we intended to prepare it to be coupled with Dark_SUSY package in order to propagate DM originated CRs.

Now DRAGON is itself a complete code that propagates CRs (by solving the diffusion-loss equation descrived in the previous section) and gamma-rays, performs very quickly and was recently released to the public.¹

DRAGON is written in C++ and makes full use of the advantages of such a complex language: it features 34 classes and all computations are performed in a highly optimized way, especially from the point of view of memory management (e.g. big

¹ It can be downloaded at http://www.desy.de/~maccione/DRAGON/.

bundles of data are always passed in the form of pointers to a structured object). Some parts of DRAGON are built following GalProp (v50p). The first reason is that it is a waste of time to reimplement standard parts, like energy losses, in which nothing new has to be found. The second reason is that it is essential to be able to compare our predictions with that of the GalProp code, and this can be done only by following the details of its implementation. Therefore, we kept in the code some features and models used in GalProp, like nuclear cross-sections, the gas distribution, the convergence technique. However, each of these models is accompanied by other models, which can be selected by setting the appropriate switch.

The equation solved by DRAGON is more complicated than the one reported in the previous paragraph, because there are several effects that have to be considered beyond diffusion and reaccelearation:

- Convection. The existence of galactic winds in many galaxies suggests that convective transport of CRs could be important [1]. Winds themselves can be CR driven, so a feedback between CR propagation and the wind dynamic may exist; they can also produce adiabatic energy losses as the wind speed increases away from the disk.
- Energy losses. Nucleons lose energy via ionization and Coulomb interactions with interstellar gas (see [2, 3] and also references therein). Electrons and positrons also lose energy due to Inverse Compton, Synchrotron and Bremsstrahlung processes (See Chap. 5 for the relevant formulas related to these processes).
- Spallation from heavier nuclei and decay of unstable nuclei. As we mentioned in Chap. 1 and in Chap. 2, CR nuclei interact with IS gas and may produce lighter nuclei via *spallation*. For this reason, a numerical code that describes CR propagation should consider both a loss term due to this process and a contribution to the source term due to spallation from heavier species. Of course, the finite lifetime of unstable isotopes must also be taken into account.

Taking all these physical processes into account, the complete equation for a nuclear species becomes:

$$\frac{\partial N^{i}(r,z,p)}{\partial t} = \left(\frac{1}{r}D_{\perp} + \frac{\partial D_{\perp}}{\partial r}\right) \frac{\partial N^{i}}{\partial r} + \left(\frac{\partial D_{\perp}}{\partial z}\right) \frac{\partial N^{i}}{\partial z}
+ D_{\perp} \frac{\partial^{2}N^{i}}{\partial r^{2}} + D_{\perp} \frac{\partial^{2}N^{i}}{\partial z^{2}} + v_{c} \cdot \nabla N^{i}
- \frac{\partial}{\partial p} \left(\dot{p} - \frac{p}{3} \nabla \cdot v_{c}\right) N^{i} + \frac{\partial}{\partial p} p^{2} D_{pp} \frac{\partial}{\partial p} \frac{N^{i}}{p^{2}} + Q(r,z,p)$$
(3.8)

which is quite similar to the one solved by GalProp: the main difference is the presence of the first derivatives in r an z that appear since D is a function of position (in GalProp it is considered instead as a constant which is therefore not affected by the gradient).

The equation is solved for each nucleus, starting from the heavier one: in fact, for each species, the source term contains a contribution due to spallation from heavier nuclei.

A complete description of the technical details of the code can be found in Appendix B. Here I will focus on the main features.

We implemented as a standard method the fast Operator Splitting (OS) that is used by default to obtain a good approximation of the solution in a reasonable amount of time.

The algorithm is the same we described in Sect. 3.1; the calculation starts with a very large Δt , of order $\sim 10^3$ Myr; the program performs some time steps with this large interval, then the Δt is halved until a minimum Δt is reached; the minimum time step has to be of order of 100 years to have reasonable solutions for nuclei, and of order of 1 year for leptons. This trick, also implemented in GalProp, permits to take into account all the physical processes that have very different intrinsic time scales and at the same time reduces the computation time to a reasonable duration.

If the user wants to refine the solution, the ADI method can be added in cascade for a better precision: in the ADI implementation the Δt does not change throughout the calculation; for each species, the iterations stop when a convergence criterion is reached: the condition requires that the maximum relative difference $\Delta x_i^{n+1}/x_i^n$ between a point in the grid at time n and the same point at time n+1 does not exceed some control value adjustable by the user (e.g. 10^{-3}). This criterion permits to control the accuracy of the solution, and is not implement in the OS technique, in which the program just ends when the minimum Δt is reached.

In the following chapters we will see DRAGON "in action" and we will describe many results related to CR nuclei and electron/positron propagation obtained with this package.

References

- D. Breitschwerdt, S. Komossa, Galactic fountains and galactic Cloud. Astrophys. Space Sci. 272, 3–13 (2000)
- K. Mannheim, R. Schlickeiser, Interactions of cosmic ray nuclei. Astron. Astrophys. 286, 983–996 (1994)
- A.W. Strong, I.V. Moskalenko, Propagation of cosmic-ray nucleons in the galaxy. Astrophys. J. 509, 212–228 (1998)

Chapter 4

Propagation of CR Nuclei: Our Results

4.1 Introduction

Hadrons are the most abundant particles of the CR flux and it is natural to start with this dominant component.

In this chapter:

- I will describe how to build a CR propagation model, which assumptions are necessary on the source term, the gas distribution and other astrophysical inputs.
- I will consider the free parameters involved in a typical model, and the main observables one has to take into account in order to constrain them; in particular I will focus on boron-to-carbon and antiproton-to-proton ratios.
- I will show how—using our numerical package DRAGON—we were able to perform a maximum likelihood analysis and outline a preferred set of propagation parameters making use of recent measurements on B/C and antiprotons. Hadronic data are well fitted by our model and no significant hint of new physics is found in the data. I will compare our results with other works in the Literature and point out the differences and innovations in our approach and in our results. I will also address the systematic uncertainties of our analysis.
- I will briefly mention how forthcoming data will be useful to put an even better constraint on the parameters.

4.2 How to Test Diffusion Models: B/C, Antiprotons. Previous Results

Building a CR propagation model consists in solving the diffusion-loss equation presented in the previous chapters by means of a numerical (or semi-analytical) code and compute, *for all desired CR species*, the spatial distribution and energy

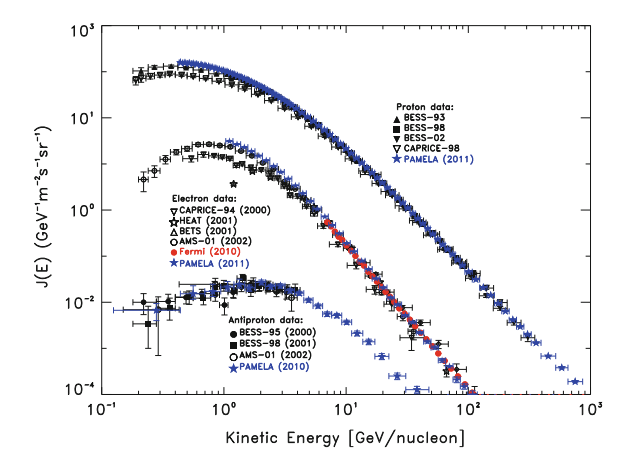


Fig. 4.1 Cosmic ray spectra at top of the atmosphere measured by recent experiments. I plotted here for illustrative purpose the CR differential fluxes as a function of kinetik energy for protons, electrons and antiprotons. Notice how the protons dominate over the other components. Both for protons and electrons, experiments performed in different epochs measured different fluxes at low energy: this is an effect of solar modulation, which strongly depends on the Solar Cycle phase. At high energy both protons and electrons are well described, at first approximation, by a power-law (we will add some detail about this). Notice how the electron spectrum is steeper with respect to the proton spectrum: this is en effect of the IC and Synchrotron energy losses suffered by the leptonic CRs. The very accurate datasets published during the last 2 years by Fermi and PAMELA collaborations are highlighted in colour

spectrum after propagation, given the distribution and spectrum of the sources plus other astrophysical inputs (Fig. 4.1).

For the hadronic component the role of energy losses is not very important, and the main process that affects their spatial and energy distribution is the energy-dependent diffusion. Hadronic CRs random walk through of the Galaxy and manage to get very far from the thin region around the Galactic plane where the majority of the sources is located: this motion results in a spread of the CRs through all the Galactic halo.

In Fig. 4.2b and c, in order to illustrate this process, I show the proton spatial distribution after propagation computed with DRAGON as a function of cylindric Galactocentric coordinates R and z. The source term is plotted in Fig. 4.2a for comparison. It is clear that in the whole energy range the hadronic part of the CRs diffuse through all the halo and get out of the slab where the source term peaks.

The main difference between low and high energy comes from the fact that the diffusion coefficient gets higher as the rigidity increases: so the CR escape in the z direction is favoured for high-energy CRs: this affects the *spectrum* that is steepened by energy-dependent diffusion with respect to the injection one, as we mentioned in the Introduction. I will come back to this with more details in the following.

Of course the main direct observable that is used to test all this scenario is the energy spectrum of each species at Sun position, although gamma-ray maps,

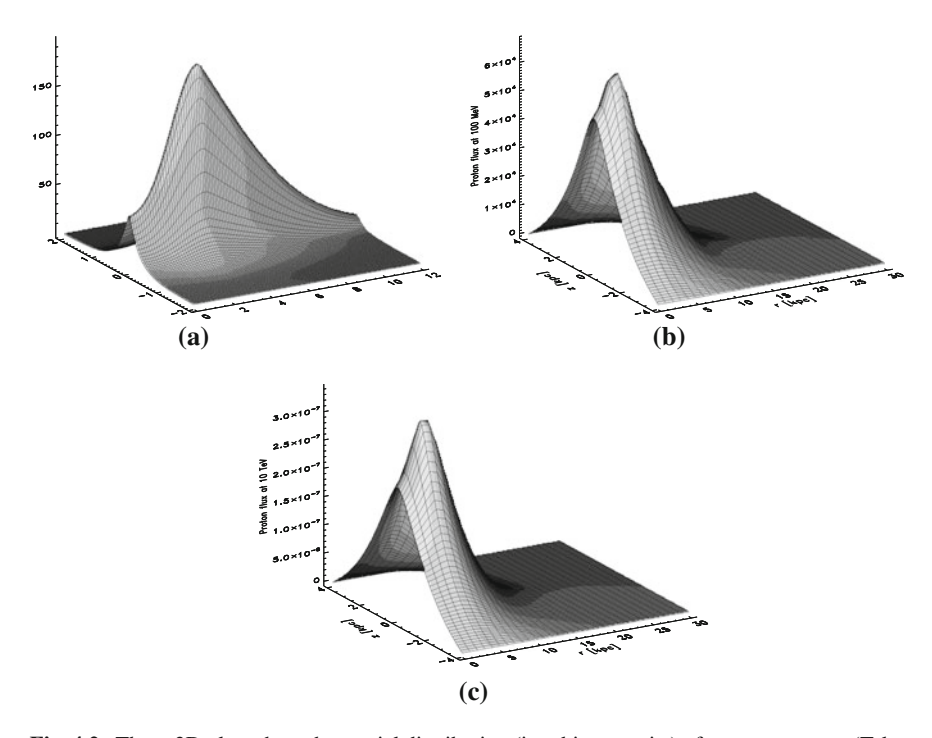


Fig. 4.2 These 3D plots show the spatial distribution (in arbitrary units) of our source term (Taken from [1]), and the CR proton distribution *after propagation* computed with DRAGON at 100 MeV and 10 TeV. **a** Source term. **b** Propagated protons at 100 MeV. **c** Propagated protons at 10 TeV

synchrotron maps and other astrophysical observations may help to trace also the spatial distribution through the Galaxy.

In order to develop a complete diffusion model for CR propagation, it is necessary first of all to implement the following astrophysical inputs, and then to determine the free parameters involved.

- The source function. If we work in cylindrical symmetry, it is a function S(r, z, p). The *spatial distribution* of CR sources is not known with precision, because of the incompleteness of the SNR catalogues. As I discussed in Chap. 2, it is then useful to use other astrophysical objects and environments as tracers (e.g. pulsars, OB associations...).
 - Concerning the *momentum dependence*, it is generally taken as a power law, in some cases with one break or more; the slope is called the *injection index* and is expected to be $\simeq -2$. from the theory of Fermi acceleration mechanism.
- The gas distribution. It is usually a smooth function $n_{gas}(r, z)$. The production of secondary CRs (especially light nuclei, such as Boron, or Antiprotons) strongly depends on the amount of target nuclei present along the primary CR path; we will see that the uncertainty on the gas amount mainly reflects on an uncertainty on

the normalization of the diffusion coefficient. We are not interested in this context in the details of the Galactic structure, because hadronic observables are sensitive to the integrated distribution on a large region around the Sun; we will explore in more detail the spatial distribution in the chapter devoted to Gamma Rays.

- The interstellar radiation field. The low-energy background of radio, IR, visible and UV photons coming from stars, HII regions, dust, etc. is important because it affects the CR energy loss via Inverse Compton process.
- The diffusion coefficient. The perpendicular diffusion coefficient (the only one that is relevant with our assumption of cylindrical symmetry) is, in general, a function $D_{\perp}(r, z, p)$.

The *rigidity dependence* is generally taken as $D_{\perp} = D_0 \mathcal{R}^{\delta}$ where \mathcal{R} is the particle rigidity.

Low energy effects on the diffusion coefficient may be parametrized in the following way

$$D_{\perp} = D_0 \beta^{\eta} \mathcal{R}^{\delta} \tag{4.1}$$

As we will see below, in this way it is possible to account for an expected lowenergy effect such as the dissipation of MHD waves as a consequence of their resonant interaction with CRs: the parametrization above permits an effective modelization of the phenomenon [2]. We will come back to this issue later on in this chapter.

The *spatial distribution* is usually not considered in the Literature; in the last chapter I will show instead how considering the variation of D_{\perp} through the Galaxy is very important and may contribute to solve serious problems such as the *Gradient problem*.

- The spallation network. It is necessary to know, from nuclear physics, the decay lifetimes and branching ratios of all species involved; moreover, for each pair $(Z_1, A_1; Z_2, A_2)$ it is necessary to know the spallation cross section as a function of energy: in fact, each particle that is propagated has a source term contribution either from the decay or the spallation of heavier particles.
- The Solar modulation. Solar modulation consists in: (1) the CR diffusion through the heliospheric magnetic field, (2) the convection driven by the outward motion of the solar wind, and (3) the adiabatic deceleration in this flow.

Gleeson and Axford [3] showed that these processes can be approximated as a motion in an effective radial electric field, so CR modulation is described under this so-called *force-field approximation* by only one parameter: the potential Φ . The modulation of a CR species is therefore given, with respect to the Local Interstellar Spectrum (LIS), by the following formula:

$$J(E_k, Z, A) = \frac{(E_k + m)^2 - m^2}{\left(E_k + m + \frac{Z|e|}{A}\Phi\right)^2 - m^2} J_{LIS}\left(E_k + \frac{Z|e|}{A}\Phi, Z, A\right).$$
(4.2)

It is important to point out that this is a low-energy effect that is almost negligible above few GeV.

When these models have been set, there are several free parameters to be determined:

- The injection spectrum and abundance for each CR species: for each nucleus, the relative abundance and the injection index (or indexes, if a break is considered) must be set.
- The normalization and energy dependence of the diffusion coefficient: these are the most important parameters for CR propagation: D_0 is the absolute normalization and δ is the slope.
- The Alfvén velocity: v_A; it parametrizes the efficiency of the stochastic reaccelearation mechanism.
- The convective velocity: v_C ; it is the velocity of the convective wind (if present) that may contribute to the vertical escape of CRs from the Galactic plane. The convective velocity can be considered constant or linearly increasing with the distance z from the Galactic plane. In the following we will not consider convection since—as I will explain in detail—our purpose is to constrain the propagation parameters relative to diffusion considering high-energy data, and convection is a low-energy effect; moreover, we will show that it is possible to reconcile all existing data in the whole energy range without taking this effect into consideration, and our approach is to minimize the number of free parameters.
- The halo thickness: z_h ; it is the height of the propagation halo where stochastic diffusion and reacceleration takes place. Notice that in some models (e.g. semi-analytical models [4, 5]) the region in which diffusion takes place is taken larger with respect to the slab where reacceleration is effective.
- The modulation potential: Φ; in Literature different values of this parameter are adopted, generally by comparison with low energy observation of primary species. We stress that, since it is related to an effective description of the phenomenon of solar modulation, the value used in a particular setup is *model dependent* so different sets of parameters may result in different choices of Φ. Moreover, the value is expected to change with time according to the 11-year cycle of Solar activity, so different experiments performed in different epochs may require very different values of this parameter.

In particular, we are interested in the parameters related to *propagation*: especially δ , but also v_A (v_C is convection is present), D_0 and z_t .

These parameters are loosely constrained by theory: D_0 depends on the turbulence level in the interstellar medium, δ is related to the turbulence spectrum (as discussed in the previous chapter), the diffusion halo thickness may take any value from \sim 1 to \sim 10 kpc, and little is known on the effectiveness of reacceleration and convection.

Moreover, all these quantities depend on the local properties (density, magnetization, temperature) of the ISM, and are therefore expected to exhibit strong variations depending on the position in the Galaxy: as we discussed, many different environments exist, with different physical properties. For example, the Alfvén velocity is related to the magnetic field and gas numerical density by the relation $v_A = 1.8 \cdot 10^5 B \left[\mu G \right] / \sqrt{n \left[\text{cm}^{-3} \right]} \left[\text{cm s}^{-1} \right]$, so in a typical HII region (n = 0.001,

 $B \sim 1-10 \,\mu G$) the expected value is $\sim 50-500 \,\mathrm{km/s}$, while in a typical molecular cloud ($n \sim 10^2-10^3$) it can be as low as $\sim 1-10 \,\mathrm{km/s}$.

Of course in a large-scale propagation model only the large-amplitude variations can be taken into account, and the parameters have to be intended as averages over large volumes (\sim 100–200 pc, depending on the grid resolution).

The only viable method to determine the parameters is therefore the comparison with observations: let's see now which observables are best suitable for this purpose.

- If one considers the energy spectrum of a **single primary species** at high energy (by high energy I mean here $E > 10 \,\text{GeV}$) after propagation:
 - the **normalization** of the propagated spectrum depends on D_0 and z_t ; actually, the two quantities are degenerate, i.e. for each D_0 that one can consider there is always a value of z_t which reproduces the correct normalization.
 - This degeneracy is not surprising from a physical point of view: in fact, an increase in the diffusion coefficient corresponds to a quicker escape of CRs from the diffusion halo: if the halo itself increases, the escape time remains unchanged and so the CR spectrum remains the same. For this reason, from now on, I will only consider the ratio D_0/z_t .
 - the **slope** of the spectrum depends both on the injection index at the source and on the energy dependence of the diffusion coefficient (parametrized by δ), as I mentioned at the beginning of the chapter.

The proof of this statement is easily obtained in the context of simplified *leaky-box models* (see Sect. 2.4). In the stationary case the equation is:

$$Q(E) = \frac{N(E)}{\tau_{esc}(E)} \Rightarrow N(E) \propto Q(E)\tau_{esc}^{-1}(E) \Rightarrow N(E) \propto E^{-\alpha - \delta}$$
 (4.3)

So we proved quantitatively what we described at the beginning of this chapter: the effect of the energy-dependent diffusion—which is parametrized by δ —is to *steepen* the injection spectrum of a primary species from $-\alpha$ to $-\alpha - \delta$. See Fig. 4.3a for a visualization of the effect of different values of δ on the propagated proton spectrum.

• On the other hand, **secondary-to-primary ratios** at high energy don't show this degeneracy: while the normalization still depends on D_0/z_t , the slope is now only affected by on δ , as can be easily shown in a leaky-box formalism:

$$\frac{N_{sec}(E)}{\tau_{esc}(E)} = -\frac{N_{sec}(E)}{\tau_{int}(E)} \Rightarrow \frac{N_{pri}(E)P_{spall}(E)}{\tau_{int}(E)} = 0$$

$$\Rightarrow \frac{N_{sec}}{N_{pri}} \propto \frac{P_{spall}(E)\tau_{esc}(E)}{\tau_{int}(E)} \Rightarrow E^{-\delta} \tag{4.4}$$

The reader may visualize this result in Fig. 4.3b and d, in which the B/C is plotted for different values both of the injection index α and of the δ : it is evident how the injection slope has no effect at all on the ratio.

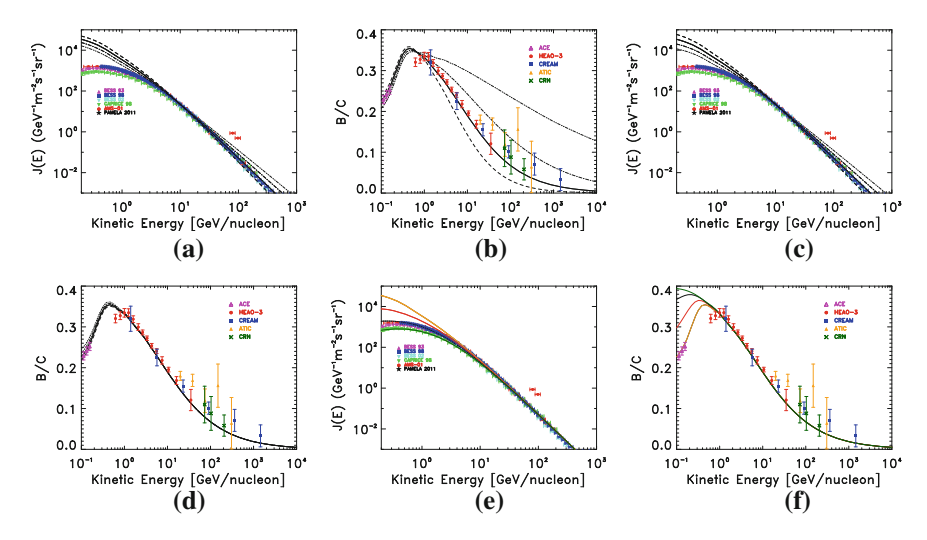


Fig. 4.3 The effect of energy-dependent diffusion is to steepen the injection spectrum of a primary species α , so that the propagated spectrum slope is $\alpha+\delta$ where δ parametrizes the rigidity dependence of the diffusion coefficient. The secondary-to-primary ratios, instead, only depend on δ . **a, b** Proton spectra and B/C for different values of δ : 0.2; 0.4; 0.6; 0.8. Injection index is fixed to 2.15. No reacceleration, no convection, no solar modulation. It is clear how larger values of δ lead to a steeper propagated proton spectrum and to a steeper B/C. **c, d** Proton spectra and B/C for different values of α : 1.75; 1.95; 2.15; 2.35. δ is fixed to 0.6. No reacceleration, no convection, no solar modulation. It is clear how larger values of α lead to a steeper propagated proton spectrum; the Boron-to-Carbon ratio, instead, does not depend at all on the injection index.**d, e** Proton spectra and B/C for different values of Φ : 0; 200; 450; 600 MeV; δ is fixed to 0.6, α is 2.15. No reacceleration, no convection. Solar modulation affects the lowest part of the propagated spectrum, and lowers the primary fluxes depending on the value of the potential. Notice that this effect must be taken into account in the model to correctly reproduce the data

So we showed how secondary-to-primary ratios at high energy give information on D_0/z_t and δ , i.e. the spatial diffusion parameters; the low-energy region, instead, is useful to constain the other parameters v_A , v_C and Φ , since these effects only affect the low-energy part of the CR spectra and do not play a relevant role above $\sim 10 \, \text{GeV}$.

When we started our work in this field, the most important results obtained with a numerical code on the comparison between models and data were obtained by GalProp team.

A large number of publications were released by this group on this topic during many years (see e.g. [6, 7]). The results were obtained with GalProp package and point towards a model with a high level of reacceleration ($v_A = 30$ km/s in the so-called *conventional* model presented in [7]): such an efficient reacceleration permits to obtain a very good fit of the B/C ratio in the whole energy range considered, including the peak detected at 1 GeV. Most CR-releated observables, indeeed, are reproduced with this model. The δ is 0.33, compatible with a Kolmogorov-like turbulence spectrum (according to the quasi-linear analysis).

A typical feature of this kind of model is the necessity of a *break* in the injection spectrum because otherwise the very high reacceleration would not permit to correctly reproduce the shape of low-energy primary spectra (in particular the proton spectrum). Another issue is the slight underproduction of antiprotons (cited e.g. in [8]). We will discuss in detail how our strategy led us to build a different class of models in which a different approach to solve these problems is adopted.

A different approach was followed by Maurin et al. [4, 5]. Their strategy is to consider the diffusion equation in a simplified geometry. The Galactic disk is described as a thin cylinder of radius R = 20 kpc and height h = 100 pc; the disk is embedded in a thicker diffusion halo of cylindrical shape with the same radius R and unknown height L (treated as a free parameter). CR sources are located in the disk, and the source term does not depend on the position; also the interstellar gas is confined in the disk with constant density $n = 1 \, \mathrm{cm}^{-3}$; the spatial diffusion of CRs occurs uniformly both in the disk and in the halo, while reacceleration and convection, if considered, are effective only in the disk.

In this simplified framework it is possible to find an exact solution of the diffusion equation.

Working with analytical solution makes the computation of the model very fast and permits to perform statistical analyses in which all the relevant parameters are allowed to vary; for example in [4] the authors obtained good quantitative constraints on the propagation parameters, and restricted δ in the range [0.45–0.85]; for every δ in this interval, a confidence region for v_C and v_A was found.

Another important result was obtained by this group in Donato et al. 2004 [9]: in this paper the contribution of Particle Dark Matter annihilation to CR antiproton flux is investigated, with particular focus on the uncertainties due to different values of the propagation parameters. The authors present thee models, called MIN, MED and MAX. They correspond to very different choices of the free parameters: the MIN model has a halo heigth of only 1 kpc, $\delta = 0.85$ and a strong convection ($v_C = 13.5 \, \text{km/s}$); the MAX model, on the opposite side, has a very large halo (15 kpc), $\delta = 0.46$ and a very efficient reacceleration ($v_A = 117.6 \, \text{km/s}$). These models are all compatible with B/C and give respectively the minimal, median and maximal supersymmetric antiproton flux: they have been widely adopted in the literature related to Particle Dark Matter indirect search. We will come back to this issue with more detail in Sect. 5.5 devoted to Dark Matter models.

4.3 Our Maximum Likelihood Analysis on B/C and Antiproton Data

4.3.1 Our Method and Results

When we completed the first version of DRAGON, we performed a complete analysis on recently released B/C and antiproton data in order to constrain the propagation

parameters listed above. The analysis was published in 2010 [12]. One the motivation of this work was the recent release of (1) very accurate measurements of the anitproton-to-proton ratio performed by PAMELA collaboration [13] that would permit us to do a joint analysis of light nuclei and antiproton data which had not been done before and also (2) high-energy data on B/C from CREAM collaboration [14] that are very important because they refer to a previously unexplored energy window.

This analysis expanded and completed a pioneering scan of the parameter space in plain-diffusion setup that used a preliminary version of our code and did not account for recent CREAM data that were not available yet at the time. The results were published in 2008 [15]. Although reacceleration was not included in the code at the time, we were able to fit all secondary-to-primary ratios (boron-to-carbon, nitrogen-over-oxygen, carbon-over-oxygen) above ~ 1 GeV/n in that work and found a preferred value for the diffusion coefficient slope $\delta = 0.57$.

The statistical analysis published in [12] was the *first analysis of this kind* performed with a numerical code, and the approach was very different with respect to other works in the Literature.

The key point is *looking at high energy*, because it is known, following what I explained above, that below some GeV many effects contribute to shape the B/C and antiproton spectra (solar modulation, maybe convection, plus other phenomena such as dissipation of MHD waves etc.).

For this reason we performed three different analyses: the first restricted to data points with $E > 10\,\mathrm{GeV/n}$, the second with $E_{\mathrm{min}} = 5\,\mathrm{GeV/n}$ and the third with $E_{\mathrm{min}} = 1\,\mathrm{GeV/n}$. The purpose of such an energy dependent analysis is: (1) use high-energy data to constrain the parameters directly connected to the pure diffusion: D_0/zt and δ , (2) use the intermediate range (1–10 GeV) to constrain the effectiveness of reacceleration (v_A) and (3) finally look at the low-energy part (<1 GeV) to tune the solar modulation potential and possibly other effects relevant to that range.

The algorithm we followed is the following.

First of all, we set the Galactic distribution of CR souces, gas and radiation, diffusion coefficient.

• For the **source term**, we assumed the general form

$$Q_i(E_k, r, z) = f_S(r, z) q_0^i \left(\frac{\rho(E_k)}{\rho_0}\right)^{-\alpha_i},$$
 (4.5)

and imposed the normalization condition $f_S(r_{\odot}, z_{\odot}) = 1$.

We assumed the spatial distribution $f_S(r, z)$ to trace the SNR distribution as modeled in [1] on the basis of pulsar and progenitor star surveys (Fig. 4.4a).

This is slightly different from the radial distributions adopted in GalProp-based articles (e.g. [6, 7]) which are based on pulsar surveys only.

Concerning the source slope, we proceeded like this: for each value of δ that we consider, we fixed the injection slope α by requiring that at very high energy

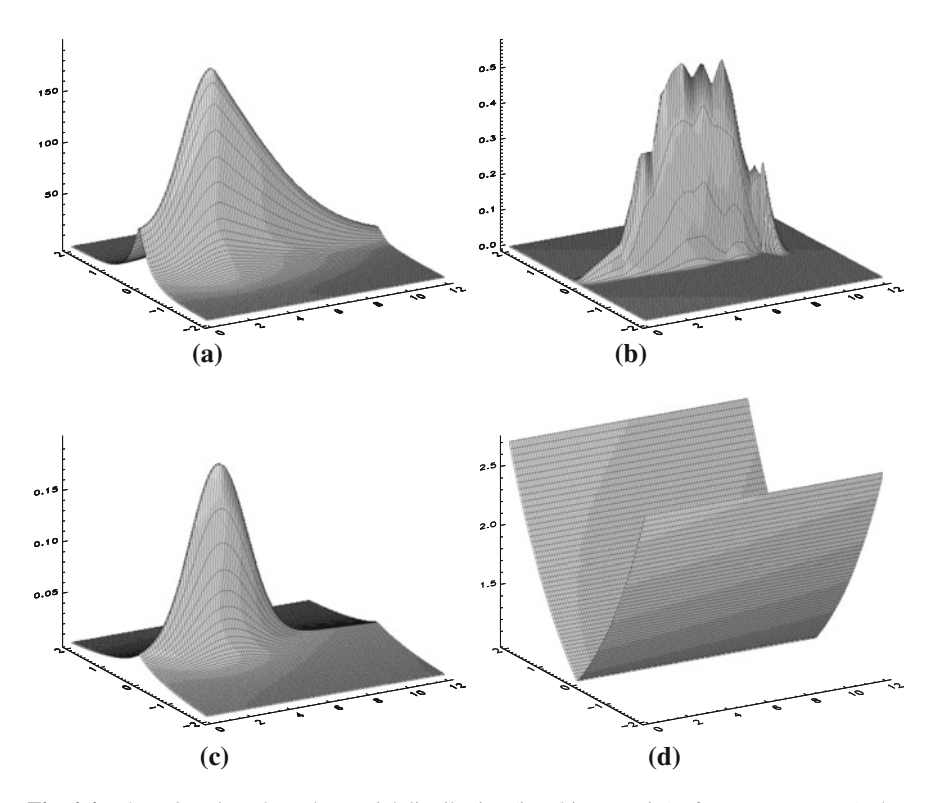


Fig. 4.4 These 3D plots show the spatial distribution (in arbitrary units) of our source term (Taken from [1]), the molecular gas ([10]), the ionized gas ([11]) and the perpendicular diffusion coefficient used for our analysis. The distributions are functions of R and z; cylindrical symmetry is assumed. a Source term. b Molecular gas. c Ionized gas. d Diffusion coefficient

 $(E_k \gg 100 \, \text{GeV/n})$ the propagated slope obeys the equality $\alpha + \delta = \gamma$ (Eq. 4.2). We adopted the same spectral index for all nuclei.

The injection abundances q_0^i were tuned so that the propagated, and modulated, spectra of primary species fit the observed ones. In particular,

- we chose to normalize the source spectra of Oxygen and heavier nuclides to reproduce the observed spectra in CRs at $E\sim 100\,{\rm GeV/n}$;
- on the other hand, the injection abundances of Carbon and Nitrogen (which, together with Oxygen mostly affect the B/C) were treated as free parameters, and we included them in the statistical analysis in a way which we will describe in the following.

It is important to remind that we assumed no spectral breaks in the source spectrum of all nuclear species. As we will discuss at the end of the chapter, this point is

crucial to understand the difference between our results and those of some previous works.

- Concerning the **gas distribution**, we adopted the same used in GalProp v50. i.e.:
 - for the molecular gas, the distribution by Bronfman [10] plotted in Fig. 4.4b.
 - for the atomic gas, the distribution by Gordon and Burton [16].
 - for the ionized gas, the distribution by Cordes et al. [11].
- For the diffusion coefficient, we adopted the parametrization of Eq. 4.1. We considered a very simple spatial distribution, with an exponential dependence upon z: D ∝ exp (z/z_t). The scale height z_t is a free parameter. In each simulation we take the boundaries of the diffusion box at least two times larger than the z_t. The z dependence of D allows to obtain a more realistic distribution of CRs after propagation, and makes the calculations independent on boundary effects. Nevertheless, we verified that, as far as spectra at Sun position are considered, every model computed in this way corresponds to a conventional model (in which D(z) is constant) by a simple scaling of the normalization (the D₀ parameter).
- For the **spallation cross sections**, we used the same compilation of data adopted in GalProp.

For antiprotons, the main processes responsible for their production are: $p-p_{\rm gas}$, $p-He_{\rm gas}$, $He-p_{\rm gas}$ and $He-He_{\rm gas}$ plus a negligible contribution from other nuclei.

Similarly to [5, 17] we adopt the production cross-section calculated using the parametrization given in Tan and Ng [18].

We will see below how the adoption of other parametrizations may affect our results.

• For the **modulation potential**, we verified that the possibility of restricting our analysis to $E_k > 1 \,\text{GeV/n}$ reduces the systematic uncertainties associated to this unknown: above $1 \,\text{GeV/n}$ the effects of modulation on the secondary/primary CR ratios used in our analysis are tiny and can safely be accounted for by means of the simple *force field* approximation.

The *potential* for heavy nuclei is set by comparison with low energy data on primary species: for B/C, C/O, N/O we use Oxygen data, for protons and antiprotons use low-energy data on protons from BESS [19] AMS-01 [20] and PAMELA [13].

We will discuss later how the uncertainties on these distribution may alter some of our results.

We will see, in particular, that a different choice of the source term profile through the Galaxy, the gas distribution, or the X_{CO} conversion factor reflects on a different propagated CR distribution and affects quite significantly the normalization of the diffusion coefficient D_0 but has little effect on the parameters related to the energy-dependent effects: δ and v_A in particular.

In the last chapter we will come back to the issue of source and gas distribution and we will see if our choices are compatible with gamma-ray data.

Once we set the distributions of the astrophysical variables, we performed the following steps for 5 different values of the Alfvén velocity: 0, 10, 15, 20, 30 km s⁻¹:

- For each point of the parameter space characterized by δ and D_0/z_t we varied the C/O and N/O source ratios to compute the χ^2 (which we call $\chi^2_{\rm C,N,O}$) of the propagated (and modulated) C/O and N/O against experimental data in the energy range $1 < E_k < 10^3 \, {\rm GeV/n}$.
 - We need to do this preliminary analysis for self-consistency reasons: Carbon and Nitrogen give a major contribution to Boron production via spallation and their spectra are shaped by spallation losses in a different way depending on the propagation parameters. So the best way to proceed in our opinion is to determine their best-fit abundances by comparison with the observed C/O and N/O ratios *for each set of propagation parameters we consider*.
- Once the source abundances were fixed, we finely sampled the parameter space $(\delta, D_0/z_t)$ by using, for each couple of these parameters, the C/O and N/O source ratios which minimized $\chi^2_{\text{C,N,O}}$; for each of these realizations we computed the χ^2 (which we call $\chi^2_{\text{B/C}}$) for the B/C modulated ratio against data in several energy ranges.

The datasets we used for the light nuclei ratios are:

- the data from HEAO-3 satellite mission that operated from September 1979 to May 1981. That mission, although quite old, provided a very accurate measurement of B/C, N/O and C/O in the ≃0.6-≃35 GeV energy range [21].
- the data from CRN mission [22].
- the recent data from CREAM balloon mission [14] that expanded our knowledge of the light nuclei ratios up to ~1 TeV/n.

The dataset we used for the antiproton-to-proton ratios is the recent one from PAMELA [13]. In the plots we also show low-energy measurements from BESS [19] and AMS-01 [20].

The procedure described above was iterated three times considering different values of E_{min} : 1, 5 and 10 GeV/n.

Moreover, we repeated again the procedure with B/C data alone, antiproton data alone and combined data.

In conclusion, we obtained 15 sets of best-fit parameters for B/C data (corresponding to different values of v_A and different minimum energies), 15 sets for antiproton data and 15 sets for combined B/C—antiproton data.

We also computed the confidence level regions in the $(\delta, D_0/z_t)$ parameter space corresponding to the 68, 95 and 99 % probabilities.

We summarize our results in Table 4.1. In Fig. 4.5 the Confidence Levels (CLs) corresponding to the B/C, antiproton and joint analysis with $E_{min} = 5$ GeV are shown.

¹ Every time we refer to a χ^2 , we mean the χ^2 divided by the number of degrees of freedom, i.e. the so called reduced χ^2 .

| v_A [km/s] | $E_{\min} [\text{GeV/n}]$ | B/C analysis | | | Joint analysis | | |
|--------------|---------------------------|--------------|-----------|----------|----------------|-----------|----------|
| | | δ | D_0/z_t | χ^2 | δ | D_0/z_t | χ^2 |
| 0 | 1 | 0.57 | 0.60 | 0.38 | 0.47 | 0.74 | 3.25 |
| | 5 | 0.52 | 0.65 | 0.33 | 0.41 | 0.85 | 2.04 |
| | 10 | 0.46 | 0.76 | 0.19 | 0.44 | 0.82 | 1.57 |
| 10 | 1 | 0.52 | 0.68 | 0.32 | 0.49 | 0.71 | 1.47 |
| | 5 | 0.49 | 0.71 | 0.28 | 0.41 | 0.85 | 1.69 |
| | 10 | 0.44 | 0.82 | 0.20 | 0.44 | 0.82 | 0.12 |
| 15 | 1 | 0.46 | 0.76 | 0.33 | 0.47 | 0.76 | 0.94 |
| | 5 | 0.49 | 0.73 | 0.26 | 0.44 | 0.82 | 0.12 |
| | 10 | 0.44 | 0.84 | 0.18 | 0.41 | 0.98 | 0.16 |
| 20 | 1 | 0.41 | 0.90 | 0.47 | 0.47 | 0.79 | 2.28 |
| | 5 | 0.44 | 0.84 | 0.22 | 0.44 | 0.84 | 0.85 |
| | 10 | 0.44 | 0.87 | 0.20 | 0.44 | 0.85 | 0.98 |
| 30 | 1 | 0.33 | 1.20 | 0.40 | 0.33 | 1.20 | 5.84 |
| | 5 | 0.38 | 1.06 | 0.20 | 0.36 | 1.09 | 2.47 |
| | 10 | 0.41 | 0.98 | 0.16 | 0.38 | 1.04 | 1.61 |

Table 4.1 Best fit parameters, and the corresponding χ^2 values, resulting from comparing our model predictions with nuclear experimental data alone (B/C analysis) and with nuclear and \bar{p}/p combined data (combined statistical analysis), as described in text

The values corresponding to $E_{\rm min}=5~{\rm GeV/n}$ for the combined analysis, which are used to constrain our models, are reported in bold

4.3.2 Discussion on B/C Analysis

Let's start to discuss the results with the B/C analysis.

As the reader can see from the first column of Table 4.1, the B/C analysis points towards values of δ confined in the following ranges:

- - [0.33-0.57] for $E_{\min} = 1 \text{ GeV/n}$,
- - [0.38-0.52] for $E_{\min} = 5 \text{ GeV/n}$,
- - [0.41-0.46] for $E_{\min} = 10 \,\text{GeV/n}$.

Noticeably the high-energy analysis—that should explore the region of the spectrum in which only diffusion-related effects act—outlines a *narrow range* for this parameter, that appears to be *weakly dependent* on the value of the Alfvén velocity. This is encouraging because it confirms what stated above, i.e. that at high energy only diffusion is effective.

As the E_{min} decreases, the range broadens and—if all data above 1 GeV are considered—it is interesting to notice that both

- high values of δ in correspondence to low values of v_A and, on the other hand,
- low values of δ (0.33) and high reacceleration ($v_A = 30 \,\mathrm{km/s}$)

are allowed. This sort of degeneracy at low energy is due to the fact that: (1) the effect of a higher δ is to *steepen* the spectrum of the B/C (because a higher energy dependence of the diffusion coefficient makes the high-energy CRs escape more easily

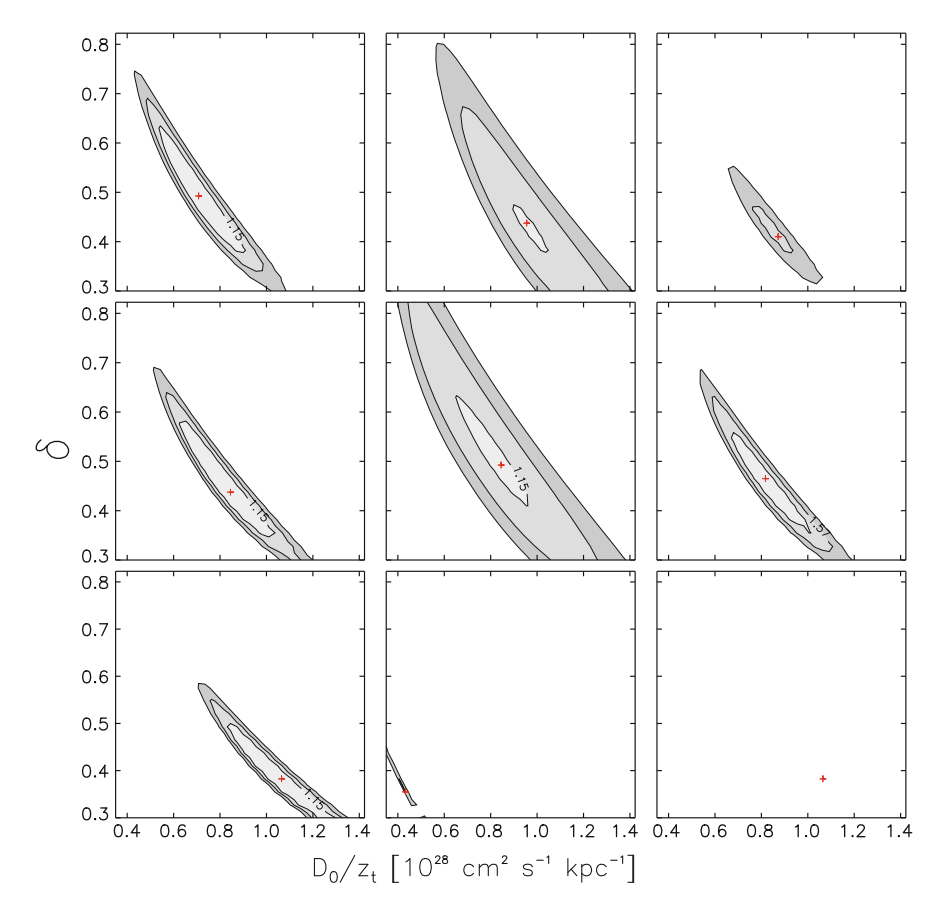


Fig. 4.5 The 68, 95 and 99 % confidence level regions of DRAGON models, computed for $E_{\min} = 5 \,\text{GeV/n}$ are represented in the plane $(D_0/z_t, \delta)$. For the 68 % confidence level the corresponding value of the χ^2 is also shown. The *red crosses* show the best-fit position. Each *row* corresponds to different values of the Alfvén velocity: $v_A = 10, 20, 30 \,\text{km/s}$ from top to bottom. Each *column* corresponds to different analyses: B/C (*left*), \bar{p}/p (*center*) and combined (*right*). Published in [12]

and therefore produce less secondaries); (2) on the other hand, a high reacceralation brings low-energy particles to the high-energy part of the spectrum compensating this effect. That's why if one considers the whole energy range it is impossible to obtain a preferred value of δ independently of reacceleration.

We point out that our analysis with $E_{min} = 1 \, \text{GeV/n}$ re-obtains—in the high-reacceleration case—the parameters of the conventional model adopted in many GalProp-based papers: $v_A = 30 \, \text{km/s}$ and $\delta = 0.33$, but the chi-squared of this model is approximately the same, e.g., of the model with no reacceleration and $\delta = 0.57$; the reason why some authors considered the conventional model as the preferred one is mainly its ability to fit sub-GeV data and the fact that quasi-linear theory points to $\delta = 0.33$ as the value corresponding to a Kolmogorov turbulence.

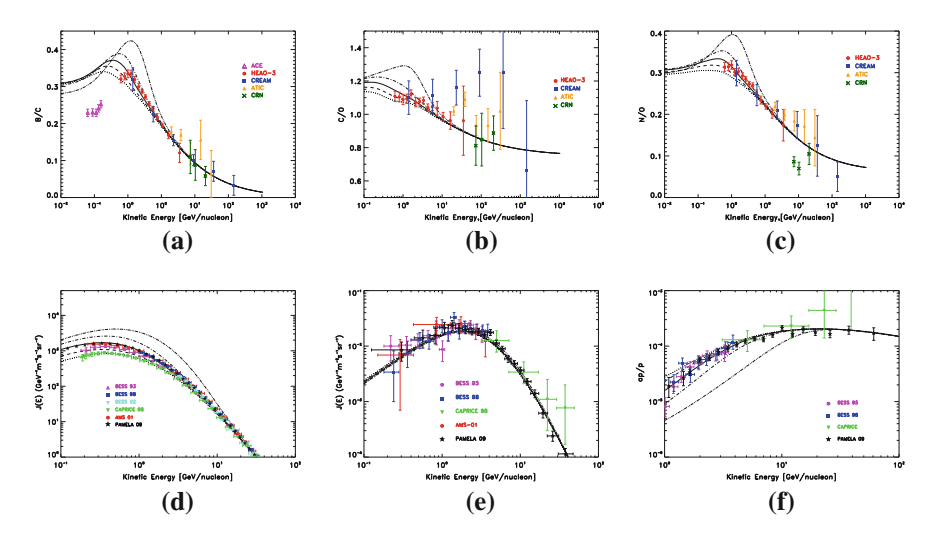


Fig. 4.6 The B/C (a), C/O (b), N/O (c), protons (d), antiprotons (e) and antiproton-to-proton ratio (f) computed with DRAGON for $\delta = 0.45$ and $D_0/z_t = 0.8$ are plotted for several values of v_A and compared with the respective experimental data. *Dotted*, *short-dashed*, *solid*, *dot-dashed*, *long-dashed* correspond to $v_A = 0$, 10, 15, 20, 30 km/s respectively. All plots are published in [12]

Our philosophy is different: we intend to look at high energy where the physics is simpler, keeping in mind that low-energy effects can account for discrepancies with data, and we don't stick to the prediction of quasi-linear theory, so we don't have any *a priori* prejudice on the value of δ to be used: we treat it as a free parameter. With this approach in mind, the B/C analysis makes us conclude that a $\delta \simeq 0.44$ (i.e. the center of the range corresponding to the analysis with $E_{min} = 10\,\text{GeV/n}$) can be taken as the preferred one. Having fixed δ from high energy, we can now look at low energy to set the effectiveness of reacceleration.

To do so, we set δ to 0.4 and vary v_A from 0 to 30 km/s. In Fig. 4.6a, b and c the reader can see the effect of this variation on the B/C, C/O, N/O ratios. It is clear that reacceleration plays a major role in shaping the low energy part of the secondary-to-primary ratios; moreover, a value $v_A = 15$ km/s seems the most adequate to get a good fit over 1 GeV of all the ratios considered.

4.3.3 Discussion on \bar{p}/p and Joint Analysis

Another very powerful and previously unexplored way to break the degeneracy between δ ad v_A that appears in the analysis with $E_{min} = 1 \,\text{GeV/n}$ is considering, together with the B/C, the antiproton-to-proton ratio.

The reader can easily see in the second column of Fig. 4.5 that a large value of v_A is not compatible with the antiproton-to-proton ratio since the tiny allowed region for the \bar{p}/p is not compatible with the B/C best region.

This is mainly due to the behaviour of the *protons*: the reader can verify in Fig. 4.6e that the absolute \bar{p} spectrum is practically unaffected by the value of the Alfvén velocity while the proton spectrum is largely influenced by this parameter and—if the value is high (>20 km/s)—it gets a peculiar shape that is difficult to reconcile with data, whatever modulation potential is adopted (Fig. 4.6d); moreover, also the absolute antiproton spectrum (see Fig. 4.6e) is better reproduced by low-reacceleration models. As we will see below in more detail, in the Literature high-reacceleration models such as the so called *conventional model* adopt a spectral break in the injection spectrum to solve this problem.

Instead, for values of $v_A = 15-20 \,\mathrm{km/s}$ the CLs for B/C and antiproton-over-proton data niceley overlap; it is clear at this point that only a limited range of the Alfvén velocity values is allowed if the combined analysis is taken in consideration: this is a new and interesting result and is well visualized in the third column of Fig. 4.5.

From Table 4.1 another evidence of the importance of the joint analysis can be seen.

The most interesting set of values is—in our opinion—the one corresponding to $E_{min} = 5\,\text{GeV/n}$ since it is the best compromise between the two opposite requirements: (1) to include in the analysis more experimental data and (2) to work in an energy range where propagation is as less as possible affected by poorly known low energy physics. From the analysis performed with this threshold the δ is well constrained in the range [0.36–0.44], almost independently from the value of v_A , and again the best value of the chi-squared appears to be in correspondence with $v_A = 15\,\text{km/s}$.

So, different ways to analyse the B/C and the combined analysis point towards:

- a moderate reacceleration around 15–20 km/s and
- a value of δ quite steeper than the conventionally used 0.33 corresponding to a Kolmogorov turbulence in the quasi-linear scheme.

We will discuss in the following paragraph a particular choice of parameters in this range that will also allow, under some hypotheses on the low energy behaviour of the diffusion coefficient, to fit sub-GeV B/C data.

4.4 Our Preferred Model

In this paragraph we will describe an effective model allowing to fit all available measurements, including sub-GeV data, based on the indications coming from the maximum likelihood analysis.

4.4 Our Preferred Model 51

It is evident from Fig. 4.6a that a model with $\delta \simeq 0.44$ and $v_A = 15$ km/s provides an excellent fit of experimental data above few GeV/n, but below that energy it overshoots the B/C observations.

As we discussed, such a discrepancy may be attributable to a number of effects which, at low energies, introduce degeneracies among the relevant parameters (modulation potential, convective velocity and gradient, if present, low-energy modification of the diffusion coefficient...).

We follow a phenomenological approach tuning only the parameter η (see Eq. 4.1) which sets the dependence of the diffusion coefficient on the particle velocity (a similar approach was followed in [23]). Interestingly we find that the choice $\eta \simeq -0.4$ allows to match light nuclei as well as antiproton data well below 1 GeV/n for almost the same range of δ and D_0/z_t values found for $\eta = 1$.

Indeed, we checked that the $\eta = -0.4$ and $\eta = 1$ CL regions computed for $E_{\text{min}} = 5 \,\text{GeV/n}$ almost coincide (which is not the case for $E_{\text{min}} = 1 \,\text{GeV/n}$).

In Fig. 4.7a-f we show a reference model obtained for $\eta=-0.4$, $\delta=0.5$, $D_0/z_t=0.7$, and $v_A=15\,\mathrm{kms}^{-1}$ that nicely reproduces all relevant data sets in the whole energy range, including also the N/O and C/O ratios (with ~ 6 and $\sim 75\,\%$ injection ratios respectively) as well as the absolute oxygen spectrum. The blue lines correspond to this reference model, while the red lines refer to the GalProp-based conventional model. I will discuss at the end of this chapter the comparison with that model.

The modified dependence of the diffusion coefficient upon rigidity, which is the consequence of adopting a value of η different from 1, can be considered—as anticipated briefly at the beginning of this chapter—as an effective modelization of physics taking place at low energy, including some non-linear phenomena such as the dissipation of magneto-hydrodynamics (MHD) waves by their resonant interaction with CRs [2]. Since this is the same interaction responsible for CR diffusion in the ISM, such an effect is unavoidable at some level. Interestingly, the value of δ used in [2] to fit the B/C in the presence of MHD wave dissipation is 0.5, which is consistent with what we found here (differently from what we do here, however, a break in the injection index was invoked in that work).

4.5 Minimal and Maximal Models

The discussion so far has pointed to a preferred set of values for the propagation parameters. This set allows a good fit of both the B/C, C/O and N/O ratios and the antiproton flux.

Nevertheless, since there is a debate on the possibility that a portion of the antiproton flux is due to exotic sources (e.g. annihilation of Particle Dark Matter, see the forthcoming discussion in Sect. 5.5) it is useful to find—in the range of values allowed by the B/C analysis—the models that minimize and maximize the antiproton flux, as done in [9].

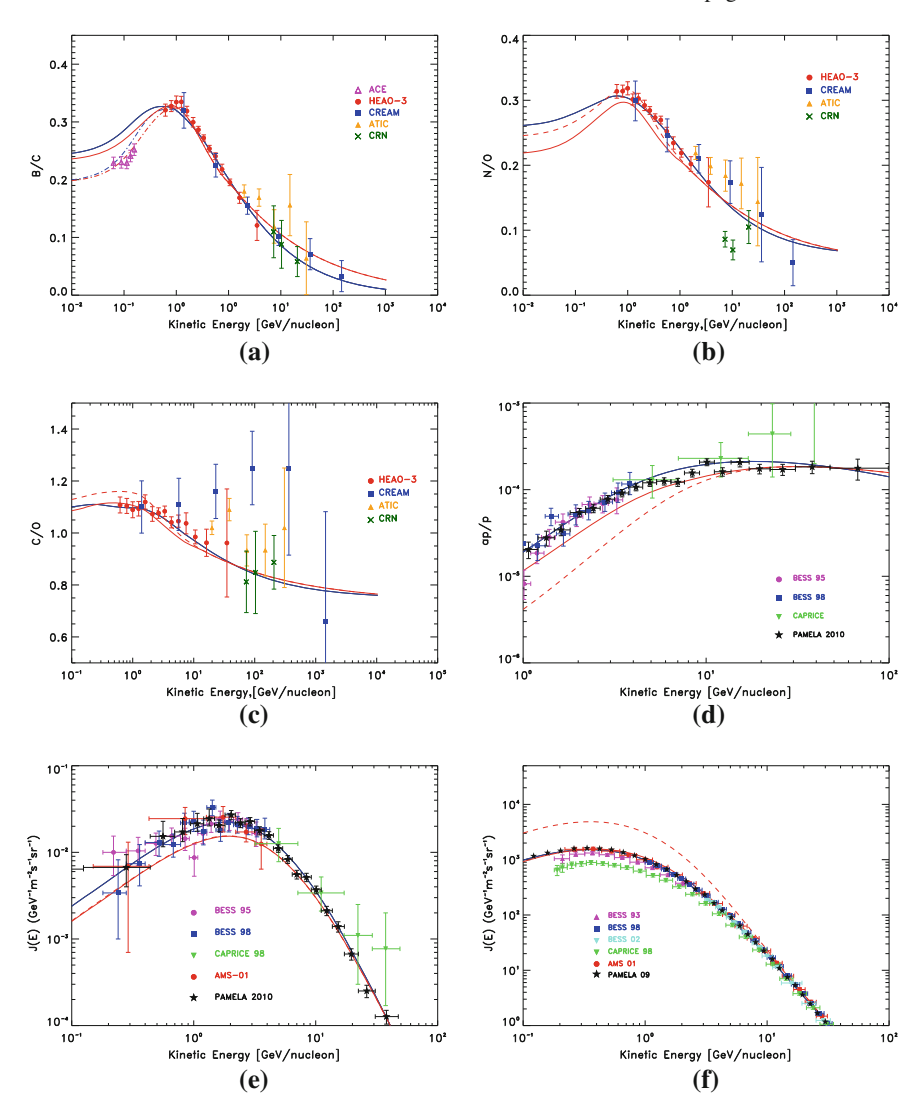


Fig. 4.7 The B/C (**a**), N/O (**b**), C/O (**c**), the \bar{p}/p ratio (**d**), the antiproton and proton absolute spectra (**e** and **f**) computed with our preferred Kraichnan model (*blue solid line*), the Kolmogorov reference model (*red solid line*) and the same model with no break in the CR source spectrum (*red dashed line*), are compared with available experimental data. In both cases we use DRAGON to model CR propagation and interactions (though almost identical results can be found with GalProp). Here we use $\Phi = 450\,\text{MV}$ for the light nuclei ratios to modulate both the Kolmogorov model and our Kraichnan reference models. $\Phi = 300\,\text{MV}$ was used only to match B/C ACE data which were taken in a very low activity solar phase. We use $\Phi = 550\,\text{MV}$ for the proton and antiproton spectra. All plots are published in [12]

For this purpose we define, for each value of v_A considered in the above, a pair of MAX and MIN models that: (1) are compatible with secondary-to-primary ratios above 1 GeV/n within 95 % CL and (2) maximize and minimize respectively the absolute antiproton flux in the range 1–100 GeV.

Among these models, we find that the absolute MAX and the absolute MIN are:

- MAX: $(\delta, D_0/z_t, v_A) = (0.68, 0.46, 0)$; this is a Plain Diffusion model with a steep δ that slightly overproduces antiprotons with respect to data.
- MIN: $(\delta, D_0/z_t, v_A) = (0.30, 1.2, 30)$; this is similar to the conventional model based on Kolmogorov-like turbulence and it slightly underproduces antiprotons with respect to data.

In the next chapter we will adopt both our preferred model and a couple of models similar to MIN and MAX to compute the propagation of leptons with different propagation setups.

4.6 Discussion

4.6.1 Comparison with Other Results

Our analysis points toward a model with $\delta \simeq 0.5$. This value corresponds—in the quasi-linear theory—to a Kraichnan turbulence although, as mentioned above, it may be compatible with a Kolmogorov cascade if non linear diffusion models are considered.

It is interesting to compare our results with other similar findings present in the literature

• The reader may see in Fig. 4.7a and d the predictions of our reference diffusion-reacceleration model $(\delta, D_0/z_t, v_A, \eta) = (0.5, 0.7, 15, -0.4)$ —which for brevity we call *Kraichnan model*—with those obtained using the propagation parameters (and source distribution) of the *conventional model* adopted by GalProp team: $(\delta, D_0(4 \text{ GV})/z_t, v_A, \eta) = (0.33, 1.45, 30, 1)$.

For the conventional model we consider two variants, represented by the solid/dashed red lines, which differ for the presence/absence of a break at a rigidity $R_{\text{break}} = 9 \,\text{GV}$ in the CR nuclei source spectra. The *conventional model* considered in [7] adopts such a break.

It is evident from Fig. 4.7f that—as we anticipated in Sect. 4.3.3—this break is needed in order to reproduce the low energy tail of the observed proton spectrum which otherwise could not be fit for any choice of the modulation potential. It is important to notice that this problem arises in all models with strong reacceleration $v_A > 20 \,\mathrm{km \, s^{-1}}$.

On the other hand our Kraichnan reference model requires a "modified" behavior of the diffusion coefficient at low energy ($\eta=-0.4$ rather than $\eta=1$) which, however, may be motivated by independent physical arguments.

From Fig. 4.7a the reader can see that while both the Kraichnan and conventional models reproduce the B/C equally well, our model provides a significantly better description of the N/O ratio measured by HEAO-3 and CREAM (see Fig. 4.7b). Furthermore, what mostly favors our Kraichnan reference model are BESS, CAPRICE and especially the PAMELA measurements of the \bar{p}/p and antiproton absolute spectrum. Indeed, the discrepancy between low energy antiproton data and the prediction of the 'conventional Galprop model', which was already noted in [7], becomes more compelling due to the new PAMELA data, as shown in Fig. 4.7e.

• The comparison of our results with those of semi-analytical models is more difficult for many reasons.

One of the difficulties lies in the simplified gas and source distribution adopted in those models. We verified, however, that such differences only affect the constraints to D_0/z_t with almost no effect on the determination of δ . We also need to take into account that semi-analytical models assume diffusive reacceleration to take place only in the thin Galactic disk (whose height is z_d), while in the numerical models, as the one presented here, it takes place in the entire diffusion halo. Therefore, in order to compare the values of the Alfvén velocity in those papers with those reported in the above it is necessary to perform a proper rescaling. This is approximatively given by $v_A = v_A^{\rm SA} \sqrt{z_d/z_t}$ [24], with $v_A^{\rm SA}$ being the Alfvén velocity in the semi-analytical models and z_t the half scale height of the Galactic disk.

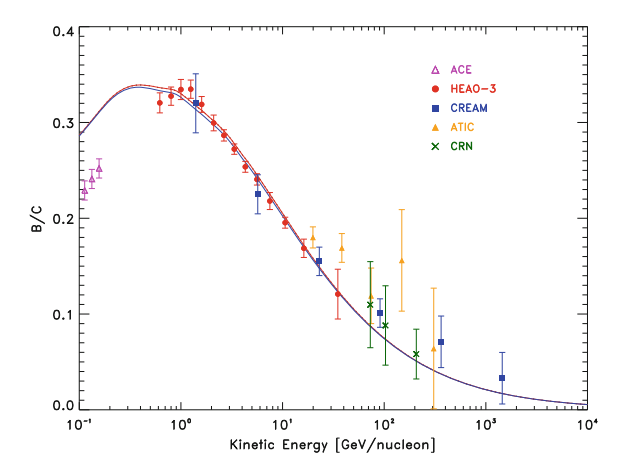
In spite of these differences, and of the fact that that CREAM and PAMELA data were not included in those analyses for chronological reasons, it is comforting that for low values of the convective velocity $v_c \simeq 0$ the preferred value of δ estimated in [4] is in remarkably good agreement with that found in this work: $\delta \simeq 0.45$. Interestingly, the rescaled value of v_A determined in [4] is $v_A \simeq 10$, for $v_c \simeq 0$, which is also in good agreement with our results. It is important to notice that, similarly to what we did in our analysis, no break in the source spectral index was assumed in [4].

We remind the reader again that in the above we always assumed $v_c = 0$ as higher values of that parameter are not required to interpret CR nuclei and antiproton data.

We tested, however, that taking v_c in a reasonable range of values do not affect significantly our constraints on most relevant diffusion coefficient parameters, namely δ and v_A . Indeed, we verified that for various choices of the convective velocity, and of its vertical gradient, it is always possible to rescale the diffusion coefficient normalization D_0/z_t so that both the B/C and the antiproton-to-proton ratio remain almost unaffected above $5 \, \text{GeV/n}$, i.e. the energy range we considered in our analysis. Our tests confirm what is claimed in [6]: namely, that the contribution of convection to the B/C energy slope is negligible, especially in the intermediate and high energy regions.

4.6 Discussion 55

Fig. 4.8 A change in the amount of interstellar gas included in the model reflects in a different normalization of the diffusion coefficient required to fit B/C and other secondary-to-primary ratios: the blue line corresponds to a double amount of molecular gas, and the D_0 has been rescaled by 20% to reproduce the data



4.6.2 Systematic Uncertainties

In our analysis we kept the source and gas distribution and other astrophysical and nuclear inputs fixed. It is important to understand how the uncertainty on these quantities may affect our result.

Maurin et al. [23] analysed in detail various sources of systematic uncertainties that could affect the results of a statistical analysis. We do not aim to repeat this kind of investigation, but I will recall some results from that paper and compare them with our findings.

- Concerning the *source term*, in [23] it is stated that the source slope has negligible effects on the diffusion parameters in plain-diffusion models, and can bring a few percentage change if reacceleration is included. We confirm that the effect of the slope is small (See Fig. 4.3d).
- Concerning the gas, in [23] it is stated that the effect of changing the surface gas density (the authors consider a uniform gas density in the disk) has a small impact on the δ but strongly influences the other parameters. We confirm this and it is evident from Fig. 4.8 that a different amount of gas results in a shift of the normalization of the diffusion coefficient, as anticipated at the beginning of this chapter.
- Concerning the *secondary production cross sections*, in [23] different models are considered (in particular one taken from GalProp and one from Webber et al. [25]) and it is stated that the effect of the uncertainty of the cross-section on the propagation parameters is <20%, although it strongly depends on the presence or absence of convection and, to a lesser extent, on reacceleration; the effect on δ is quoted $\sim 10\%$.
- The low-energy dependence of the diffusion coefficient, according to these authors, strongly affects the results. This in another indication of the importance of a statistical analysis focusing on high-energy data.

In conclusion, we can say that the results of the analysis we performed can be affected by systematic uncertainties that are not easy to estimate; nevertheless, the most important parameter (δ) is less affected by these uncertainties and our choice to perform a energy-dependent analysis contributes to make these effects less important.

References

- K.M. Ferrière. The interstellar environment of our galaxy. Rev. Mod. Phys. 73, 1031–1066 (2001)
- V.S. Ptuskin, I.V. Moskalenko, F.C. Jones, A.W. Strong, V.N. Zirakashvili, Dissipation of magnetohydrodynamic waves on energetic particles: impact on interstellar turbulence and cosmic-ray transport. Astrophys. J. 642, 902–916 (2006)
- L.J. Gleeson, W.I. Axford, Solar modulation of galactic cosmic rays. Astrophys. J. 154, 1011 (1968)
- 4. D. Maurin, F. Donato, R. Taillet, P. Salati, Cosmic rays below Z = 30 in a diffusion model: new constraints on propagation parameters. Astrophys. J. **555**, 585–596 (2001)
- F. Donato, D. Maurin, P. Salati, A. Barrau, G. Boudoul, R. Taillet, Antiprotons from Spallations of cosmic rays on interstellar matter. Astrophys. J. 563, 172–184 (2001)
- A.W. Strong, I.V. Moskalenko, Propagation of cosmic-ray nucleons in the galaxy. Astrophys. J. 509, 212–228 (1998)
- A.W. Strong, I.V. Moskalenko, O. Reimer, Diffuse galactic continuum gamma rays: a model compatible with EGRET data and cosmic-ray measurements. Astrophys. J. 613, 962–976 (2004)
- 8. A.W. Strong, I.V. Moskalenko, V.S. Ptuskin. Cosmic-ray propagation and interactions in the galaxy. Ann. Rev. Nucl. Part. Sci. 57, 285–327 (2007)
- F. Donato, N. Fornengo, D. Maurin, P. Salati, R. Taillet. Antiprotons in cosmic rays from neutralino annihilation. Phys. Rev. D 69(6), 063501 (2004)
- L. Bronfman, R.S. Cohen, H. Alvarez, J. May, P. Thaddeus, A CO survey of the southern Milky Way—the mean radial distribution of molecular clouds within the solar circle. Astrophys. J. 324, 248–266 (1988)
- J.M. Cordes, J.M. Weisberg, D.A. Frail, S.R. Spangler, M. Ryan, The galactic distribution of free electrons. Nature 354, 121–124 (1991)
- 12. G. Di Bernardo, C. Evoli, D. Gaggero, D. Grasso, L. Maccione. Unified interpretation of cosmic ray nuclei and antiproton recent measurements. Astropart. Phys. **34**, 274–283 (2010)
- O. Adriani et al. [PAMELA collaboration], New measurement of the antiproton-to-proton flux ratio up to 100 GeV in the cosmic radiation. Phys. Rev. Lett., 102(5), 051101 (2009)
- H.S. Ahn et al. [CREAM collaboration], Measurements of cosmic-ray secondary nuclei at high energies with the first flight of the CREAM balloon-borne experiment. Astropart. Phys. 30, 133–141 (2008)
- C. Evoli, D. Gaggero, D. Grasso, L. Maccione, Cosmic ray nuclei, antiprotons and gamma rays in the galaxy: a new diffusion model. J. Cosmol. Astropart. Phys. 10 18 (2008)
- M.A. Gordon, W.B. Burton, Carbon monoxide in the galaxy. I—the radial distribution of CO, H₂, and nucleons. Astrophys. J. 208, 346–353 (1976)
- I.V. Moskalenko, A.W. Strong, J.F. Ormes, M.S. Potgieter. Secondary antiprotons and propagation of cosmic rays in the galaxy and heliosphere. Astrophys. J. 565, 280–296 (2002)
- 18. L.C. Tan, L.K. Ng, Parameterization of invariant cross section in p-p collisions using a new scaling variable. Phys. Rev. D 26, 1179–1182 (1982)
- T. Sanuki, M. Motoki, H. Matsumoto, E.S. Seo, J.Z. Wang, K. Abe, K. Anraku, Y. Asaoka, M. Fujikawa, M. Imori, T. Maeno, Y. Makida, N. Matsui, H. Matsunaga, J. Mitchell, T. Mitsui,

References 57

A. Moiseev, J. Nishimura, M. Nozaki, S. Orito, J. Ormes, T. Saeki, M. Sasaki, Y. Shikaze, T. Sonoda, R. Streitmatter, J. Suzuki, K. Tanaka, I. Ueda, N. Yajima, T. Yamagami, A. Yamamoto, T. Yoshida, K. Yoshimura. Precise measurement of cosmic-ray proton and helium spectra with the BESS spectrometer. Astrophys. J. **545**, 1135–1142 (2000)

- M. Aguilar et al. [AMS-01 Collaboration], The alpha magnetic spectrometer (AMS) on the international space station: Part I—results from the test flight on the space shuttle. Phys. Rep. 366, 331–405 (2002)
- J.J. Engelmann, P. Ferrando, A. Soutoul, P. Goret, E. Juliusson, Charge composition and energy spectra of cosmic-ray nuclei for elements from Be to NI—results from HEAO-3-C2. Astron. Astrophys. 233, 96–111 (1990)
- S.P. Swordy, D. Mueller, P. Meyer, J. L'Heureux, J.M. Grunsfeld, Relative abundances of secondary and primary cosmic rays at high energies. Astrophys. J. 349, 625–633 (1990)
- 23. D. Maurin, A. Putze, L. Derome, Systematic uncertainties on the cosmic-ray transport parameters. Is it possible to reconcile B/C data with $\delta = 1/3$ or $\delta = 1/2$? Astron. Astrophys. **516**, A67 (2010)
- 24. D. Maurin, R. Taillet, F. Donato, P. Salati, A. Barrau, G. Boudoul. Galactic cosmic ray nuclei as a tool for astroparticle physics. ArXiv Astrophys. e-prints (2002)
- 25. W.R. Webber, A. Soutoul, J.C. Kish, J.M. Rockstroh, Updated formula for calculating partial cross sections for nuclear reactions of nuclei with Z = 28 and E > 150 MeV/n in hydrogen targets. Astrophys. J. Suppl. Ser. **144**, 153–167 (2003)

Chapter 5 The Leptonic Field

5.1 Introduction

In this chapter I will discuss the leptonic part of CRs: electrons and positrons. This component has been matter of debate because—as I pointed out in the introduction—from recent measurements very interesting signs of either new astrophysical sources or even new physics came out.

The outline of the chapter is the following:

- I will treat the problem of the CR lepton propagation, showing how energy losses are expected to shape the propagated spectrum.
- I will briefly recall the experiments that measured CR leptons before 2008.
- I will discuss the interesting results released by PAMELA and ATIC in 2008 with their scientific implications in terms of previously unaccounted sources or signals of new physics.
- I will present Fermi-LAT measurement of the electron+positron spectrum.
- I will show in detail how we interpreted Fermi-LAT dataset together with PAMELA
 measure of the positron fraction. I will show that an extra component is necessary
 to interpret the data, and I will compare a viable pulsar scenario to some Dark
 Matter scenarios.
- I will anticipate something of the on-going work on the interpretation of recent Fermi-LAT measure of the positron spectrum.

5.2 Propagation of CR Electrons

CR electrons are expected to be produced in SNRs like hadrons; a part of the electrons and and all the positrons (in the standard picture) are instead expected to be secondaries, i.e. produced by protons and heavier nuclei via spallation on IS gas.

The leptonic propagation in the ISM is a bit more complicated with respect to the hadronic one because leptons—due to the low mass—suffer *severe energy losses*; the two main mechanisms are:

• Synchrotron radiation.

It is the electromagnetic radiation generated by a ultrarelativistic charged particle moving through a magnetic field. The radiated power, computed from Larmor's formula, is:

$$P = \frac{4}{3}\sigma_T \beta^2 \gamma^2 \epsilon_B \equiv b(E)E^2 \tag{5.1}$$

where σ_T is Thompson cross section, ϵ_B is the energy density of the magnetic field. The equation above defines the term b(E) that will be used many times in the following.

At fixed energy the synchrotron energy losses are much more effective for an electron than for a proton because $\sigma_T \propto m^{-2}$ and $\gamma = E/(mc^2)$ so $P \propto m^{-4}$. Since $m_e/m_p \sim 1/2000$, an electrons radiates 12 order of magnitude more than a proton with the same energy in a given magnetic field.

A single particle emits a high-energy radiation whose spectrum is peaked at an energy corresponding to the synchrotron angular frequency $\omega_S \propto \gamma^3 \omega_C$ where ω_C is the cyclotron angular frequency.

A collection of particles with non-thermal spectrum described by a power law with index Γ between energies E_1 and E_2 , instead, emits a power-law spectrum with index

$$s = \frac{\Gamma - 1}{2} \tag{5.2}$$

between ω_1 and ω_2 (the synchrotron frequencies corresponding to E_1 and E_2). In Astrophysics the synchrotron emission is observed wherever high-energy electrons are present: pulsars, SNRs, AGNs are typical environments where this radiation is observed, from radio to gamma wavelength depending on the electron energy.

Diffuse CR electrons in the Galaxy also radiate and a diffuse Synchrotron emission is observed in the radio and microwave domain by radio telescopes and space missions such as WMAP and Planck. This emission is an interesting probe for CR lepton propagation models and was recently analyzed 1: the *radio* part of the emission (frequencies $\sim 10{\text -}100\,\text{MHz}$) provides a probe of the interstellar electron spectrum below some GeV, while the *microwave* part of the spectrum (frequency $\sim 10^4{\text -}10^5\,\text{MHz}$) provides an essential probe of the spectrum in the interesting region $10{\text -}100\,\text{GeV}$ where solar modulation is not important. We will not go through the comparison between our models and Synchrotron data but we plan to expand our work in this direction in the future.

¹ See the latest talks by A.W. Strong (http://www.mpe.mpg.de/~aws/talks.html).

• Inverse Compton.

In the well-known process of *Compton scattering* an incoming photon scatters off an electron that is initially at rest with respect to the observer: the electron gains energy and the scattered photon has a frequency lower than that of the incoming photon.

If the electron is ultra-relativistic in the observer's frame and interacts with a lowenergy photon, the process is called *Inverse Compton* scattering. In this case the electron *loses* energy as an effect of the interaction; the photon, instead, gains energy and is shifted to shorter wavelength. Of course the two processes are correlated by a Lorentz boost: the same process seen in the electron rest frame is a standard Compton scattering.

This effect is very common in Astrophysics because high energy CR electrons interact with several background photons of different wavelengths: photons of the Cosmic Wave Background (CMB), plus diffuse IR, optical and UV photons that are the result of the emission by stars and the consequent scattering, absorption, and re-processing of that emission by the dust present in the ISM. These photons constitute the Interstellar Radiation Field (ISRF); a recent model for the energy spectrum and distribution of the ISRF in the Galaxy is described in [1].

The energy loss rate due to IC is given by a formula very similar to the Synchrotron radiating power:

$$P = \frac{4}{3}\sigma_T \beta^2 \gamma^2 \epsilon_{\gamma} \tag{5.3}$$

where σ_T is Thompson cross section, ϵ_{γ} is the energy density of ISRF.

The low-energy photons that interact with CRs are transformed into Gamma-rays. An important component of the diffuse gamma emission from our Galaxy is due to Inverse Compton, as we will see in the last chapter; this emission traces the spatial distribution of both the CR electron population and the ISRF.

A detailed analytical computation of CR electron propagation in the Interstellar Medium can be found in Bulanov and Dogel 1974 [2].

In this paper the authors treat the propagation of CR electrons assuming a cylindrical symmetry.

The source term is taken to be uniform in a thin disk with radius $r_S \simeq 4.5 \cdot 10^{22} \,\mathrm{cm} \simeq 15 \,\mathrm{kpc}$ and half-thickness $h_S = 3-4.5 \cdot 10^{20} \,\mathrm{cm} \simeq 100-150 \,\mathrm{pc}$. The diffusion is assumed to take place in a halo with half-thickness h with intermediate length: $r_S > h > h_S$. The diffusion coefficient is taken as $D = D_0 (E/E_0)^{\delta}$.

A key role in the computation is played by the *energy loss length*, i.e. the distance through which an electron travels, on average, losing $\simeq 50\%$ of its energy. It is given by:

$$\lambda^{2}(E) \equiv \int_{b(E)}^{E} \frac{D(E^{2})}{b(E)} dE^{2} = \frac{D_{0} E^{\delta - 1}}{(1 - \delta) E_{0}^{\delta} \beta}$$
 (5.4)

Here β is the proportionality factor that appears in the energy loss formula for Synchrotron or IC: $\dot{E} = \beta E^2$.

The authors show that the solution of the diffusion-loss equation takes different forms according to the part of the spectrum into consideration. In the following I will recall the results for $\delta < 1$ in different parts of the spectrum and give a qualitative explanation of the results.

• If the energy is low the energy loss length is much larger than the halo:

$$\lambda > h$$

$$E < E_1 = \left(\frac{D_0}{h^2 E_0 (1 - \delta) \beta}\right)^{\frac{1}{1 - \delta}}$$

In this energy range the energy losses are not relevant at all: the electrons fill the entire diffusion halo and their spectrum is steepened from $-\alpha$ to $\alpha_P = -\alpha - \delta$ as for the hadronic case (in which Synchrotron and Inverse Compton never play any role).

The energy E_1 can be estimated, for typical values present in the interstellar medium, of the order ~ 0.1 –1 GeV

• In the intermediate region:

$$h_S < \lambda < h$$
 $E_1 < E < E_2 = \left(\frac{D_0}{h_S^2 E_0 (1 - \delta) \beta}\right)^{\frac{1}{1 - \delta}}$

the spectrum is steepened to $\alpha_P = -\alpha - \frac{\delta}{2} - \frac{1}{2}$.

This result can be motivated qualitatively using the following simplified argument: the number density of particles with energy E that diffuse in a volume V and are affected by energy losses can be approximated as

$$N(E) = Q(E) \tau(E) \frac{V_{\text{sources}}(E)}{V(E)}$$
 (5.5)

where Q is the source term, τ is the energy loss time scale, V_{sources}/V is the ratio between the volume where the sources are located and the volume in which the particles diffuse.

In the energy range we are considering the electrons *do not spread* through all the diffusion halo as the hadrons: the volume they occupy is limited instead by the energy loss length:

$$V(E) = 2\pi r_S^2 \lambda \propto E^{(\delta/2 - 1/2)}$$
 (5.6)

and so, since we have $Q \propto E^{-\alpha}$ and $\tau \propto E^{-1}$, Eq. 5.5 gives:

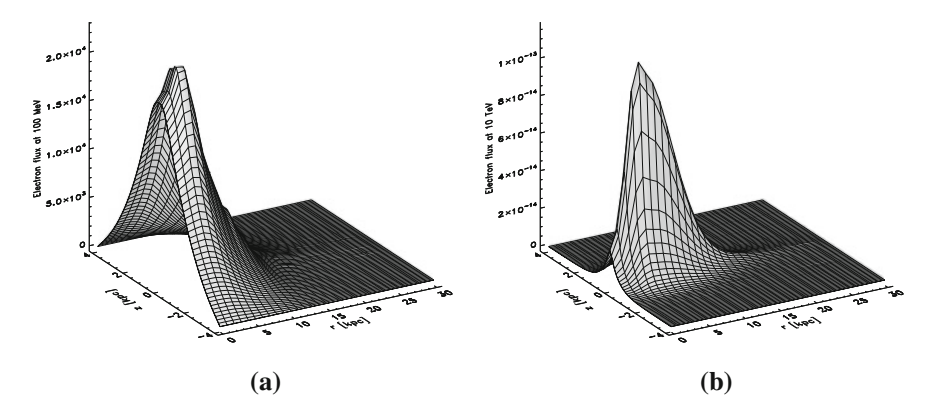


Fig. 5.1 The spatial distribution of CR electrons computed with DRAGON for $E=100\,\mathrm{MeV}$ (a) and for $E=10\,\mathrm{TeV}$ (b) as a function of Galactocentric coordinates R and z. The profile along z appears much broader at $100\,\mathrm{MeV}$, while the very high energy electrons can't get very far from the sources due to the severe energy losses. It is interesting to compare these plots with Fig. 4.2b, c in which the same distribution is plotted for CR protons

$$N(E) \propto Q(E)\tau(E) \frac{V_{\text{sources}}(E)}{V(E)} \propto E^{-\alpha - \frac{\delta}{2} - \frac{1}{2}}$$
 (5.7)

 In the high-energy region the loss length is even smaller than the half-thickness of the source disk:

$$\lambda < h_S$$

$$E > E_2 = \left(\frac{D_0}{h_S^2 E_0 (1 - \delta) \beta}\right)^{\frac{1}{1 - \delta}}$$

Here the energy losses dominate, the particles are confined to a thin volume around the sources and the spectrum is steepened to $\alpha_P = -\alpha - 1$. This can be shown using again Eq. 5.5 and putting $V(E) = V_{\text{sources}}(E)$.

The energy E_2 is very high, of the order of 100 TeV for a source disk with half-thickness <100 pc; so, most experimental data actually lie in the intermediate region.

It is remarkable that, due to energy losses, the volume occupied by electrons gets smaller as the energy increases. This effect is not present for the proton component and can be highlighted making use of numerical codes that solve the diffusion-loss equation. For illustrative purpose we show in Fig. 5.1a, b the electron distribution in the Galaxy at 0.1 GeV and 10 TeV simulated with DRAGON in a Plain Diffusion setup using standard choices of the source term, gas and radiation field distribution: it is evident that at very low energy the electrons diffuse through all the halo while at 10 TeV they remain very close to the thin region along the Galactic plane where the sources are located.

It is very important to point out that for energies larger than some hundreds of GeV it is essential to account for the discrete nature of the sources: in fact the energy loss length is so small that those energetic electrons must be produced in the nearby interstellar medium: a $100\,\text{GeV}$ electron must come from $r<1\,\text{kpc}$ and at $10\,\text{TeV}$ electron from $r<200\,\text{pc}$; these distances are comparable to the mean distance between two SNRs. For this reason it is straightforward to expect fluctuations from a simple power law in the high energy part of the observed spectrum.

On the other hand, we remark that—as for the hadron component—the low energy tail of the spectrum up to some GeV is strongly affected by time-dependent solar modulation.

5.3 Pre-Fermi Measurements of CR Electron and Positron Spectrum

Prior to 2008 the measures of the CR electron and positron spectrum were not very accurate: the statistic was poor and the disagreement between different experiments exceeded one order of magnitude in flux; so, the constraints that could be put on the models describing their origin and propagation were poor.

In 2008 a very exciting time for CR electron measurements began because some very important results were published, some of which were in strong tension with the conventional predictions given by astrophysical models of electron and positron propagations.

The experiments that published in these years on this topic were:

- Payload for Antimatter and Matter Exploration and Light nuclei Astrophysics (PAMELA). It is a space observatory for charged CRs launched in 2006; the instruments mounted on-board are a time-of-flight system, a magnetic spectrometer, a calorimeter, a shower tail counter scintillator and a neutron detector: these devices permit to identify CR light nuclei, protons, antiprotons, electrons and positrons over a wide energy range (~100 MeV-~100 GeV) with high statistics; the presence of the magnet permits to discriminate particles and antiparticles because of the opposite curvature of their trajectories within the magnetic field.
- Advanced Thin Ionization Calorimeter (ATIC). It is a balloon experiment flying in the stratosphere over Antarctica to measure the energy and composition of cosmic rays; the mission started in 2000 and has performed 3 flights so far.
- High Energy Stereoscopic System (H.E.S.S.). It is a system of Atmospheric Cherenkov Telescopes (ACTs) located in Namibia. An ACT works by imaging the flash of Cherenkov radiation generated by the electromagnetic cascade of particles produced when a very high-energy gamma ray strikes the top of the atmosphere. This shower of charged particles, known as an Extensive Air Shower (EAS) is initiated at an altitude of 10–20 km: the incoming gamma-ray photon undergoes pair production in the vicinity of the nucleus of an atmospheric molecule; then, the electron-positron pairs produced—that are of extremely high

energy—immediately undergo Bremsstrahlung or Braking Radiation; this radiation produced is itself extremely energetic, with many of the photons undergoing further pair production iterating the mechanism. Also high energy CR electrons initiate an EAS and can be detected by H.E.S.S.; the energy range covered by this class of experiment is very high (TeV region), where fluxes are so low that space experiments are inefficient due to their small acceptance. Currently there are several ACTs around the world and a new big array of these instruments (named CTA, Cherenkov Telescope Array) is in project.

The most important result was published by PAMELA in the April of 2008; PAMELA reported a measure of the positron-to-electron ratio in the range between 1.5 and 100 GeV.

This measurement—described in [3]—marked an important point in the history of CR measurements.

In fact, the positron-to-electron ratio is expected to *decrease* with energy in the standard scenario in which positrons are merely of secondary origin.

The proof of this statement is quite easy (see e.g. [4]).

- The CR electron after propagation—according to the analytical solution we described above—can be written as $\Phi_{e^-} = E^{-\gamma_e^0 \delta l}$ where γ_e^0 is the *injection* index of the electrons, and $\delta + l$ parametrizes the steepening due to energy-dependent positron diffusion and energy losses.
- Concerning the CR positrons, since they originate from the protons via spallation on IS gas, assuming an energy independent production cross section, their source term is simply $E^{-\gamma_p}$ where γ_p is the *propagated* index of the protons; after propagation their spectrum can be written as $\Phi_{e^+} = E^{-\gamma_p \delta l}$.

So the ratio is proportional to

$$\frac{\Phi_{e^+}}{\Phi_{e^-}} \sim E^{-\gamma_p + \gamma_e^0} \tag{5.8}$$

A rising ratio would require

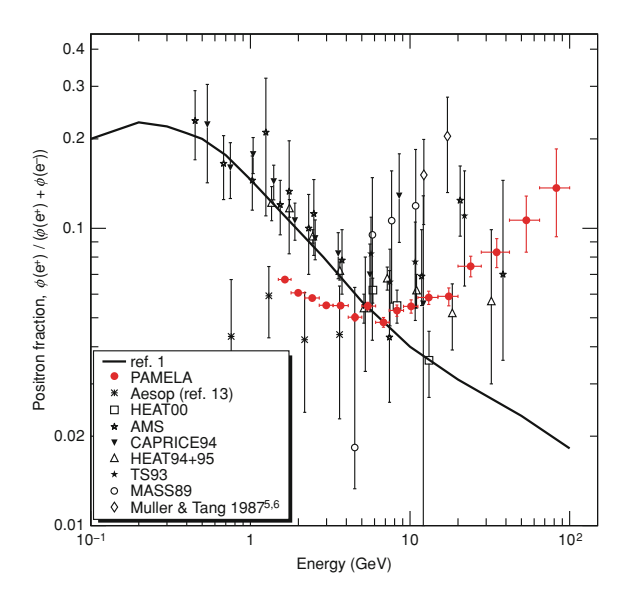
$$\gamma_e^0 > \gamma_p \tag{5.9}$$

i.e. an electron injection slope steeper than the proton *propagated* slope, that seems extremely hard to achieve from a theoretical point of view. So the positron-to-electron ratio is expected to *decrease* with energy.

PAMELA, instead, observed a *rise* in the positron fraction for energies $E > 10\,\text{GeV}$ (in Fig. 5.2 we show the corresponding plot). That arose a very interesting debate in the scientific community in the following 2 years, and a huge number of articles were published on this topic; in the next paragraph I will describe the most interesting proposed explanation for such anomaly.

5 The Leptonic Field

Fig. 5.2 The positron-toelectron ratio measured by PAMELA (*red points*) compared to previous data and to the prediction of conventional CR propagation models. The sharp rise above 10 GeV, and the large excess at high energy that caused a very interesting debate in the Astroparticle community, are evident. Picture taken from [3]



The ATIC collaboration, on its hand, published [5] during the same year an unexpected excess in the electron+positron spectrum with respect to the predicted astrophysical diffuse flux in the range 300–800 GeV. Although the statistics was not so high (the "extra" electron events are \simeq 70) this result, combined with PAMELA observation, showed another interesting hint of either an unaccounted astrophysical accelerator of positrons and electrons or some exotic explanation connected with the problem of Particle Dark Matter.

Concerning the high energy section, instead, the H.E.S.S. measure shows a steepening of the electron spectrum for energies greater than 1 TeV; since in that region the energy losses are very effective, the steepening can be explained by the lack of very nearby accelerators of electrons and positrons.

These three results gave a major contribution to the development of the field; in the next paragraph I will analyse the important scientific implications of these measurements.

5.4 Astrophysical Explanations of the Pre-Fermi Leptonic Excesses

After the release of PAMELA dataset, it was promptly understood that the rise in the positron fraction could be the indication of the existence of a primary astrophysical source (or set of sources) of positrons; in particular Hooper et al. [6] examined the

 $^{^2}$ ATIC does not have a magnet and therefore is not able to discriminate between electrons and positrons.



Fig. 5.3 The Crab Pulsar is a magnetized neutron star spinning 30 times per second; it can be seen in the center of this image taken in X-rays from the orbiting Chandra Observatory. The pulsar rotational energy powers the X-ray emission: the strong induced electric field accelerates charged particles, producing two X-ray jets directed away from the poles and an intense wind in the equatorial direction. Interesting edges are created as the charged particles stream away, eventually losing energy as they interact with the strong magnetic field. The Crab pulsar embeds a mass larger than the Sun in a ultra-compact object whose density is greater than nuclear matter, which is the rest a supernova explosion that was observed by Chinese astronomers in the year 1054. This image is taken from http://apod.nasa.gov/apod/apod/apo81227.html. Credit: NASA/CXC/SAO/F.D. Seward, W.H. Tucker, R.A. Fesen

intriguing possibility that that the observed flux of high energy positrons is the result of electron-positron pair production taking place in nearby and galactic pulsars.

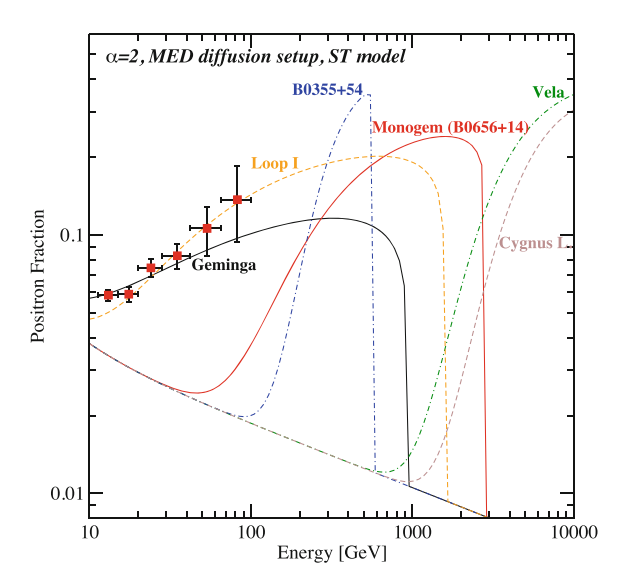
The idea that both the electron and the positron spectrum observed at Earth is the superposition of a *conventional* component (made of primary CR electrons accelerated in SNRs and secondary electrons and positrons produced via spallation) plus some *extra* component dates back to 1995 with the pioneering work of Atoyan et al. [7]. In this paper the authors suggested that the high energy portion of the electron spectrum could be dominated by near ($r < 100\,\mathrm{pc}$) and relatively young ($\tau < 10^5\,\mathrm{year}$) sources; known SNRs located in the nearby were invoked to account for the electron spectrum, but the hints of a rise in the positron spectrum—already present at the time in pre-PAMELA observations—led the authors to argue that pair-production in the magnetosphere of a near pulsar (such as Geminga) could account for both electron and positron extra-component (Fig. 5.3).

Pulsars, indeed, have been known to be potential sources of high energy electrons and positrons for a long time (see e.g. Shen [8], Harding and Ramaty [9]).

Pulsars were discovered in 1967 and, as the name suggests, were observed as periodic radio sources; it was soon realized (independently by Thomas Gold and Franco Pacini in 1968) that these sources are actually rapidly spinning ($P \sim 1-30 \, \text{s}$) neutron stars³ whose magnetic axis is not aligned with the rotation axis; neutron stars

³ A neutron star is the final stage in the evolution of a massive star: the life cycle of stars more massive than 8–10 solar masses ends with a Supernova Explosion; the shock wave continues to

Fig. 5.4 Some nearby mature pulsars can explain the PAMELA anomaly. Taken from [10]



have a intense gravitational field because a mass ~ 1.4 Solar Masses is concentrated in a sphere with a radius ~ 10 km; moreover, they have a very strong dipole magnetic field ($\sim 10^{12} - 10^{14}$ G), so they are an extreme environment where many energetic phenomena can take place (Fig. 5.4).

Their rapid rotation induces an electric field that—in some regions—is able to accelerate electrons and nuclei parallel to magnetic field lines: these particles emit curvature gamma photons that produce electron+positron pairs, which on their hand are able to radiate additional gamma rays via synchrotron radiation: the resulting electromagnatic cascade is able to produce $\sim 10^4$ pairs per primary particle which streams out of the magnetosphere into the surrounding nebula [9].

The details of this mechanism are difficult to model, and the efficiency of the conversion of the pulsar rotational energy into the $e^+ + e^-$ kinetic energy is not known; nevertheless, Hooper et al. [6] showed that a small number of nearby mature pulsars, such as B0656+14 (Monogem) and Geminga, could each plausibly generate the observed flux of positrons under simple and reasonable hypotheses:

- The $e^+ + e^-$ spectrum coming out of the sources is modelled as a power-law with spectral index 1.5 with exponential cutoff;
- Order of a few percent of the pulsars' spin down power is required to be transferred into the production of electron-positron pairs.

Another attempt to interpret ATIC and PAMELA data in terms of pulsar emission came from Profumo [10].

⁽Footnote 3 continued)

propagate in the interstellar medium forming a Supernova Remnant and accelerating Cosmic Rays, while a compact object with very high density made of neutrons remains.

This author considered the pulsars listed in ATNF catalogue [11] available online at [12] and showed how, under simple assumptions on their energy output and efficiency, the PAMELA positron excess is likely to come from a set of mature (age $\sim\!10^6\,\rm year)$ and nearby pulsars while ATIC peak requires a powerful young source. The paper shows how it is unlikely that a single source can originate both excesses but an analysis of the age-distance parameter space shows that some areas are compatible with both datasets and a collection of known objects could account for both measurements.

As I will explain in detail, some aspects of this interesting analysis were used in our Fermi interpretation paper.

5.5 Dark Matter Interpretation

5.5.1 Introduction

Although simple and quite natural, the pulsar interpretation is not the only one. In fact, PAMELA excess, together with ATIC peak, was recognized by many authors as an indirect observation of Particle Dark Matter.

It has been known for a long time that some kind of unobserved matter is needed to explain a large number of observations. First of all, the rotation curves of most galaxies are flatter than expected applying Newton law of dynamics if only the visible star and gas distribution is taken into account; moreover, the application of the *Virial theorem* to clusters of galaxies leads to an unobserved amount of mass that exceeds the visible mass by roughly one order of magnitude; more recently, a spectacular observational evidence of the existence of Dark Matter came from Gravitational Lensing observations, in particular in the Bullet Cluster region [13] where a collision between two galaxy clusters appears to have caused a separation of dark matter and baryonic matter: X-ray observations show that much of the baryonic matter in the system (in the form of a hot plasma) is concentrated in the center of the system, while weak gravitational lensing observations of the same system show that much of the mass resides outside of the central region of baryonic gas.

On even larger scales, in the currently accepted cosmological model known as ΛCDM , ⁴ Dark Matter is a crucial component.

 Λ CDM is a standard cosmological model based on General Relativity: it manages to describe the evolution of the Universe from the beginning to present time.

The model includes a single originating event, the $Big\ Bang$ or initial singularity, followed by an exponential expansion of space by a scale multiplier of 10^{27} or more, known as *cosmic inflation*. The early Universe then continued the expansion

 $^{^4}$ Λ CDM stands for Lambda-Cold Dark Matter; Λ is the cosmological constant: is an important ingredient of the model since it allows an accelerated expansion of the Universe at present time; Cold Dark Matter is supposed to be the most important part of the matter content of the Universe: Cold means that it decoupled in non-relativistic regime.

and remained hot and ionized for several hundred thousand years; when protons and electrons recombined, the optical depth suddenly decreased and the radiation decoupled from matter: this radiation, strongly redshifted, can be observed today as a uniform *Cosmic Microwave Background* (CMB).

The evolution of the Universe obeys Einstein's equation; assuming a Friedmann–Robertson–Walker metric—the most general metric that describes a homogeneous and isotropic space-time—it is possible to derive, from the Einstein's equation, the *Friedman equation*, i.e. the equation describing the evolution of matter and energy content of the Universe:

$$\Omega_M + \Omega_\Lambda + \Omega_k = 1 \tag{5.10}$$

where Ω_M is the energy density associated to matter, Ω_{Λ} is the energy density associated to the cosmological constant Λ (the so called $Dark\ Energy$), Ω_k is the curvature term, equal to 0 in Λ CDM model; all the energy densities are normalized to the $critical\ density\ \rho_C$, i.e. the energy density that is compatible with a flat Universe in absence of a cosmological constant. The measure of these parameters at present time is very important to understand the evolution of the Universe.

The observations of the redshift-versus-distance relation of Supernovae indicate that the expansion of the Universe is accelerating; since it is impossible to obtain an accelerated expansion without a cosmological constant, this observation implies $\Omega_{\Lambda} > 0$.

Another important observable that constrains the cosmological parameters is the Cosmic Microwave Background, in particular the power spectrum of its inhomogeneities. The WMAP collaboration recently released the following values for the Cosmological parameters after 5 years of observations of the CMB [14]:

- The curvature is compatible with 0: the 1σ interval is -0.0179 < k < 0.0081;
- the dark energy component is $\Omega_{\Lambda} = 0.742 \pm 0.030$;
- the baryonic matter is $\Omega_b = 0.0441 \pm 0.0030$;
- the non-baryonic matter is $\Omega_c = 0.214 \pm 0.0027$.

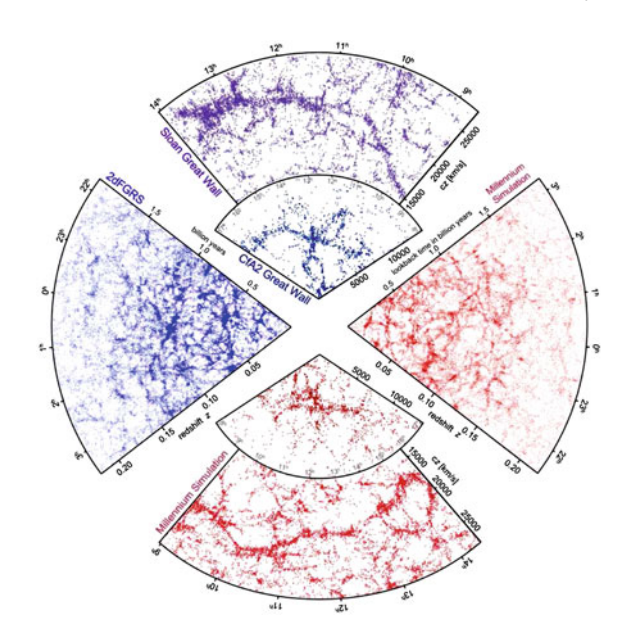
These data clearly show that a large part of the matter content of the Universe (about 80%) is therefore made of some unknown form of unobserved non-baryonic matter (Fig. 5.5).

Nowadays DM is also a crucial ingredient of Structure Formation models: sophisticated numerical codes simulate the evolution of the collisionless DM gas under the influence of gravitational force in an expanding space based on Λ CDM scenario; for example the famous Millennium Simulation⁵ followed the evolution of $\sim 10^{10}$ "particles"—each representing approximately 10^9 solar masses of Dark Matter—and produced the hierarchy of cosmic structures (clusters, superclusters, filaments) that are currently observed in the 3D Galaxy distribution derived by large scale surveys such as the Sloan Digital Sky Survey (SDSS).

⁵ see http://www.mpa-garching.mpg.de/millennium/.

⁶ see http://www.sdss.org/.

Fig. 5.5 Amazingly the simulated large-scale structure of the Universe, based on ΛCDM paradigm, is able to reproduce all the cosmic structures and substructures appearing in large-scale 3D surveys that map 3D distributions of the Galaxies in the observed Universe. This is a spectacular example of how Dark Matter is a fundamental ingredient in Cosmological Models. Picture taken from Springel et al. [15]



Although the evidences of its existence are numerous, no one knows what DM is actually made of. It was argued that a diffuse gas of some kind of exotic massive, neutral, weakly interacting particle (a WIMP: Weakly Interactive Massive Particle) could be a good DM candidate.

Noticeably, it is possible to show that a WIMP with a mass $\sim 100\,\text{GeV}-1\,\text{TeV}$ that comes out of the equilibrium in a non-relativistic regime (this is the so-called *Cold Dark Matter* scenario) can provide the required energy density to match the cosmological observations: this is the so called *WIMP miracle*. In fact, the observed energy density at present time for a generic particle, normalized to the critical density, is

$$\Omega_0 = \frac{n_0 M}{\rho_C} = \frac{n_D \left(\frac{T_0}{T_D}\right)^3 M}{\rho_C} \tag{5.11}$$

where n_D numerical density at decoupling. Since the decoupling occurs when the expansion rate of the Universe H_D overcomes the annihilation rate of the particle with its antiparticle: $n_D \sigma v = H_D$, one obtains

$$\Omega_0 = \frac{H_D \left(\frac{T_0}{T_D}\right)^3 M}{\rho_C \sigma v} \tag{5.12}$$

Simple calculations permit to obtain a value of $< \sigma v > \simeq 10^{-26} \, \mathrm{cm}^3/\mathrm{s}$ for the velocity-averaged annihilation cross section of a hypothetical WIMP that contributes

to most of the observed DM density. Since for weak interaction $\sigma \propto g_W^4 M^{-2}$ this cross section is compatible with a particle with $M \sim 100-1000\,{\rm GeV}$.

A natural candidate for such a particle comes from Super-Symmetric theories. Supersymmetry is a symmetry that relates elementary particles of one spin to other particles that differ by half a unit of spin and are known as *superpartners*. In a theory with supersymmetry, for every type of boson there exists a corresponding type of fermion with the same mass and internal quantum numbers, and vice-versa. Supersymmetry is expected to be spontaneously broken so that all the superpartners have masses much greater than the particles that are currently observed and for this reason nobody has observed them so far. Moreover, if R-parity⁷ is conserved, the Lightest Supersymmetric Particle (LSP) is expected to be stable and may be a WIMP candidate. In most models the LSP is mostly *B-ino* (superpartner of the hypercharge gauge boson field B), possibly mixed with neutral *W-ino* (superpartner of the weak isospin gauge boson field W_0) and/or neutral *Higgsino*. The mass of such a particle is unknown, although it is naturally expected to lie in the range of the electroweak scale ($\sim 200 \, \text{GeV}$).

5.5.2 Interpretation of PAMELA and ATIC Data

Cosmic Rays enter this fascinating field because the existence of these massive particles permeating the Universe, and therefore also our Galaxy, could bring observable effects. In particular, annihilation or decay of such particles could give rise to high energy Standard Model particles and add a new detectable component to the Cosmic Ray flux.

For this reason, immediately after PAMELA measurement was released, many authors claimed that this measure is compatible with a DM scenario.

For example Cirelli et al. [16] performed a model-independent analysis that took into account PAMELA, ATIC data on electrons and positrons, and also PAMELA antiproton data. This paper followed a phenomenological approach: a generic WIMP is considered and the mass, annihilation cross section and primary annihilation channels are treated as free parameters. The results can be seen in Fig. 5.6:

- (1) a DM particle with $M=150\,\mathrm{GeV}$ decaying into W^\pm (compatible with a Wino) may reproduce the positron fraction but also produces an unobserved large amount of antiprotons;
- (2) a TeV DM annihilating into μ^{\pm} is able to reproduce both PAMELA positron fraction and ATIC peak, being also compatible with antiproton measurements;
- (3) a heavy (10 TeV) DM particle annihilating into W^{\pm} reproduces PAMELA positron fraction and produces a sharp feature in the antiproton spectrum in

⁷ R-parity is a symmetry acting on the Minimal Supersymmetric Standard Model (MSSM) fields; all Standard Model particles have positive R-parity while supersymmetric particles have negative R-parity. So, if R-parity is conserved, a supersymmetric particle cannot decay into a set of SM particles: for this reason the lightest supersymmetric particle (LSP) must be stable.

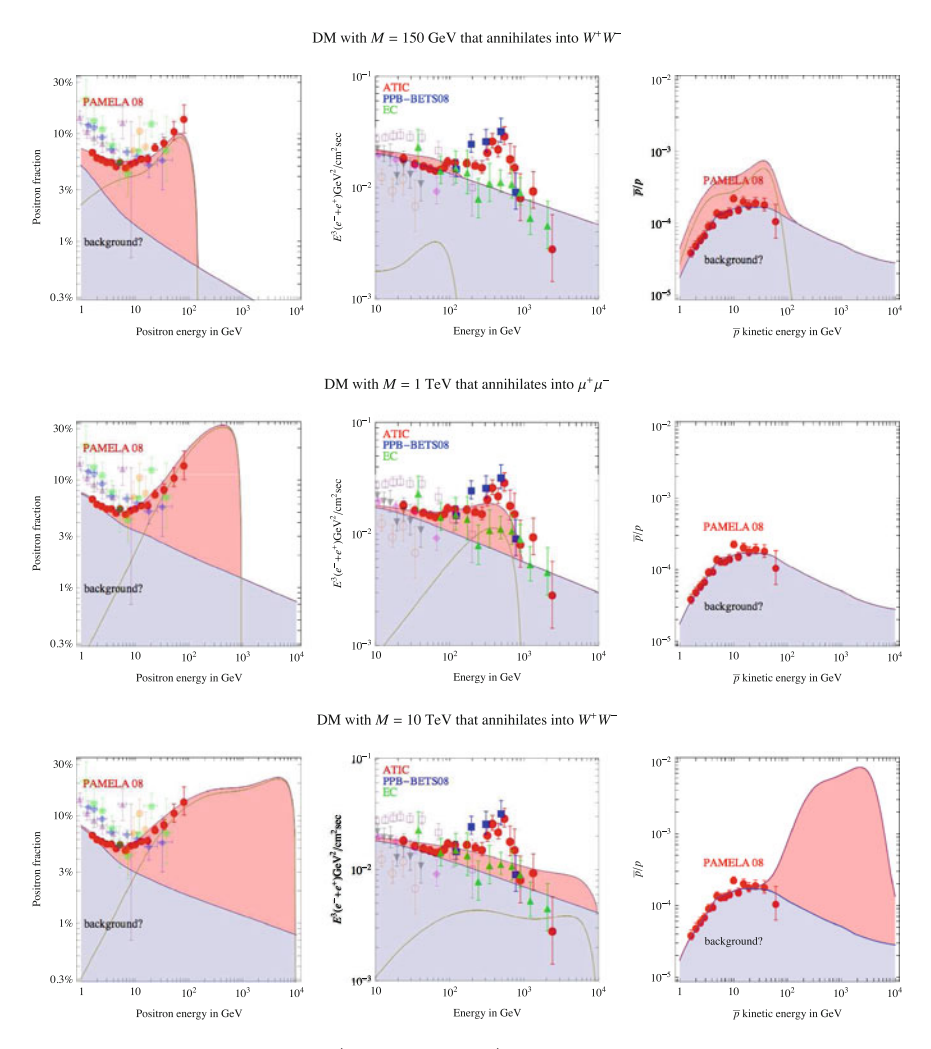


Fig. 5.6 Three examples of ts of e^+ (*left column*), $e^+ + e^-$ (*center*), \bar{p}/p (*right*) data, for the three cases discussed in the text: $M = 150 \,\text{GeV}$ (*upper row*), $M = 1 \,\text{TeV}$ (middle row, favored by data), $M = 10 \,\text{TeV}$ (*lower row*). Taken from Cirelli et al. [16]

an unexplored energy range ($E>100\,\mathrm{GeV}$). This scenario is disfavoured by H.E.S.S. data on the e^++e^+ specrum at high energy.

The conclusion, also supported by many other works, is that a DM candidate that produces the desired amount on positrons must be either leptophilic (i.e. annihilate into leptons, case 2) or very heavy (>10 TeV, case 3), otherwise an excess of low-energy antiprotons is produced, in tension with PAMELA observations. This is a very challenging requirement for DM models since a natural supersymmetric scenario is

not compatible with multi-TeV DM particles (the scale of symmetry breaking should be the weak scale) and does not suppress hadronic annihilation channels.

More noticeably, PAMELA positron data require an annihilation cross section much larger (~2 orders of magnitude) than that expected from Cosmology (see before). Since we are observing the annihilation *at present time* it is possible indeed that the current low-temperature annihilation cross section differs from the cross section at decoupling; some low-energy enhancements such as the Sommerfeld effect were invoked to explain this discrepancy [16, 17]; nevertheless this is another problem that makes the DM scenario less natural.

5.6 Fermi Measurement of CR Electron+Positron Spectrum

The Fermi Gamma-ray Space Telescope is an observatory designed to perform gamma ray astronomy observations from a circular Low Earth Orbit at 565 km altitude. Fermi was launched on June, 11 2008. The mission is a joint venture of NASA, the United States Department of Energy, and government agencies in France, Germany, Italy, Japan, and Sweden.

The main instrument that Fermi brings on-board is the Large Area Telescope (LAT). The LAT is a multi-purpose observatory to survey the Gamma-ray sky in a very wide energy range, from 20 MeV to 300 GeV: such a high energy was never reached before by space gamma-ray instruments and the window between 10 and 300 GeV was previously completely unexplored because it was too high in energy for space missions and too low for ground-based experiments such as H.E.S.S. I refer to Atwood et al. [18] for a complete technical description of the instrument; here I highlight the main features.

The LAT is a *pair-conversion telescope*, i.e. it reveals gamma-rays by making them interact inside it and form an electron+positron pair. It is composed of a 4X4 array of identical towers that measure the arrival direction and energy of each photon. A LAT tower is made of two modules: a Tracker (TKR) and a Calorimeter (CAL); the TKR module is composed of tungsten converter foils—where a photon can interact and give rise to an electron+positron pair—interleaved with silicon-strip detectors where the electron and positron trajectories are mapped; The CAL, which gives a measure of the converted photon energy, is made instead of 96 CsI crystals arranged in 8 layers: it provides 8.6 radiation lengths for normally incident particles. Noticeably, the Pisa section of INFN gave a major contribution to the construction of the TKR. The TRK array is also covered by a segmented Anti-Coincident detector (ACD) which is useful to veto events coming from ordinary CR; the ACD is able to provide an excellent background rejection tagging >99.97% of charged particles.

Being designed to convert photon into electron+positron pairs, the LAT is also by its nature a detector for electrons and positrons, and its capability of performing very accurate systematic-limited measurement of the spectrum of the leptonic part of CRs has been recognized since the early phases of its design (Fig. 5.7).

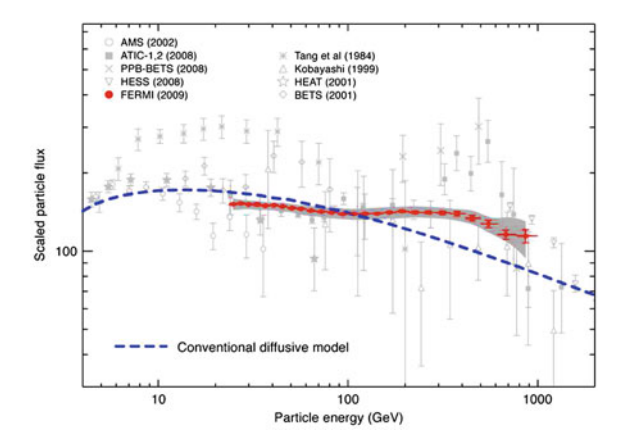


Fig. 5.7 The Electron+Positron spectrum from 20 GeV to 1 TeV measured by Fermi-LAT in 2009 based on 6 months of data taking. Previous datasets are shown in *grey*. Notice the great accuracy of Fermi-LAT measurement compared to previous ones, that were statistical-limited and showed discrepancies one from the other of 1 order of magnitude or more. Fermi-LAT spectrum appears almost featureless and significantly harder than predicted by theoretical models tuned on previous experiments. Notice that at high enery the ATIC prominent feature is not confirmed. Adapted version of the plot published on Phys. Rev. Lett. [19], taken from the Viewpoint published on the American Physics Society website https://physics.aps.org/articles/v2/37

The measure was published in 2009 [19]: the electron+positron spectrum⁸ from 20 GeV to 1 TeV is presented; it is based on 6 months of data taking. The Pisa group had a leading role within the collaboration in the data analysis presented in this paper, which is now widely considered as a real milestone in the history of this kind of measurement. The analysis is described briefly in [19] and explained in more datail in [20] where an update of the data is also presented, with energy range expanded downwards to 7 GeV and an increase in statistics.

The analysis above 20 GeV is particularly accurate because the on-board filter is designed to record ALL events that deposit at least that energy in the calorimeter, including charged particles vetoed by the ACD. These data are the input for a dedicated Event Selection.

The separation of the leptons from the CR protons is very challenging because the CR hadronic flux is dominant and overcomes the leptonic one by 2 orders of magnitude. The procedure can be summarized as follows. Each event is described by a set of variables, and a number of cuts is applied to the most relevant ones to isolate the lepton events. In particular, a powerful discriminator is the lateral shower development: the e.m. showers are more compact than the hadronic ones and a selection on variables that map the distribution of the shower in the TKR and in the

⁸ The measure refers to electrons+positrons since Fermi-LAT does not have a magnet and therefore is not able to distinguish between negative and positive particle, although recently a very interesting method based on the Earth magnetic field permitted to obtain the two spectra seprately: I will mention it at the end of the chapter.

CAL provides a rejection power of $\sim 10^2$. Moreover, a selection on the distribution of hits in the ACD increase the rejection power up to $\sim 10^3$ above 100 GeV. A further boost in the rejection power comes from a method based on Classification Trees (CT). CTs are widely used are used to predict the membership of objects to a particular category from their measurements on one or more predictor variables; in this case two CTs are used, one for TKR variables and one for CAL variables, and the results of these CTs are combined to obtain a resulting rejection power better than $\sim 10^3$ up to $200\,\text{GeV}$ rising above that energy to reach $\sim 10^4$ at $1\,\text{TeV}$.

The events passing the Event Selection and identified as electrons or positrons undergo the Energy Reconstruction which is another tricky step since, for electromagnetic cascades of more than some hundreds GeV, the CAL—due to its limited size—is not able to retain all the energy of the electron+positron pair: so the longitudinal profile must be fitted in order to correct for the energy leakage.

Both the Event Selection and the Energy Reconstruction rely on a sofisticated Montecarlo Simulation that provides a detailed description of the instrument. The MC was verified to be an accurate model for the LAT response with beam test data both for hadrons and electrons up to 282 GeV. Thanks to this analysis the Geometric Factor (GF) as the function of the energy is provided, i.e. the proportionality coefficient between the rate of events passing the selection criteria and the incident flux in physical unit: the GF contains all the information about geometrical acceptance and instrument sensitivity.

With all these tools in hand the procedure to obtain the spectrum is straightforward: the collected events that pass the selection cuts are corrected by subtracting the residual hadronic contamination (less than $10\,\%$ at the highest energy) that was estimated from the average rate of hadrons that survive electron selection in the simulations; then the result is corrected for finite energy redistribution with an unfolding analysis and converted into a flux by scaling with the GF.

This method was applied to 6 months of data taking, from 4 August 2008 to 31 January 2009, and more than $4 \cdot 10^6$ electron events were selected above 20 GeV. Due to this huge number of events, the uncertainty on the measured turned out to be dominated by the systematic, so a precise investigation of this source of error was performed.

The major source of systematic uncertainty is the (slight) discrepancy between the real instrument response and the MC simulation. As sketched in Fig. 5.8, if the MC were perfect, the final spectrum would not depend on the particular choice of the cut value. In the figure a variable that distinguishes electrons and hadrons is considered; the choice c1 corresponds to a very loose selection which does not exclude almost any electron but retains a considerable contamination; instead, the choice c3 corresponds to a very conservative selection which reduces the statistics but provides a dataset with very small contamination. If the MC/data agreement were perfect, the two opposite cases would yield the same spectrum: a more conservative choice of cuts results in a lower subtraction of hadron background but, on the other hand, also a lower GF; on the opposite side, a looser selection needs a high subtraction but also a division by higher GF: in both cases the result would be unaltered. The real situation is different from this ideal scenario and what is observed is a variation of the spectrum

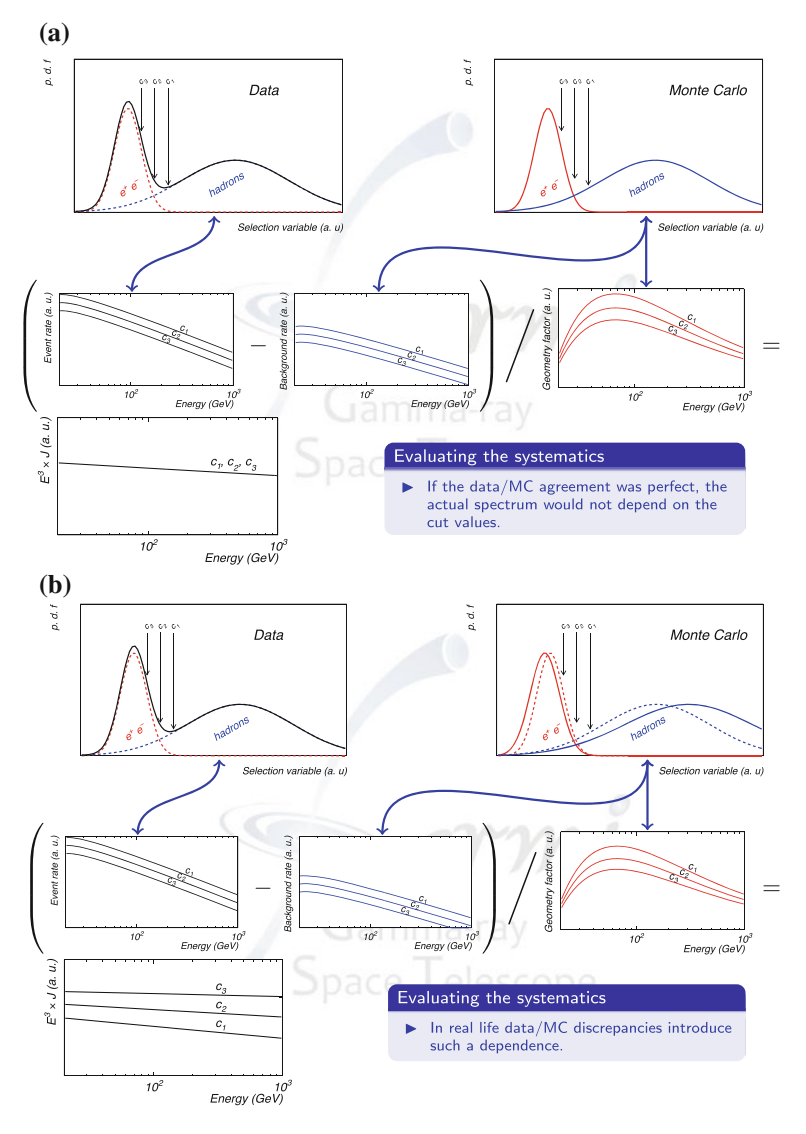
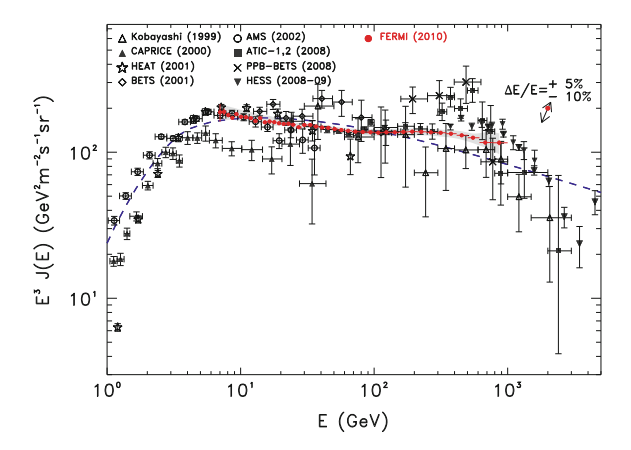


Fig. 5.8 This scheme illustrates the origin of the systematic uncertainty in the $e^- + e^+$ spectrum measured by Fermi-LAT: the position of the cut does not influence the measure if Data and MC perfectly agree (Panel a). If there is some discrepancy, the choice of the cut position reflects in a different measured spectrum (Panel b). Taken From Luca Baldini's talk at RICAP 2009 conference, http://ricap09.roma2.infn.it/slides/Baldini_RICAP09.pdf

according to the cut choice. So what was done by the collaboration is the following. For each step in the event selection a range of thresholds around the reference value used by the cut is scanned and the corresponding flux versus GF curve is derived. Then, the curve to a GF consistent with a null cut is extrapolated and the relative

Fig. 5.9 The Electron+ Positron spectrum from 7 GeV to 1 TeV measured by Fermi-LAT in 2010 based on 12 months of data taking. Taken from [20]



difference between the corresponding flux and the reference is taken as the systematic uncertainty associated with the cut. All such contributions, taken separately with their sign, and the uncertainty of the residual contamination, derived from an overall $20\,\%$ uncertainty in the underlying proton spectrum, are finally summed in quadrature.

The spectrum that comes out of this procedure is shown in Fig. 5.7: it appears to be compatible with a single power-law with spectral index $\gamma=3.045\pm0.008$. The prominent feature observed by ATIC is *not confirmed*, but the slope appears harder than predicted by conventional propagation models tuned on pre-Fermi data, therefore showing an excess in the high energy region with respect to model predictions.

This measure was then updated by the Fermi-LAT Collaboration with an increased statistics, based on one year data, and an extended energy range down to 7 GeV. The complete description on the analysis and the new results can be found in [20]. In the 7–20 GeV region the data are treated differently with respect to the high energy portion because: (1) from a technical point of view, in that energy range the LAT onboard filter does not record all the events that are triggered in the instrument but only provides, for bandwidth reasons, a sample of all trigger types prescaled by a factor 250, and (2) from a physical point of view, the data below 20 GeV are affected by the magnetic field of the Earth: in particular, the lowest energy of primary electrons that can be measured is strongly dependent on geomagnetic position and decreases with increasing geomagnetic latitude. Given Fermi orbit, the magnetic cutoff spans from \simeq 6 to \simeq 15 GeV.

The spectrum is confirmed by this update to be compatible with a single power-law with a spectral index 3.08 ± 0.05 , only slightly softer than the one published in [19]. Hints of a deviation from a pure power-law behavior between 20–100 GeV and at a few hundreds GeV, which were already found in the six month data, are still present in the updated spectrum; moreover, the lowest energy part of the spectrum shows a slight steepening with respect to the highest part. The reader can appreciate these features in Fig. 5.9.

Another important useful piece of information comes from the measure of the level of *anisotropy* of the CR electron+positron flux: the turbulent magnetic field is expected to make the CR flux isotropic, but the presence of a nearby source may reflect in an increased rate of particles towards a particular direction of the sky, so the study of this observable is very important.

In 2010 Fermi-LAT collaboration published a paper [21] on the measurement of anisotropy in the CR $e^+ + e^-$ fluxes. The events corresponding to the first year of Fermi-LAT science operation were analysed; the minimum energy was set to 60 GeV to avoid any spurious effect due to geomagnetic field. A total of 1.6 million electron/positron events were considered. The search was performed using two independent and complementary techniques, both providing a null result. The upper limits on a fractional anisotropic excess ranged from a fraction of a percent (below 100 GeV) to roughly one (at $E \sim 500$ GeV) for the range of angular scales considered.

In the next paragraphs we will see the very interesting implications of Fermi-LAT measurements for the interpretation of leptonic fluxes: first I will discuss the interpretation of the first dataset published in 2009; then I will discuss the second interpretative work on the spectrum from 7 GeV to 1 TeV, including a discussion on the compatibility of our models with the upper limits on anisotropy.

5.7 Interpretation of 2009 Dataset

5.7.1 Single Component Models

Shortly after the Fermi-LAT measurement of CR electron+positron spectrum from 20 GeV to 1 TeV was released, we published [22] an interpretative paper showing the scientific implications of the new dataset combined with previous measurements by PAMELA and H.E.S.S.

First of all, we considered a conventional scenario of CR production and propagation in which primary electrons are accelerated in SNRs and secondary e^+ and e^- production occurs where IS gas is present. The simulations were performed using GalProp, the official CR propagation code adopted by the Fermi collaboration.

As discussed in Chap. 4, the main astrophysical inputs and free parameters for a given model are: the spatial distribution of CR sources, interstellar gas and radiation field; the CR primary injection spectra and abundances; the size of the propagation region; the normalization of the spatial diffusion coefficient D_0 , its distribution through the Galaxy and its dependence on particle rigidity (δ); the effectiveness of reacceleration and convection, if present (v_A , v_C).

Concerning the astrophysical inputs:

• We modeled the *source term* as in GalProp-based papers.

- We took the same *gas distribution* used both in GalProp-based papers and in our DRAGON-based analysis [23] (adopted also in [24] as explained in Chap. 4).
- We used the *ISRF* described in [1].
- We used a spatially uniform diffusion coefficient.

We chose the propagation parameters corresponding to the so-called *conventional* setup, i.e. $\delta=0.33$ (corresponding, in the quasi-linear approximation, to a Kolmogorov-like turbulence), $z_H=4\,\mathrm{kpc}$ as the diffusion halo height, $D_0=5.8\cdot10^{28}\,\mathrm{cm^2s^{-1}}$ as the normalization of the diffusion coefficient, $v_A=30\,\mathrm{km/s}$, no convection. These parameters were shown in several GalProp-based studies to give a satisfactory fit of several CR observables such as Boron-to-Carbon ratio (See Chap. 4) and—if a break is adopted in the injection—they are able to fit most primary species spectra.

The only parameter we chose to tune is the electron injection spectrum: we found that a value of 2.42, harder than the previously adopted 2.54 tuned on pre-Fermi data, allows to reproduce the observed slope of Fermi-LAT spectrum.

We also considered an alternative diffusion setup, with $\delta=0.6$ and no reacceleration and convection, compatible with B/C and other observables (see Chap. 4): in this case, an injection index of 2.33 is required to reproduce the slope of Fermi-LAT spectrum. In both cases a slope of 1.60 under 4 GeV is assumed, as done in pre-Fermi models: we will discuss the necessity of such break in the following paragraph. The two models we proposed are shown in Fig. 5.10 together with a pre-Fermi theoretical prediction (black line).

Figure 5.10 clearly shows that the two models we proposed nicely fit Fermi-LAT dataset from 20 to 1,000 GeV but:

- at low energy they are in tension with AMS-01 and HEAT data below 20 GeV. This discrepancy could be partially explained with a systematic uncertainty of Fermi energy calibration: this may result in a +10 %--20 % rigid shift of the spectrum. Moreover, the uncertainty in solar modulation and in the low-energy injection spectrum could partly account for this difference. Now, after the release of Fermi-LAT data down to 7 GeV and the recent PAMELA dataset at lower energy, the problems with single-component models are even more serious and are hardly explained by these arguments.
- at high energy the H.E.S.S. dataset is not reproduced; this however could be
 explained by the granularity of sources that is not taken into account in our models:
 in the TeV region the length scale on which energy losses are effective becomes
 comparable with the mean distance between sources, and strong deviations from
 a smooth large-scale model are expected; the sharp fall of H.E.S.S. dataset may
 simply be the result of the absence of a very nearby accelerator of TeV electrons.

The effect of source stochasticity, important at high energy, was also evaluated following an analytical approach: the contributions from individual sources were summed to a diffuse background computed with GalProp (Fig. 5.11).

For example, we pointed out that it may be important to consider the fact that—although we live in a inter-arm region as pictured in Fig. 2.1, and thus quite far from

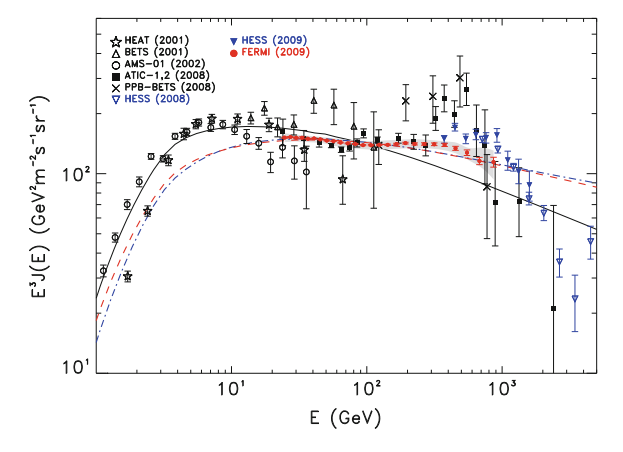


Fig. 5.10 We compare Fermi-LAT CR electron+positron data as well as several other experimental data sets with the electron+positron spectrum modelled with GalProp. The *black continuous line* corresponds to the conventional model used to fit pre-Fermi data. The *red dashed* and *blue dot-dashed lines* are obtained with modified injection indexes in order to fit Fermi-LAT CRE data. Both models account for solar modulation using the force field approximation assuming a potential $\Phi = 0.55$ GV. Published in [22]

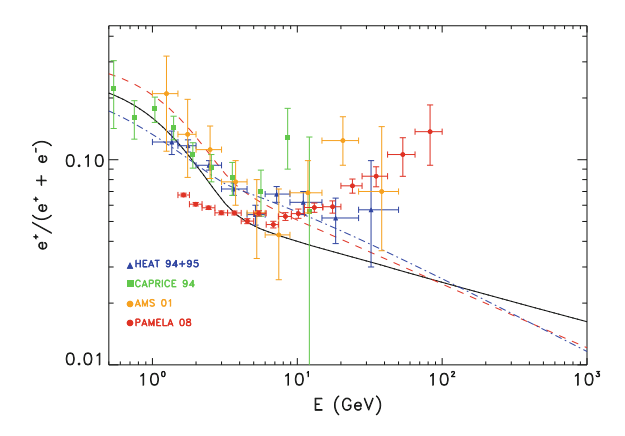


Fig. 5.11 The positron fraction for the same models is plotted against experimental data. The *black continuous line* corresponds to the conventional model used to fit pre-Fermi data. The *red dashed* and *blue dot-dashed lines* are obtained with modified injection indexes in order to fit Fermi-LAT CRE data. Both models account for solar modulation using the force field approximation assuming a potential $\Phi = 0.55$ GV. Published in [22]

the bulk of SN events—the Solar Neighbourhood is located within a ring-shaped region of high star-forming activity: the so-called *Gould's Belt* (Fig. 5.12). The Belt is about 900 pc wide and contains several giant complexes of hot, recently formed O-B type stars; it is considerd as a sort of "local arm" or "local spur" in the inter-arm region where our Solar System lies (see Pohl et al. [25]).

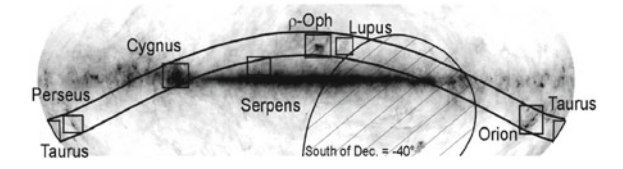


Fig. 5.12 The star-forming complexes belonging to the Gould's belt superimposed to an infrared map of our Galaxy by IRAF. Figure taken from http://www.jach.hawaii.edu/JCMT/surveys/gb/

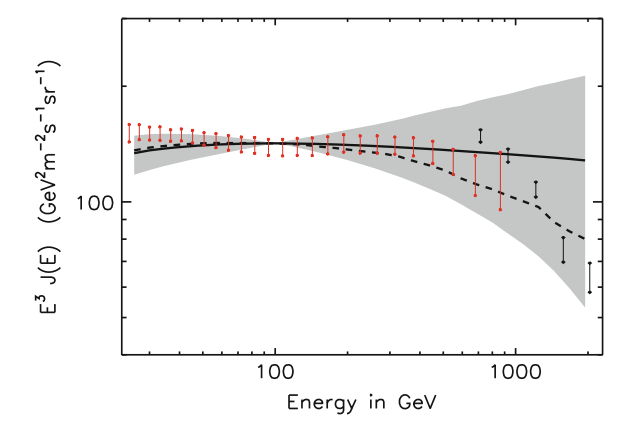


Fig. 5.13 Results of an analytical calculation for stochastic sources, including Gould's Belt (see Pohl et al. [25]). All spectra are normalized to the fiducial flux at 100 GeV. The *solid line* gives the average spectrum that one would obtain, if the sources were continuously distributed. The shaded are indicates the $1-\sigma$ fluctuation range of the electron flux at each energy. The *dashed line* indicates one randomly chosen, actual electron spectrum. Fermi-LAT and H.E.S.S. data points are represented in *red* and *black* respectively. Published in [22]

The main parameters involved in the simple model we presented for the source stochasticity are: (1) the time period during which electrons are released by each SNR (here 20 kyr), and (2) the rate of supernovae as a function of location in the Galaxy, for which we used a time-dependent model of supernovae in the Gould's Belt superposed on a uniform supernova distribution in the Galactic Plane with half-thickness 80 pc.

The Gould's Belt was found to enhance the local SN rate, resulting in marginally harder electron spectra. Figure 5.13 shows, for merely illustrative purposes, the result of this analytical calculation.

However, even taking into account stochasticity and discrete sources, the most important problem with *all* these single-component models is that **the rise in PAMELA positron-to-electron ratio is not reproduced at all**, as seen in Fig. 5.11.

This is a problem of all diffuse models based on standard assumptions; we have already showed in the above that in conventional models it is hard to obtain a rising positron-to-electron ratio.

A detailed study by Delahaye et al. [26] confirmed—using semi-analytical models—that such a rise could not be explained, unless a very soft electron spectrum (index \simeq -3.5) was assumed: this possibility had been considered in pre-Fermi era but, after the very accurate measurement of the electron spectrum provided by Fermi collaboration, this possibility was ruled our and therefore a new kind of interpretation was required.

5.7.2 Pulsar Models

Since in our opinion the simplest way to interpret the PAMELA excess is the presence of a previously unaccounted astrophysical source, we investigated if nearby pulsars could account for both the positron measurements and the new Fermi-LAT electron+positron spectrum.

We modeled a pulsar as a point, bursting source of electrons and positrons. We considered bursting sources because we assumed that most $e^+ + e^-$ pairs are released immediately after the Pulsar Wind Nebula merges with the surrounding interstellar medium, in a short time compared to the total pulsar lifetime; when the pulsar gets older, it gradually slows down and its energy output—and therefore its emission of electrons and positrons—becomes negligible.

So our extra source term is written this way:

$$Q(E, t, \vec{r}) = Q(E) \delta(t - t_0) \delta(\vec{r})$$
 (5.13)

where t_0 is the injection time (the instant in which the particles are released from the source into the ISM), and \vec{r} is the distance to the source.

Since we wanted to consider the contribution of all nearby pulsars from current catalogues, our method consisted in

- Computing analitically the contribution from each object and
- Summing the total pulsar contribution to the standard diffuse component calculated with GalProp.

So, we solved analytically a simplified version of the CRe transport equation:

$$\frac{\partial N_e(E,t,\vec{r})}{\partial t} - D(E)\nabla^2 N_e - \frac{\partial}{\partial E}(b(E)N_e) = Q(E,t,\vec{r})$$
 (5.14)

where $N_e(E, t, \vec{r})$ is the number density of e^{\pm} per unit energy, D(E) is the diffusion coefficient (assumed to be spatially uniform), b(E) the rate of energy loss and $Q(E, t, \vec{r})$ the source term. We neglected convection and re-acceleration, their role

being negligible above $\sim 10\,\text{GeV}$ especially on short $\sim 100\,\text{pc}$ distances. The diffusion coefficient was assumed to have the usual power law dependence on energy $D(E) = D_0 \; (E/E_0)^\delta$. Both normalization and δ were chosen to be the same as adopted in GalProp to model the diffuse component, in order to have perfect compatibility between the continuous and the discrete component.

The general solution of Eq. (5.14) for a point bursting source can be found in Ginzburg and Putskin [27], Atoyan et al. [7]. We considered the particular case of a source term whose energy dependence is taken as a power-law with an exponential cutoff:

$$Q(E, t, \vec{r}) = Q_0 \left(\frac{E}{1 \,\text{GeV}} \right)^{-\Gamma} e^{(-E/E_{\text{cut}})} \,\delta(t - t_0) \,\delta(\vec{r})$$
 (5.15)

and found the corresponding analytical soultion: the details of the calculations are summarized in Appendix C.

In order to perform the calculations, we needed to know for each pulsar its age, distance, and the energy release; the first two parameters could be found in catalogues; we determined the latter by integrating the formula describing evolution of spin-down luminosity over time giving (see e.g. Profumo [10])

$$E_{e^{\pm}} \simeq \eta_{e^{\pm}} \; \dot{E}_{\rm PSD} \, \frac{T^2}{\tau_0} \,,$$
 (5.16)

where $\dot{E}_{\rm PSD}$ is the present time spin-down luminosity determined from the observed pulsar timing, $T=P/2\dot{P}$ (where P is the pulsar period) the pulsar age, and η_{e^\pm} is the e^\pm pair conversion efficiency of the radiated electro-magnetic energy.

For the characteristic luminosity decay time we assumed $\tau_0 = 10^4$ years as conventionally adopted for mature pulsars.

Several almost free parameters are included in the formulas described in the above, i.e.: (1) The pair conversion efficiency $\eta_{e^{\pm}}$; (2) The spectral index of the source term Γ ; (3) The cutoff energy in the source term E_{cut} ; (4) The time after which the e^{\pm} pairs are released in the ISM (i.e., the plerion lifetime Δt).

Since these parameters are loosely constrained by observations, we randomly varied them in a reasonable range for each pulsar. We performed this operation many times, doing a sort of Montecarlo simulation: the results can be seen in Fig. 5.14 for the electron part and in Fig. 5.15 for the positron part (see our article [22] for more details). In the plots, each grey line corresponds to a different combination of the free parameters, and the blue line represents a particular one which nicely fits the data. The figures show the contribution from all pulsar within 3 kpc in ATNF catalogue [11], summed to a diffuse model computed with GalProp, corresponding to the conventional pre-Fermi model (as shown in Fig. 5.10, black line) sligtly rescaled by a 10% factor. From the figures it is quite evident that **the pulsar scenario is compatible with both Fermi-LAT and PAMELA datasets**, while some discrepancy remains with low-energy data, but may be explained with the same arguments discussed previously.

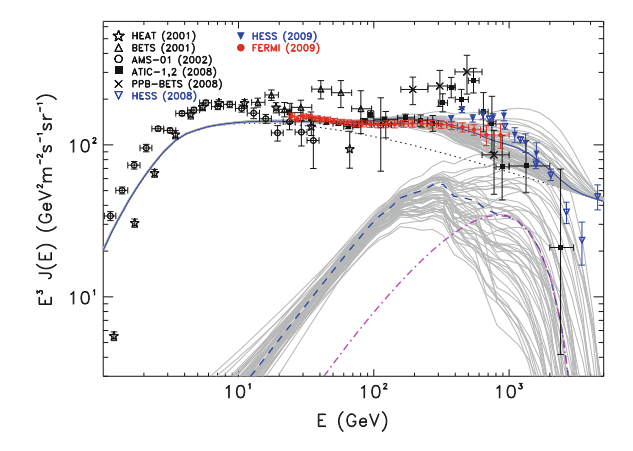
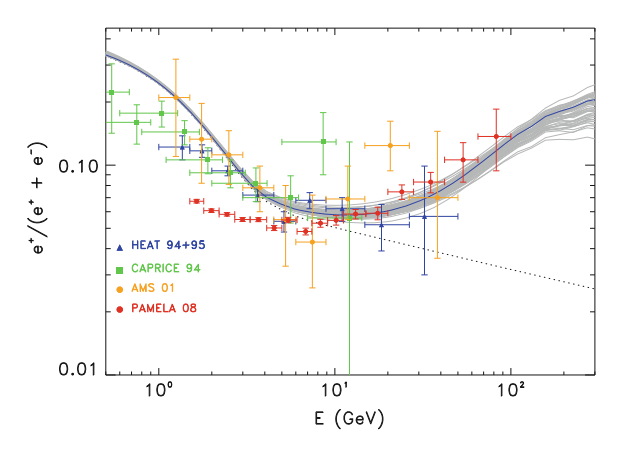


Fig. 5.14 We compare the electron plus positron spectrum from multiple pulsars plus the Galactic diffuse component with experimental data. We consider the contribution of all nearby pulsars in the ATNF catalogue with d < 3 kpc with age $5 \times 10^4 < T < 10^7$ year by randomly varying $E_{\rm cut}$, η_{e^\pm} , Δt and Γ in the range of parameters given in the text. Each gray line represents the sum of all pulsars for a particular combination of those parameters. The blue dot-dashed (pulsars only) and blue solid lines (pulsars+GCRE component) correspond to a representative choice among that set of possible realizations. The purple dot-dashed line represents the contribution of Monogem pulsar in that particular case. Note that for graphical reasons here Fermi-LAT statistical and systematic errors are added in quadrature. Solar modulation is accounted as done in previous figures. Published in [22]

Fig. 5.15 We compare the positron-to-electron ratio predicted by our model that accounts for multiple pulsars plus the Galactic diffuse component with experimental data. Each *gray line* represents the contribution of all pulsars for a particular combination of the parameters, just as in the plot at the left. Solar modulation is accounted as done in previous figures. Published in [22]



The ranges in which we allowed the parameters to vary are: $800 < E_{\rm cut} < 1400 \, {\rm GeV}$, $10 < \eta_{e^{\pm}} < 30 \, \%$, $5 < (\Delta t/10^4 \, {\rm year}) < 10 \, {\rm and} \, 1.5 < \Gamma < 1.9$.

The values we chose were compatible with the few existing constraints at the time.

The range we adopted for Γ is compatible with the synchrotron emission spectra observed by pulsar radio observations as well as with gamma-ray spectra measured

by EGRET in the 0.1–10 GeV range (Thomson et al. [28]) which loosely constrains it in the range 1.4 < Γ < 2.2. In particular, in the case of Crab PWN, it was shown that gamma-ray measurements can be interpreted in terms of IC emission from a population of electrons having a power-law spectrum with $\Gamma \simeq 1.5$ up to ~ 200 GeV, becoming steeper at higher energies, which is very close to that value used here. Since the PWN magnetic field, hence synchrotron energy losses, decrease with the pulsar age, that break is expected to be at much larger energies for mature pulsars (see e.g. Aharonian et al. [29]).

Now Fermi collaboration published new and interesting results, and in the First Pulsar Catalog [30] the discovery of 46 high-confidence pulsed detections based on 6 months of data taking is reported (previously, EGRET had detected 7 pulsars in gamma-rays); in particular, 16 previously unknown pulsars were discovered by searching for pulsed signals at the positions of bright gamma-ray sources or at the positions of objects suspected to be neutron stars based on observations at other wavelengths. It is interesting that the mean spectral index of these sources is 1.46, although the conncetion between the γ -ray spectral index and the electron spectral index is not obvious. Harding and Ramaty [9] stated that these indexes have to be comparable due to the shower nature of the emission, but the further interaction of the electron and positrons with the pulsar wind may radically change the scenario, so this value can't be considered as a solid observational confirmation of the CR electron spectrum we used in the paper that *can't be observed directly in any way*.

As far as the cutoff energy is concerned, I point out that for young pulsars the PWN gamma-ray spectra observed by ACTs have been interpreted in terms of IC emission of electrons with $E_{\rm cut} \approx 10^3$ TeV [31]. That quantity, however, is expected to be considerably smaller for older pulsars as it decreases with the pulsar spin-down luminosity (see e.g. Bueshing et al. [32]).

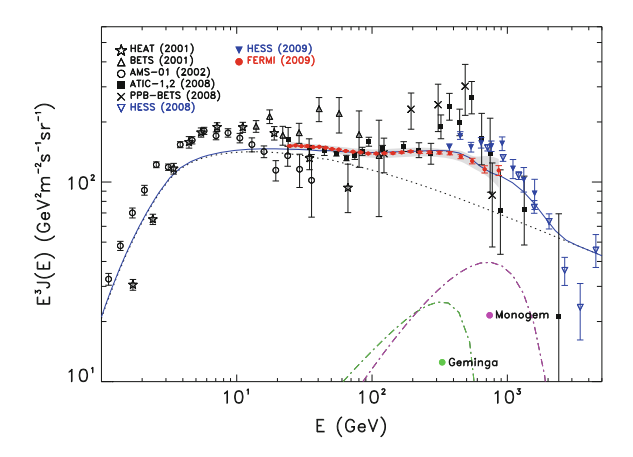
It is important to point out that in our model the dominant contribution at high-energy comes from Monogem (d = 290 pc; T = $1.1 \cdot 10^5$ y. The averaged contribution is shown as the purple dot-dashed line in the plots) and Geminga (d = 190 pc; T = $3.7 \cdot 10^5$ y); conversely, two of the brightest pulsars in γ -ray sky, such as Crab and Vela, do not contribute at all in our model: this is not surprising because they are too young and the electrons and positrons are still likely to be still confined within the Pulsar Wind Nebula; Monogem and Geminga, instead, as the reader may notice looking at Table 5.1, are the most energetic ones (in terms of spin-down power) among nearby, middle aged pulsars and the presence of the the delay between pulsar birth and release of $e^+ + e^-$ makes their emission more recent and thus even more important. Differently from our approach, several other similar works do not consider this delay: so they show a "bumpy" total spectrum due to several contributions from very young pulsars and, in particular, a prominent emission from Vela at high energy that is hard to reconcile with the high-energy part of Fermi spectrum and with H.E.S.S. data (see e.g. [33]).

In Fig. 5.16 we showed that the contribution from Monogem and Geminga alone can account for both Fermi-LAT and PAMELA measurements. I want to emphasize how important is the presence of the exponential cutoff in the source injection spectrum to get a good fit of the data: in fact, if this cutoff is not present, the propagated

| No. | Name | Distance (kpc) | Age (y) | Ė (erg/s) |
|-----|----------------------|----------------|---------------------|---------------------|
| 1 | J0633+1746 (Geminga) | 0.16 | $3.42 \cdot 10^{5}$ | $3.2\cdot 10^{34}$ |
| 2 | J1856-3754 | 0.16 | $3.76 \cdot 10^{6}$ | $3.3 \cdot 10^{30}$ |
| 3 | B0656+14 (Monogem) | 0.29 | $1.11 \cdot 10^{5}$ | $3.8\cdot10^{34}$ |
| 4 | J0720-3125 | 0.36 | $1.90 \cdot 10^{6}$ | $4.7 \cdot 10^{30}$ |
| 5 | B0823+26 | 0.36 | $4.92 \cdot 10^{6}$ | $4.5 \cdot 10^{32}$ |
| 6 | B1133+16 | 0.36 | $5.04 \cdot 10^{6}$ | $8.8 \cdot 10^{31}$ |
| 7 | B1929+10 | 0.36 | $3.10 \cdot 10^{6}$ | $3.9\cdot 10^{33}$ |
| 8 | B2327-20 | 0.49 | $5.62 \cdot 10^{6}$ | $4.1 \cdot 10^{31}$ |
| 9 | J1908+0734 | 0.58 | $4.08 \cdot 10^{6}$ | $3.4 \cdot 10^{33}$ |
| 10 | B0906-17 | 0.63 | $9.50 \cdot 10^{6}$ | $4.1 \cdot 10^{32}$ |
| 11 | B2045-16 | 0.64 | $2.84 \cdot 10^{6}$ | $5.7 \cdot 10^{31}$ |
| 12 | J1918+1541 | 0.68 | $2.31 \cdot 10^{6}$ | $2.0 \cdot 10^{33}$ |
| 13 | J0006+1834 | 0.70 | $5.24 \cdot 10^{6}$ | $2.5 \cdot 10^{32}$ |
| 14 | B0834+06 | 0.72 | $2.97 \cdot 10^{6}$ | $1.3 \cdot 10^{32}$ |
| 15 | B0450+55 | 0.79 | $2.28 \cdot 10^{6}$ | $2.4 \cdot 10^{33}$ |
| 16 | B0917+63 | 0.79 | $6.89 \cdot 10^{6}$ | $3.7 \cdot 10^{31}$ |
| 17 | B2151-56 | 0.86 | $5.15 \cdot 10^{6}$ | $6.4 \cdot 10^{31}$ |
| 18 | B0203-40 | 0.88 | $8.33 \cdot 10^{6}$ | $1.9 \cdot 10^{32}$ |
| 19 | B1845-19 | 0.95 | $2.93 \cdot 10^{6}$ | $1.1\cdot 10^{31}$ |
| 20 | J0636-4549 | 0.98 | $9.91 \cdot 10^{6}$ | $1.6 \cdot 10^{31}$ |
| 21 | B0943+10 | 0.98 | $4.98 \cdot 10^{6}$ | $1.0 \cdot 10^{32}$ |

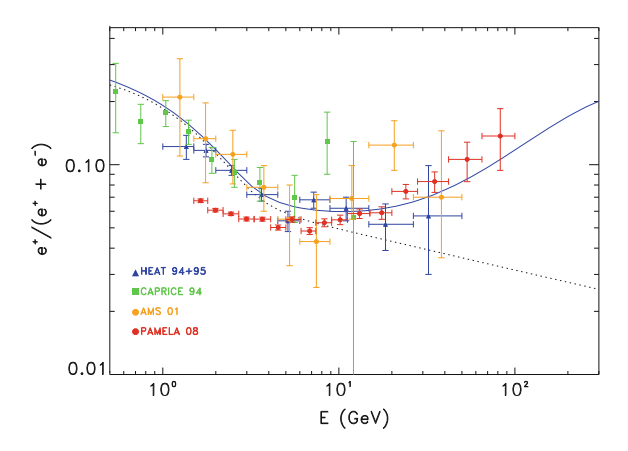
Table 5.1 Relevant paramters for pulsars within 1 kpc

Fig. 5.16 In this figure we represent the electron-pluspositron spectrum computed in a case in which only the dominant contribution from Monogem and Geminga pulsars, analytically computed, is shown as coloured *dotdashed lines*. The *grey band* represents systematic errors on the CRE Fermi-LAT data. Published in [22]



spectrum presents a very sharp feature determined by energy losses at the maximum energy determined by Eq. C.7 in Appendix C; with our choice for the source term, instead, the propagated spectrum is much smoother and shows a much better accord with observed data, differently from other previous works (see e.g. [10]).

Fig. 5.17 In this figure we represent the positron ratio computed in a case in which only the dominant contribution from Monogem and Geminga pulsars is taken into account. Published in [22]



5.7.3 Dark Matter Models

I stress that a Dark Matter interpretation of PAMELA data is far from being excluded, even after that Fermi-LAT did not observe ATIC excess (Fig. 5.17).

Here I will briefly present our efforts to reproduce Fermi-LAT dataset in a DM annihilation scenario (Fig. 5.18 for plots).

The main ingredients that must be set in such interpretation are: (1) the DM density profile; (2) The DM particle mass; (3) The annihilation channel(s); (4) The annihilation cross section.

We assumed for the dark matter density profile ρ_{DM} an analytic and spherically-symmetric interpolation to the results of the high-resolution Via Lactea II N-body simulation (Diemand et al. [34])⁹, namely:

$$\rho_{\rm DM}(r) = \rho_{\odot} \left(\frac{r}{R_{\odot}}\right)^{-1.24} \left(\frac{R_{\odot} + R_s}{r + R_s}\right)^{1.76} , \qquad (5.17)$$

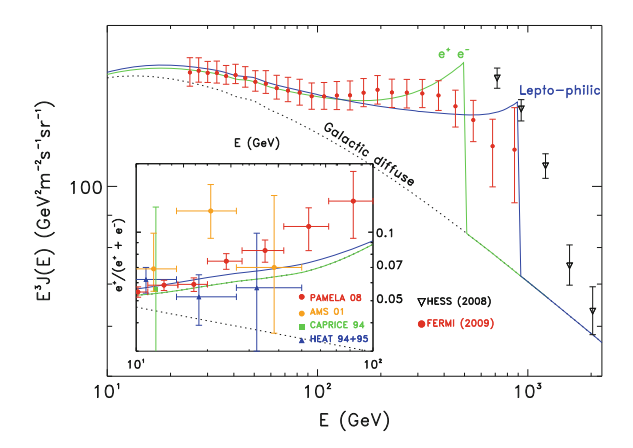
where $\rho_{\odot}=0.37~{\rm GeV\cdot cm^{-3}}$ is the local density, $R_{\odot}=8.5~{\rm kpc}$ is the distance between the Sun and the Galactic center and $R_s=28.1~{\rm kpc}$ is a scale parameter.

For simplicity, we neglected the effect of clumpiness, as well as the possibility of a nearby, dense dark matter sub-halo. We warn the reader, though, that, while very unlikely, the latter possibility may be relevant not only for the normalization of the e^{\pm} produced by dark matter annihilation, but also for the spectral shape.

For illustrative purposes, we focused on three simple benchmark classes of models where the flux of antiprotons are generically suppressed to a level compatible with

 $^{^9}$ Via Lactea simulation follows the growth of a Milky Way-size system in a Λ CDM Universe from redshift 104.3 to the present. The galaxy-forming region is sampled with \sim 10 9 particles of mass \sim 4 times the Solar mass. The simulation reveals the fractal nature of Dark Matter clustering: isolated halos and subhalos contain the same relative amount of substructure and both have cuspy inner density profiles.

Fig. 5.18 Predictions for the CRE spectrum from two specific dark matter models (number 1 and 2 in the text), compared to current measurements. The same large-scale Galactic CRE components (dotted line) as in Fig. 5.16 is used here. Note that the theoretical model curves showed in this plot do not account for the smearing due the finite experimental energy resolution. Published in [22]



the PAMELA antiproton data. Specifically we considered the following ones, similar to those discussed in Sect. 5.5.2:

- (1) **Pure** e^{\pm} **models**: this class of models is defined as one where dark matter annihilation yields a pair of monochromatic e^{\pm} , with injection energies equal to the mass of the annihilating dark matter particle. Notice that dark matter models where the annihilation proceeds into pairs of light intermediate scalar, pseudoscalar or vector particles ϕ , subsequently decaying into light fermion (and possibly only e^{\pm}) pairs (see e.g.[35]), produce a different spectrum from the monochromatic e^{\pm} injection we consider here. Specifically, the resulting e^{\pm} injection spectra have a further dependence on the mass of the intermediate particle ϕ . For simplicity, and in order to maintain our discussion at a phenomenological and model-independent level, we do not consider this possibility here.
- (2) "**Lepto-philic**" models: here a democratic dark matter pair-annihilation branching ratio into each charged lepton species is assumed: 1/3 into e^{\pm} , 1/3 into μ^{\pm} and 1/3 into τ^{\pm} . In this class of models antiprotons are not produced in dark matter pair annihilation. Examples of models where the leptonic channels largely dominate include frameworks where either a discrete symmetry or the new physics mass spectrum suppresses other annihilation channels.
- (3) Super-heavy dark matter models: as pointed out in Cirelli et al. [16], antiprotons can be suppressed below the PAMELA measured flux if the dark matter particle is heavy (i.e. in the multi-TeV mass range), and pair annihilates e.g. in weak interaction gauge bosons. Models with super-heavy dark matter can have the right thermal relic abundance, e.g. in the context of the minimal supersymmetric extension of the Standard Model. We remind here that these models are in strong tension with recent H.E.S.S. data on the electron spectrum in the TeV region.

In our paper [22] a more detailed discussion on these classes of models and a systematic exploration of the parameter space (M, σ) for each case can be found.

Here we only report in Fig. 5.18 two reference choices for the mass and pair annihilation rate for a model annihilating into e^+e^- and for a "lepto-philic" model. For the first case, a mass of 500 GeV and a velocity-average cross section 9×10^{-25} (cm³/s) is used; for the second case, a mass of 900 GeV and a velocity-average cross section 4.3×10^{-24} (cm³/s) is used.

It is clear that, even though Fermi-LAT does not show ATIC bump, it is still possible to fit those data in a DM scenario; the requirements on the cross section remain quite high, so the problems we outlined above connected with this kind of interpretation remain unchanged (unnatural annihilation channels, large boost factors).

5.7.4 Comparison with Other Interpretations

So far we focused on the natural interpretation of the positron excess in PAMELA data as the signature of an extra source of either astrophysical of exotic nature.

Now I want to remind that other explanations for the rise in the positron fraction exist, in which no extra component at all is assumed, but some kind of modification of the standard production/propagation scenario is invoked.

Blasi [37] proposed a model in which the excess in the positron fraction arises because of the positrons created as secondary products of hadronic interactions inside the sources.

The Author focuses his attention on the CR acceleration process at SNR shocks and states that it is unavoidable that secondary electrons and positrons are produced near the shock through hadronic interaction of the freshly accelerated Cosmic Rays and the gas present in the region. In the paper the equilibrium spectrum of $e^+ + e^-$ produced in the acceleration region is computed solving a diffusion equation that takes into account the presence of the shock, the advection with the fluid and the diffusion upstream the shock. The free parameters involved in this calculations are: the fluid velocity upstream the shock u_1 ; the diffusion coefficient upstream the shock (that depends on the intensity of the regular magnetic field and on the turbulence level); the gas density in the acceleration region; the flux of primary protons and electrons at the source. The key result of this computation is that the secondary electrons and positrons produced near the shock (within a distance $\sim D/u_1$) present a harder spectrum with respect to primary species.

Once the secondary leptonic spectrum at the source is computed, the particles are propagated in the Galaxy in a leaky-box scheme. The final result is that these extra secondary positrons produced near the SNR shocks *may explain the PAMELA rise of the positron fraction* for some reasonable choices of the parameters involved.

Another recent paper [36] applied this idea to a realistic distribution of SNRs in the Galaxy. In this paper the normalization of the injection spectrum is fixed by the γ ray flux at high energy observed by H.E.S.S. assuming an hadronic origin for this

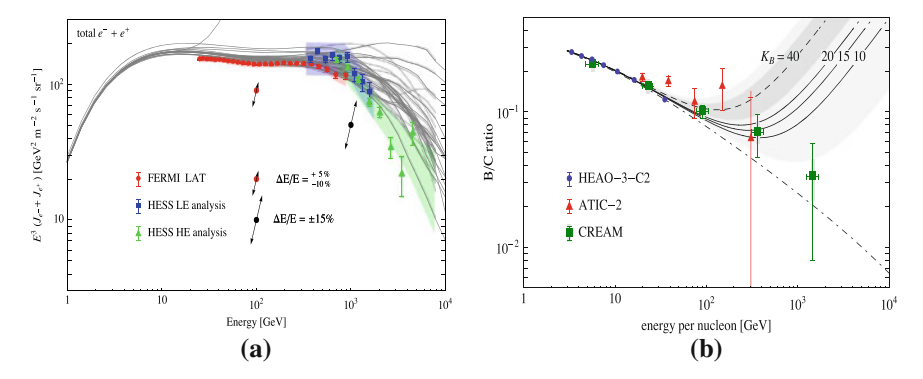


Fig. 5.19 Panel **a**: The electron+positron spectrum calculated in [36] for different realizations of the SNR distribution is shown in comparison with Fermi-LAT and H.E.S.S. data. Panel **b**: The corresponding B/C is plotted against current experimental data

emission. A large number of random distributions of sources drawn from a common probability density function are considered. The results of this MonteCarlo simulation can be found in Fig. 5.19a: noticeably Fermi-LAT and H.E.S.S. datasets are reproduced; moreover, the rising behaviour of the positron fraction is also obtained for several choices of the parameters (see [36]).

Of course the same method can be applied to other secondary products of p-p interactions. In particular a non negligible antiproton flux is expected to be produced by the same mechanism. In [39] this extra flux is computed and is found to be compatible with present data, since it is predicted to become dominant at energies $E > 100 \,\text{GeV}$ where no measurement is available yet.

Also an excess of Boron production is expected from the same mechanism that brings an excess in the positron production. This possibility is discussed in [40] and confirmed in [36]. In Fig. 5.19b the predicted B/C for several values of the free parameter is shown; the predicted upturn at high energy is not compatible with CREAM observation although a hint of a deviation from the standard prediction is found in ATIC data.

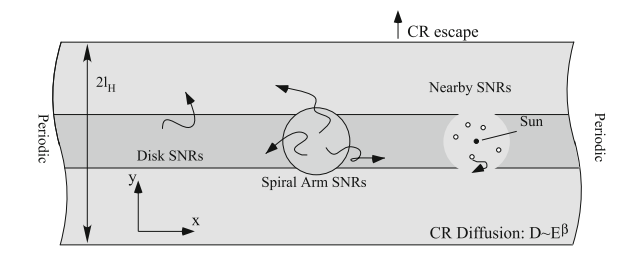
Forthcoming measurements from AMS will help to test the predictions of this scenario concerning the antiproton and the B/C spectra.

Another interesting idea to explain both Fermi-LAT data and the rising positron ratio comes from Shaviv et al. [38].

The idea is represented in Fig. 5.20. In this papers SNRs are considered as the only primary accelerators of CRs, but their concentration along spiral arms is considered. Since we live in a inter-arm region, the nearest regions where the bulk of CR sources are located are about a kpc away, so for energies $E > 10 \,\text{GeV}$ the primary electrons cool via Synchrotron and Inverse Compton before reaching Earth. Primary protons, instead, are of course unaffected by energy losses and are able to reach the Solar System. Secondary positrons and electrons, that are produced via CR proton—gas

92 5 The Leptonic Field

Fig. 5.20 A sketch of the model presented in [38]. See the text for a description



collisions in the nearby ISM, can also reach the Solar System up to high energies increasing the positron/electron ratio.

The model is shown in [38] to reproduce Fermi-LAT and PAMELA data. However, some free parameters were tuned, in particular the SN ratio between the arm to interarm region (set to 10 in that work).

In conclusion, the interesting debate on the anomalous behaviour of PAMELA data, together with the necessity to fit the very accurate Fermi-LAT dataset gave rise to four different scenarios. Here I summarize the main points related to each of them.

- **Pulsar interpretation**. It is quite natural: since PAMELA data suggest the presence of a primary source of positrons, and since pulsars are known to be $e^+ + e^-$ pair emitters, it is straightforward to expect a contribution from nearby pulsars to the positron fraction and to the electron spectrum. The efficiency of pair production in the magnetosphere is unknown, and the model strongly depends on this free parameter. If the model is correct, an anisotropy in the CR electron flux should be detected towards the most energetic nearby pulsars; nevertheless, the presence of unobserved pulsars in other portions of the sky may decrease or cancel this anisotropy so a null result from the anisotropy search does not necessarily disprove this scenario.
- Dark Matter interpretation. Since many different astrophysical and cosmological arguments point towards the existence of an unknown form of non-baryonic, non-shining matter diffusely present in our Galaxy, the hypothesis that the positron excess is a signature of the annihilation or decay of this unobserved matter is very fascinating. It is possible to reproduce the data in a scenario in which a DM particle of mass ~500–900 GeV annihilates into leptons; nevertheless, the high required cross-section and the requirement of a purely leptophilic annihilation channel makes this hypothesis less natural in our opinion.
- Secondary production in the accelerator. This intriguing possibility does not require any extra source. The idea is that the extra positrons are produced within the acceleration sites of CRs, namely the SNR shocks. This scenario has testable consequences: in particular, it predicts an upturn in secondary-to-primary ratios such as \bar{p}/p and B/C; for the B/C this feature has not been observed so far and CREAM data clearly disfavour such a scenario. Future data from AMS will help to test these predictions.

• Role of source inhomogeneity. A model in which CR sources (but not the molecular and atomic gas) are concentrated in spiral arms could in principle reproduce the PAMELA data, according to a recent claim by some authors. This prediction strongly depends on some ad hoc assumptions concerning the arm/interarm ratio of CR sources, the gas distribution, the diffusion coefficient. In particular, it is crucial to assume that most SN events occur in the arms, although a very recent work [41] finds a completely different result. Nevertheless, this is an interesting possibility that needs to be tested more precisely in the future with a realistic model for the gas distribution too. For this reason it is important to push on 3D propagation models in which all effects related to Galactic structures can be taken into account.

5.8 Interpretation of 2010 Dataset and Anisotropy Upper Limits

5.8.1 Introduction

In 2010 several important measurements were published, as described in Sect. 4.4:

- Fermi-LAT spectrum was extended down to 7 GeV as shown in Fig. 5.9: at low energy a steepening is observed, and—although the dataset is still compatible with a power law within systematic uncertainties—hints of a deviation from the single-component scenario appear more evident.
- Some upper limits on the anisotropy of CRE flux were released by Fermi Collaboration.
- New PAMELA and CREAM data on antiprotons and B/C were published, and their implications on CR propagation parameters were extensively studied by our group with DRAGON package, as described in Chap. 4.

These new pieces of information forces us to reconsider and update our interpretative scenario; the new results were published in [42].

Following the previous article, we started our work analysing single-component models.

5.8.2 Single Component Models

First of all we considered three different propagation setups. The parameters of these models are summarized in Table 5.2; these models are chosen in the following way:

• the **PD** model is a Plain Diffusion model with no reacceleration and convection, i.e. $v_A = v_C = 0 \text{ km/s}$; it is quite similar to the MAX model discussed in Sect. 4.5.

| Model | δ | $D_0 (\text{cm}^2 \text{s}^{-1})$ | z_h (kpc) | γ_p | $v_A \text{ (km s}^{-1}\text{)}$ | η |
|-------|----------|------------------------------------|-------------|------------|----------------------------------|--------|
| KOL | 0.33 | 5.6×10^{28} | 4 | 1.6/2.4 | $v_A = 30$ | 1 |
| KRA | 0.5 | 3.0×10^{28} | 4 | 2.25 | $v_A = 15$ | -0.4 |
| PD | 0.60 | 2.4×10^{28} | 4 | 2.15 | $v_A = 0$ | -0.4 |

Table 5.2 Propagation and CR injection parameters for the three reference models

 D_0 is the diffusion coefficient normalization at 3 GV; δ the index of the power-law dependence of D on energy; z_h the half-height of the Galactic CR confinement halo; γ_p the CR nuclei injection index; v_A is the Alfvén velocity; η is the exponent of the power-law dependence of D on the particle velocity β

- the **KOL** is a model based on $\delta = 0.33$ which is known to correspond—in the quasi-linear approximation—to a Kolmogorov model of turbulence; it is quite similar to the MIN model discussed in Sect. 4.5.
- the **KRA** is a model based on $\delta = 0.5$ which—under the same approximation—refers to a Kraichnan model of turbulence. It is our preferred model according to the maximum likelihood analysis presented in the previous chapter.

We point out again that the correspondence between δ and turbulence model may not be valid in the actual interstellar environments where the turbulence level is high, and also the KRA model may be compatible with a Kolmogorov-like turbulent cascade. The other parameters of the model are tuned to reproduce the B/C ratio in the energy range $0.1 < E < 10^3$ GeV; see Fig. 5.21a for a visual comparison of these models and Chap. 4 for a detailed discussion on the CR propagation parameters: we remind here that the KRA model is almost coincident to the model we pointed out as the preferred one in our maximum likelihood analysis, since it provides the best fit of B/C ratio and recent PAMELA antiproton data; the KOL model, instead, which has been widely used in the Literature, seems disfavoured by this dataset, and we will see below that also electron+positron data do not favour high reacceleration models such as KOL.

With these propagation parameters at hand, we start our analysis—as we did for the 2009 dataset—with single component models. We evaluate these models with DRAGON package, and confirm our findings with GalProp: as we pointed out in Chap. 3, if the physical inputs are the same the two codes produce the same results so in the following—since we don't need to explore the radial dependence of the diffusion coefficient—the package we used is not relevant.

We proceed in the following way. For each propagation setup, we start tuning the free parameters involved in the calculation of the CRE spectrum against Fermi-LAT data in the energy range 20–100 GeV, where both statistics and systematics errors are smallest; this choice is also strongly motivated by theoretical arguments: above 20 GeV the uncertainties on the CRE spectrum due to solar modulation are negligible; moreover, below 100 GeV the CRE spectrum is less affected by the uncertainties due to the stochastic spatial and temporal distribution of CRE local sources which become relevant in the TeV energy range.

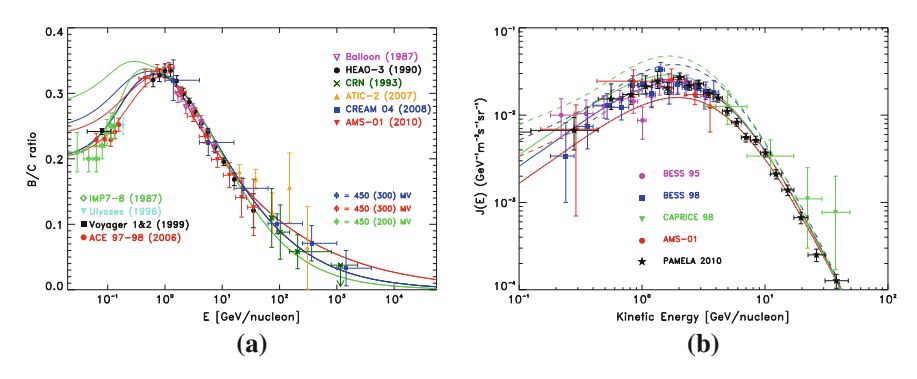


Fig. 5.21 Panel **a**: B/C ratios, as computed with our three reference models given in Table 5.2, are compared with experimental data. Red lines $\delta=0.33$ model (KOL); blue lines $\delta=0.5$ model (KRA); green lines plain diffusion (PD). Solid lines are modulated with $\Phi=450$ MV, which is appropriate for HEAO-3 and CREAM data, while triple-dotted lines have been computed for $\Phi=300$ MV which is appropriate for ACE data. Panel **b**: The theoretical antiproton spectra computed for our three reference models are compared with experimental data. The color notation is the same as in the previous figures. All solid lines are modulated according to the force field scheme assuming the charge symmetric potential $\Phi=550$ MV as required to reproduce the measured proton spectrum at low energies. Dashed lines are the corresponding LIS spectra. Published in [42]

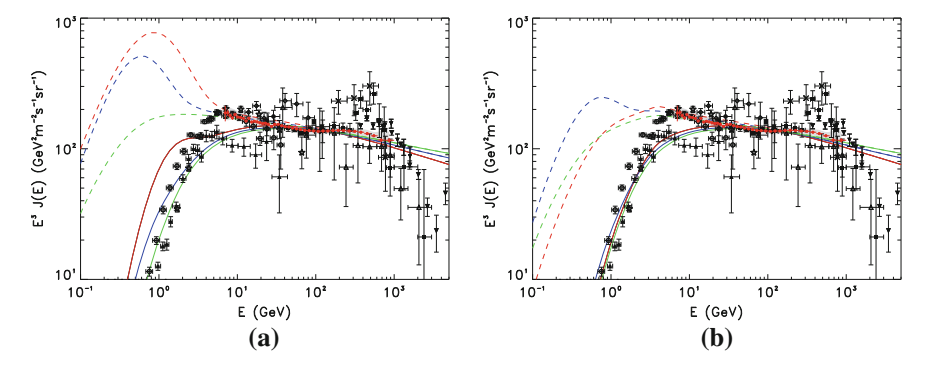


Fig. 5.22 The $e^- + e^+$ spectra computed for single component models with unique injection slopes $\gamma = 2.45, 2.37, 2.32$ (panel a) and broken power-law $\gamma = 1.6/2.4; 2.0/2.37; 2.32/2.32$ below/above 2 GeV for the KOL (red), KRA (blue) and PD (green) diffusion setups respectively (panel b). Fermi-LAT data are represents by the red points. See Fig. 5.23a, c, e for the other experiment's symbols. Modulated lines (solid curves) have been computed in the force field framework with $\Phi = 550$ MV; dashed lines are the corresponding local interstellar (LIS) spectra. Plots published in [42]

We find that above 20 GeV the injection spectral indexes $\gamma = 2.45, 2.37, 2.32$, respectively for the KOL, KRA and PD models, are adequate to reproduce Fermi-LAT data (see Fig. 5.22a, b).

Problems appear, however, when considering lower energy data.

A discrepancy between low energy pre-Fermi data and the prediction of single component models was already noticed in 2009 dataset and tentatively ascribed e.g. to systematics experimental errors or to effects of solar modulation; that interpretation, however, does not hold against the new Fermi-LAT data between 7 and 20 GeV which agree with AMS-01 and HEAT data and are clearly incompatible with the results of the above models (see Fig. 5.22a, b).

It is worth noticing at this point that reacceleration models need spectral breaks to correct for an anomalous behavior which would otherwise arise in the propagated LIS spectrum and is shown in Fig. 5.22a (dashed lines). The reason of such a behavior can be traced back to the combined effect of reacceleration and energy losses: reacceleration shifts electrons from the low-energy to the high-energy region of the spectrum, while energy losses take electrons from high to low energy; the two effects have comparable strength in the GeV region and give rise to pronounced bumps in the unmodulated spectra if a single power-law is assumed. This feature is more evident in models with strong reacceleration (as in the KOL model), and must be treated by introducing a sharp, and hardly justifiable, break in the injection, as shown in Fig. 5.22b. On the other hand, the KRA model, in which only moderate reacceleration is present, requires a smoother break. No break at all is required for the PD model.

A reasonable fit of the CRE spectrum measured by Fermi-LAT at low energy is possible if we choose to normalize the models to data at $10\,\text{GeV}$ (rather than $100\,\text{GeV}$) and adopting injection spectra slightly steeper than those reported in the above (2.50 rather than 2.45 in the KRA model, 2.43 rather than 2.37 for the KOL model). The results are shown in Fig. 5.23a, c, e: it is clear that the models obtained in this way are not able to reproduce the spectral features seen by Fermi-LAT and poorly reproduce the data in the region around $100-200\,\text{GeV}$ where the accuracy of the measure is at its maximum. Concerning positrons (see Fig. 5.23b, d, f), it is clear that: (1) Below $10\,\text{GeV}$ the $e^+/(e^-+e^+)$ measured by PAMELA can be reproduced by the KRA and PD models while the fit is unsatisfactory for the KOL model: again, low reacceleration models seem to provide a better description of low energy experimental data; (2) None of the single component realizations can reproduce PAMELA rise above $10\,\text{GeV}$.

We summarize what discussed above pointing out again the main problems of single component models.

- they are unable to reproduce all the features revealed by Fermi-LAT in the CRE spectrum, in particular the flattening observed at around 20 GeV and the softening at ~500 GeV. If, as they should, such models are normalized against data in an energy range where systematical and theoretical uncertainties are the smallest, they clearly fail to match CRE Fermi-LAT and PAMELA data below 20 GeV. If they are normalized at 10 GeV to repdroduce the low energy part, they fail to reproduce the region where uncertainties are the smallest.
- As explained many times, they cannot reproduce the rising positron-to-electron ratio measured by PAMELA at high energy. Therefore, if PAMELA observations

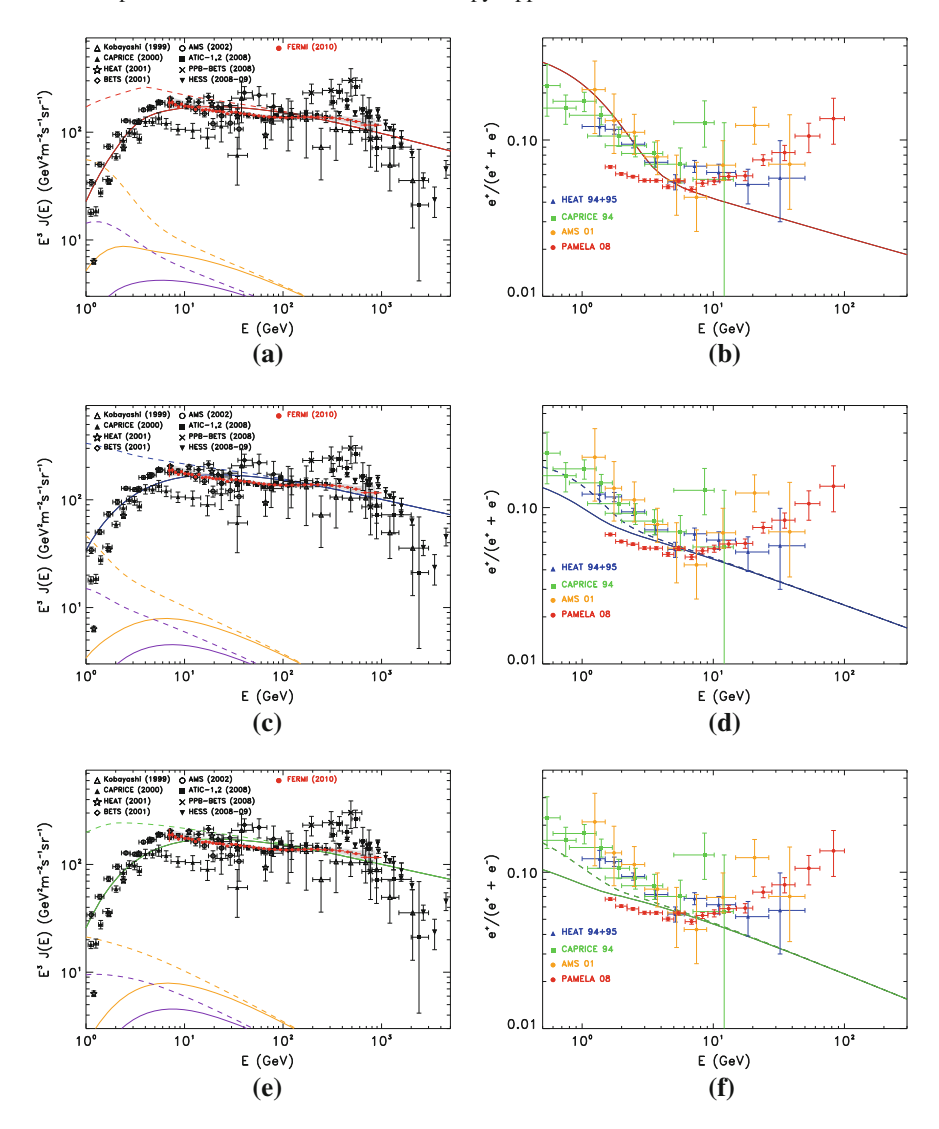


Fig. 5.23 The electron $(e^- + e^+)$ spectrum is shown for the KOL (panel **a**), KRA (panel **c**) and PD (panel **e**) diffusion setups as specified in Table 5.2. The electron source spectral indexes are 1.60/2.50 below/above 4 GeV for the KOL model (panel **a**) and 2.00/2.43 and 2.0/2.400 below/above 2 GeV for the KRA (panel **c**) and PD models (panel e) respectively. *Purple* and *orange lines* represent secondary electron and positron spectra respectively. The corresponding positron fraction $(e^+/(e^- + e^+))$ curve computed under the same conditions are shown in the panels (**b**), (**d**) and (**f**) respectively. *Solid lines* are modulated with a potential $\Phi = 550$ MV. *Dashed lines* are the corresponding LIS spectra. Plots published in [42]

are correct, an additional positron component, besides that produced by CR spallation, has to be invoked.

5.8.3 Double Component Models

These considerations led us to consider again double component models with an extra component added to a diffuse background.

This time we start with a very general model: we consider a new component whose injection spectrum is modelled as power-law + exponential cutoff, and whose spatial distribution is taken equal to the CR source distribution adopted for the diffuse model; the nature of this source (pulsars? Dark Matter? something else?) will be addressed later.

In order to tune the normalization of the two spectral components we proceed this way.

- We tune the standard component to reproduce both the $e^- + e^+$ spectrum measured by Fermi-LAT and the $e^+/(e^-+e^+)$ measured by PAMELA below 20 GeV, where the effect of the extra component is supposed to be negligible. Remarkably, this is possible only if we use propagation setups with low reacceleration, namely either the KRA or the PD, because the low-energy part of PAMELA positron ratio can't be reproduced in KOL setup. Since the KRA also provides the best combined fit of B/C and antiproton data, we will stick to this model from now on. The required source spectral slopes for the electron standard component is $\gamma_{e^-} = 2.00/2.65$ below/above 4 GeV for this propagation model. Such index is quite steep if compared to theoretical predictions regarding Fermi acceleration mechanism, but we remind the reader that we modeled the standard component in the approximation of a cylindrically symmetric source distribution, which may be less realistic for high energy electrons where the local distribution is relevant. Accounting for the spiral arm distribution of SNRs may result in a different requirement for the injection index. Indeed, being the Sun in the so-called "local spur" situated in a interarm region, the average distance from SNRs is larger than in the smooth case: as a consequence, a harder injection spectrum may be required to compensate for the larger energy losses and reproduce the observed spectrum. Clearly, in the absence of the extra e^{\pm} component, high energy CRE and positron fraction data would completely be missed.
- We tune the extra-component to reproduce Fermi-LAT and H.E.S.S. high energy CRE data. We find here that this is possible by taking $\gamma_{e^\pm}=1.5$ and $E_{\rm cut}=1.0-1.5$ TeV (see Fig. 3). This is similar to the parameters used in the interpretation of 2009 data but in that case a KOL diffusion was used (so low energy positron data were not reproduced in that case).

The results are shown in Figs. 5.24 and 5.25. It is reamarkable that such a simple phenomenological model accounts for nearly all leptonic measurements from the sub-GeV to the TeV region.

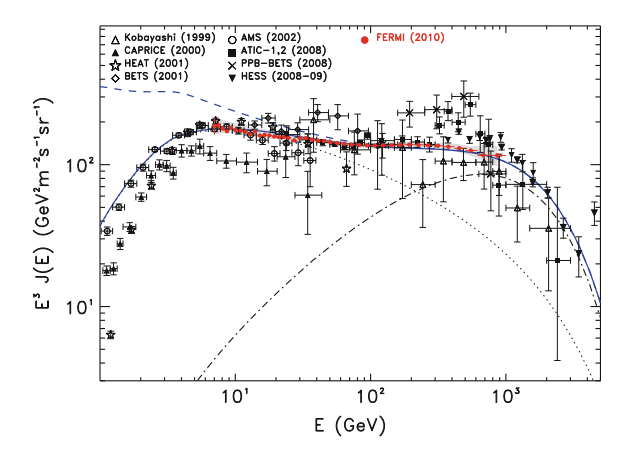
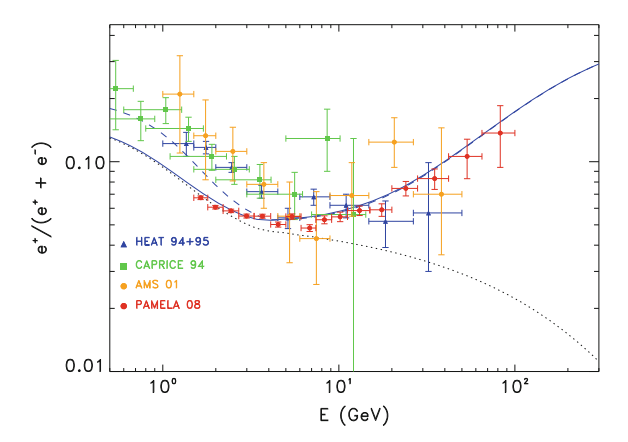


Fig. 5.24 The measured $e^- + e^+$ total spectrum is compared with the predictions of our two-component model. The *dotted line* represents the propagated standard component with injection slope $\gamma_{e^-} = 2.00/2.65$ above/below 4 GeV and $E_{\rm cut}^{e^-} = 3$ TeV, while the *dot-dashed line* is the e^\pm component with $\gamma_{e^\pm} = 1.5$ and $E_{\rm cut}^{e^\pm} = 1.4$ TeV. Both components are propagated with DRAGON adopting the KRA setup. The *blue solid/dashed lines* represent the modulated/LIS quantities. The modulated lines have been computed adopting the charge symmetric modulation potential $\Phi = 550\,\mathrm{MV}$. Published in [42]

Fig. 5.25 The measured positron ratio is compared with the predictions of our two-component model. Both components are propagated with DRAGON adopting the KRA setup. The *blue solid/dashed lines* represent the modulated/LIS quantities. The modulated lines have been computed adopting the charge symmetric modulation potential $\Phi = 550\,\mathrm{MV}$. Published in [42]



5.8.4 Contribution from Nearby Pulsars and SNRs

At this point we consider possible nearby astrophysical sources and—similarly to the analysis we performed for 2009 data—we see if they can account for the extra electrons and positrons; we also check if the models we propose are compatible with anisotropy upper limits published in [21].

We consider first the pulsars within 2 kpc from Earth, taken from the ATNF catalogue. We verified that more distant pulsars give a negligible contribution. We

100 5 The Leptonic Field

Fig. 5.26 The contribution from nearby pulsars (within 2 kpc) to the $e^+ + e^-$ specrum is computed analytically for the KRA diffusion setup and added to a standard component similar to that shown in Fig. 5.24 (but with an exponential cutoff at 3 TeV). The pulsar e^\pm conversion efficiency is \simeq 35 %. Published in [42]

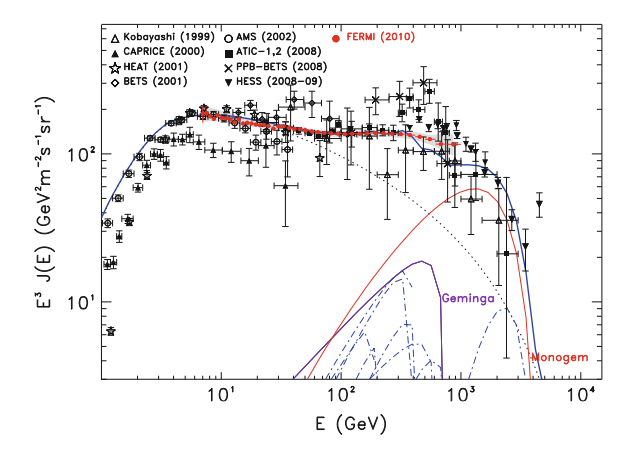
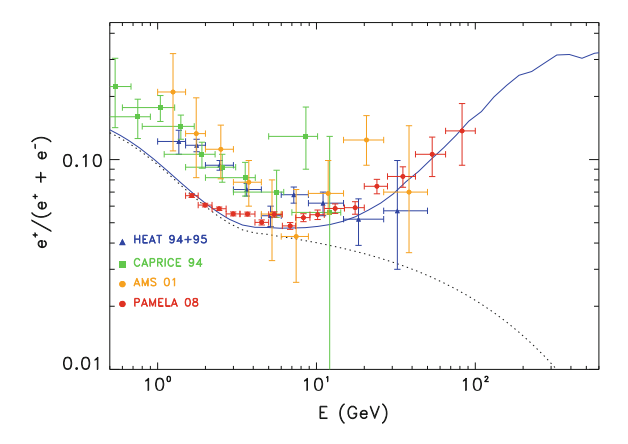


Fig. 5.27 The contribution from nearby pulsars (within 2 kpc) to the positron ratio is added to a standard component as in Fig. 5.26. Notice that since pulsars are assumed to emit both electrons and positrons, the rising positron-to-electron ratio measured by PAMELA is correctly reproduced within such a scenario. Published in [42]



also verified that γ -ray pulsars which have been detected by Fermi-LAT [30] and are not in the ATNF catalogue, which can also contribute to the observed $e^- + e^+$ spectrum do not affect significantly our results. The energy budget is computed as described in the previous paragraph.

As shown in Figs. 5.26 and 5.27, the pulsar scenario allows a very good fit of both high-energy Fermi-LAT and H.E.S.S. electron+positron as well as PAMELA positron fraction data, due to the presence of primary positrons. The plots in Figs. 5.26 and 5.27 have been computed assuming that $\tau_0 = 10^4 \, \mathrm{year}$, as commonly done in the literature. Furthermore we tuned the pulsar injection parameters to the values $\gamma_{e^\pm} = 1.4$, $E_{\mathrm{cut}} = 2 \, \mathrm{TeV}$, $T_{\mathrm{esc}} = 75 \, \mathrm{kyr}$ and $\eta_{e^\pm} = 35 \, \%$.

While it is certainly unrealistic to assume that all pulsars share the same values of those parameters, this is not critical for our results since the high energy tail of the spectrum is always dominated by a single object, namely the Monogem pulsar (PSR B0656+14) Furthemore, we already discussed that it is possible to reproduce

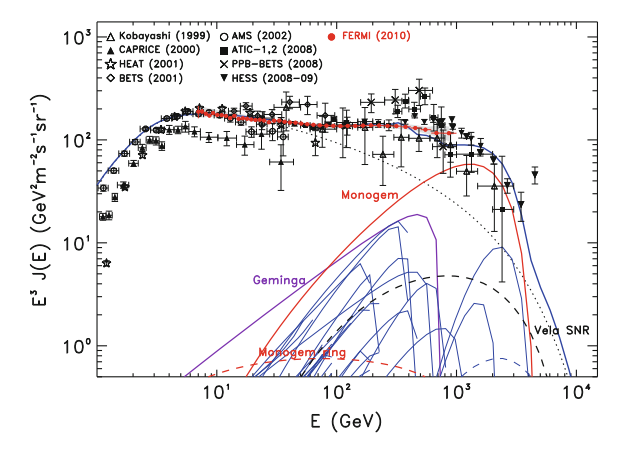


Fig. 5.28 The analytically computed CRE flux from both nearby (within 2 kpc) SNRs and pulsars is added to the same standard component used in Fig. 5.26. Again, all components are propagated using the KRA diffusion-reacceleration setup. The assumed energy release for each SNR is taken as 2×10^{47} erg . The pulsar efficiency is $\simeq30$ %. Solar modulation modulation potential is $\Phi=500$ MV. Published in [42]

CRE and positron data for several allowed combinations even randomly varying the pulsar parameters.

So far we have always treated the standard electron component as originated by a continuous distribution of sources (we only briefly considered the possibility of fluctuations of this continuous distribution and the role of the Gould's belt). This approximation, however, is not realistic above few hundred GeV for the reasons we explained above. Indeed, if we share the common, and well motivated, wisdom that CRE are accelerated by SNR, only few of those objects will contribute to the CRE observed spectrum above 100 GeV. This may produce observable features in the total CRE spectrum.

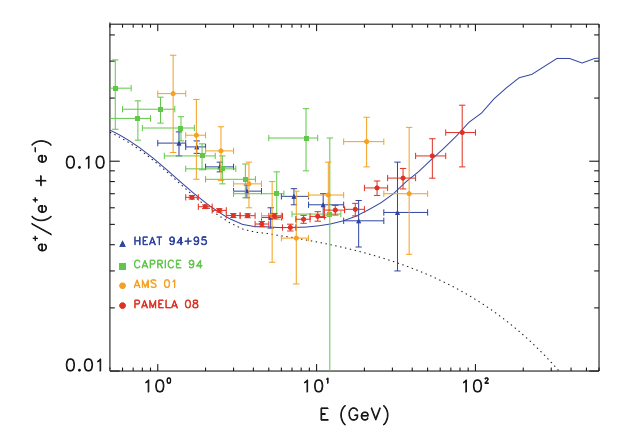
In order to study such effect, this time we treat CRE propagation from nearby SNRs (lying within the local arm) similarly to what we just did for pulsars. Since the SNR lifetime is typically smaller than the propagation time, we consider the emission from a single SNR as a single burst simultaneous to the SNR birth. Hence, we consider all observed SNRs within 2 kpc as taken from the Green catalogue [43] and treat them as point-like e^- sources with a power-law injection spectrum and an exponential cutoff (Fig. 5.29).

The reader may find an useful graphical representation of nearby SNRs and Pulsars plotted in a Age-Distance diagram in Fig. 5.30 taken from Delahaye et al. [33]. ¹⁰

¹⁰ In that paper the authors follow a similar approach and find that, for reasonable assumptions on the parameter of both local and distant sources, the current observations can be reproduced by a smooth distant contribution plus a collection of local pulsars and SNRs with no need for exotic contributions: such a finding is similar to our result. Moreover, they investigate the systematic uncertainties that turn out to be high: in particular, the spectral shape at high energy appears to be

102 The Leptonic Field

Fig. 5.29 The positron fraction is shown for the same model of Fig. 5.28 compared to experimental data. The assumed energy release for each SNR is taken as 2×10^{47} erg. The pulsar efficiency is ~30 %. Solar modulation modulation potential is $\Phi = 500 \,\text{MV}$. Published in [42]



In Figs. 5.28 and 5.29 we respectively represent the CRE spectrum and positron fraction obtained for a reasonable combination of pulsar and SNR parameters, namely:

- injection index for the SNRs: $\gamma_{a-}^{SNR} = 2.4$;
- cutoff energy for the SNRs: $E_{\rm cut}^{\rm SNR}=2~{\rm TeV};$ electron energy release per SN $E^{\rm SNR}=2\times10^{47}~{\rm erg};$
- injection index for the pulsars: $\gamma_{e^-}^{PSR} = 1.5$;
- cutoff energy for the pulsars: $E_{\rm cut}^{\rm PSR}=1.5~{\rm TeV};$ efficiency for the pulsars: $\eta_{e^\pm}^{\rm PSR}\simeq30~\%$ (which is slightly smaller than that needed without considering nearby SNR).

We see from Fig. 5.28 that, under those conditions, the dominant sources in the 100 GeV-1 TeV region remain Monogem and Geminga.

Clearly, other combinations of parameters are possible, and the relative contributions of the several sources may vary. However, the requirement to reproduce the PAMELA positron fraction imposes an important independent constraint which does not permit to lower significantly the Monogem dominant contribution with respect to that of SNRs: therefore the discrete contribution of nearby SNRs should not introduce pronounced features (bumpiness) in the CRE spectrum.

The pulsars and SNRs that were considered so far are represented, for illustrative purposes, in Fig. 5.31 in which the approximate locations of the Monogem and Geminga pulsars, together with Cygnus Loop and Vela SNRs, are shown superimposed to a map of the nearby interstellar medium showing the most important structures (Giant Molecular Clouds, OB complexes); the pattern of the Gould's belt is clearly seen in the map.

weakly correlated with the spectral indices of local sources, but more strongly with the hierarchy in their distance, age and power.

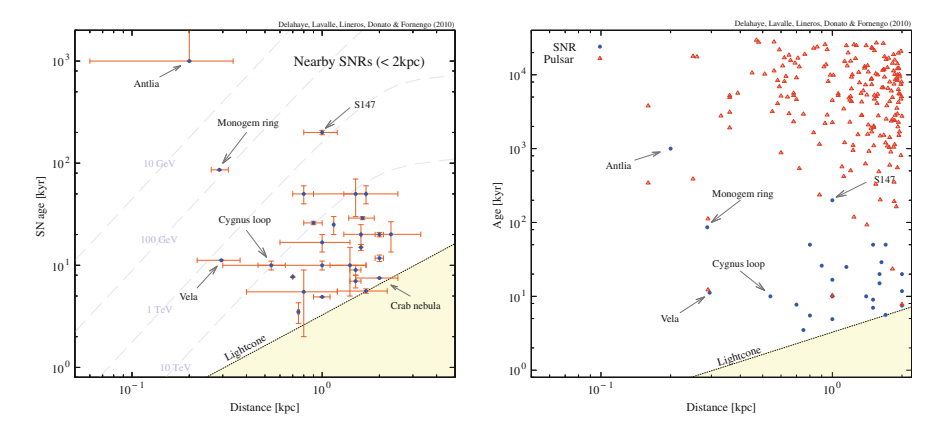


Fig. 5.30 *Left* Plot of the observed age versus distance to the Earth for a collection of local SNRs. *Right* the same plot for a complete sample of local SNRs and pulsars. The *dashed lines* correspond to limits beneath which a local source cannot contribute significantly to the signal (valid for MED propagation setup). Published in [33]

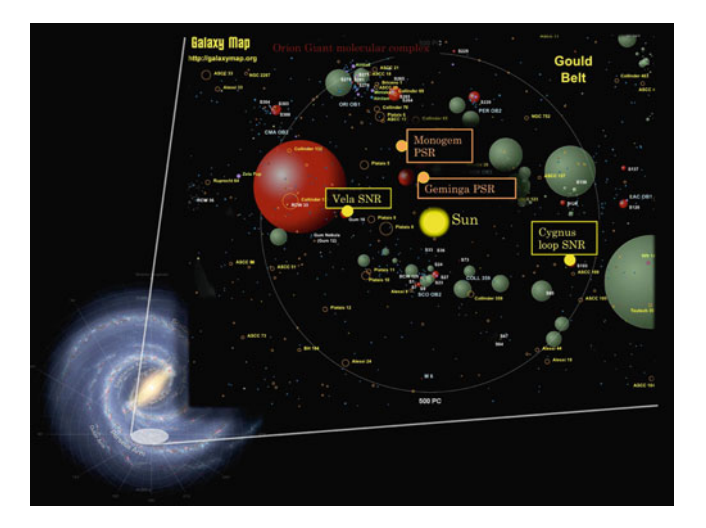


Fig. 5.31 A map of the nearby interstellar medium taken from http://galaxymap.org/detail_maps/gould.html is shown. The map features the Gould's belt region, i.e. the part of the Galaxy corresponding to the Local Arm. The most important sources that contribute to the CR electron flux are superimposed to the map

5.8.5 Compatibility with Upper Limits on Anisotropy

We will see now if this prediction is compatible with current upper limits published by Fermi collaboration.

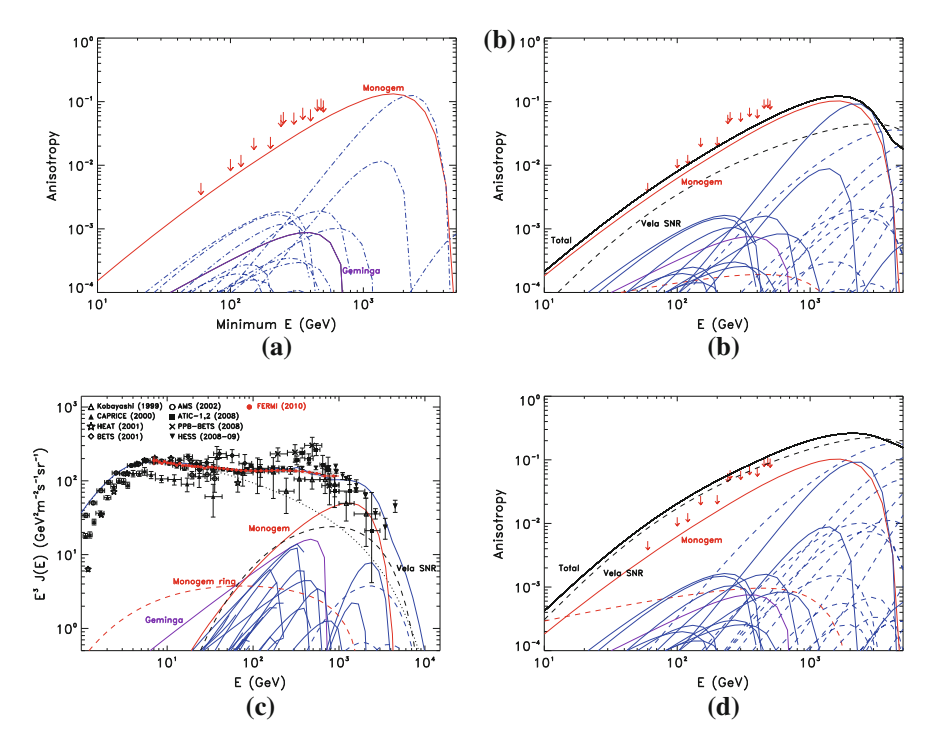


Fig. 5.32 Panel **a**: The integrated anisotropy, as a function of minimum energy, computed for the pulsar model plotted in Fig. 5.26 is compared to the 95 % C.L. Fermi-LAT upper limits [21]; Panel **b**: The same is done here for the pulsars+SNRs model plotted in Fig. 5.28. The *black solid line* represents the total anisotropy, originated mostly by Monogem and Vela SNR. Panel **c**: The CRE spectrum for a modified version of the pulsars+SNRs (hybrid) model in which the energy output of SNRs is increased to 1×10^{48} erg is represented. This model is still compatible with Fermi-LAT and HESS electron data. Panel **d**: The corresponding anisotropy is shown: a strong contribution from SNRs is not compatible with Fermi-LAT upper limits. Plots published in [42]

The analytical expressions which we used to compute the CRE anisotropy due to a single pulsar is:

Anisotropy =
$$\frac{3}{2c} \frac{r}{T - T_{\text{esc}}} \left(\frac{1 - (1 - E/E_{\text{max}}(t))^{1 - \delta}}{(1 - \delta)E/E_{\text{max}}(t)} \right)^{-1} \frac{N_e^{\text{PSR}}(E)}{N_e^{\text{tot}}(E)}$$
 (5.18)

where $N_e^{\rm PSR}$ and $N_e^{\rm tot}$ are the electron spectra from the pulsar and its sum to the large scale Galactic plus distant pulsar components; T and $T_{\rm esc}$ are the pulsar birth time and the time it takes for the electrons to be released in the ISM respectively; $E_{\rm max}(t)$ is the energy loss time due to synchrotron and IC losses.

The most important results we obtained are summarized in Fig. 5.32a, b.

First of all, it is important to notice that the model we presented above, where only the emission from nearby pulsars is added to the smooth Galactic standard component, is compatible with the upper limits reported by the Fermi-LAT Collaboration. The middle-aged pulsar Monogem gives the dominant contribution to the anisotropy, and the expected value of this observable is very close to the upper limit, so that a positive detection is expected in the near future towards Monogem.

Hence we now consider the model (repersented in Fig. 5.28) in which the main contribution to the high energy $e^- + e^+$ flux still comes from pulsars but the contribution of local SNRs is also considered (hybrid model). We see from Fig. 5.32b that also this possibility is not excluded by anisotropy measurements: in this plot, the reader may notice that the Monogem pulsar (red solid line) and the Vela SNR (black dashed line) contribute most to the total anisotropy (the black solid line), which is computed as the sum of each anisotropy weighted by the cosine of the angle of the corresponding source with respect to the direction of the maximum flux. However, also in this case the total expected anisotropy is very close to the measured upper limit, so that a future detection at level $\sim 1\%$ at ~ 1 TeV towards the portion of the sky where Vela and Monogem are located (with the peak situated almost in the middle between the two sources) is expected in the next years.

It should be noticed that Fermi-LAT anisotropy constraints already exclude some models which do reproduce the CRE and the positron fraction data. For illustrative purposes, in Fig. 5.32c, d we show the CRE spectrum and anisotropy computed for a model in which the electron energy emitted by SNRs is increased from 2×10^{47} erg to 1×10^{48} erg and pulsar e^{\pm} emission efficiency is consequently reduced from 35 to 30% so to reproduce the observed CRE spectrum. We see from Fig. 5.32d that the expected anisotropy exceeds the upper limits in that case, mostly because of the large contribution of Vela SNR, which is nearby (less than 300 pc) and very young ($\sim 10^4$ year). Although this result can hardly be translated into a sharp constraint on the e^{\pm} energy output from SNRs, due to the large number of free parameters we had to deal with, nevertheless we can safely conclude that a scenario in which SNRs provide the dominant contribution to CRE spectrum in the TeV region is incompatible with Fermi-LAT upper limits on the CRE anisotropy.

5.9 Fermi Preliminary Measurement of CR Positron Spectrum

Although Fermi-LAT is not equipped with a magnet and is therefore unable to distinguish between a positron and an electron track, there is a way to measure the positron flux with this instrument. The idea is to use the Earth magnetic field: since it bends electrons and positrons in different ways, there are certain patches of the sky will contain just one kind of particle but not the other. Using a numerical code that calculates the trajectory of leptons in the geomagnetic field it is possible to compute the regions where only e^+ or only e^+ are allowed: the leptonic tracks registered by the instrument when it passes through these regions can therefore be identified as

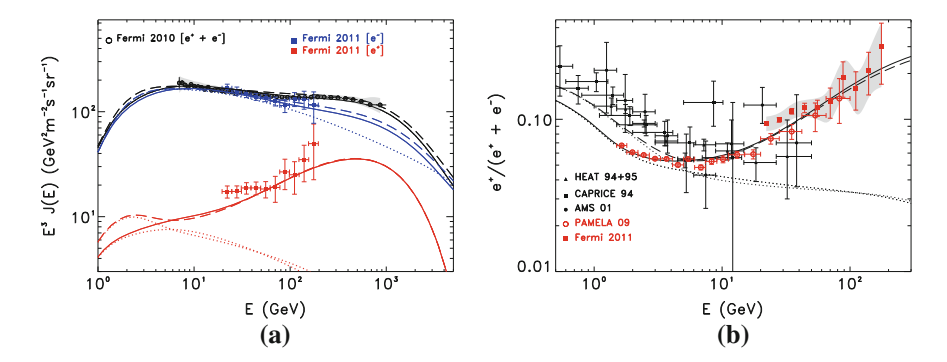


Fig. 5.33 The new data on positron spectrum and positron ratio released by Fermi-LAT collaboration are nicely matched by a simple double-component model in which the diffuse standard component is added to an extra primary component of electrons+positrons with a hard injection spectrum (slope = -1.5) and exponential cutoff at 1.4 TeV. *Solid lines* KRA diffusion setup. *Dashed lines* KOL diffusion setup

electrons or positrons. These regions get smaller as the particle energy increases, making the task more and more difficult.

Fermi-LAT collaboration released the measurement of the absolute positron and electron fluxes based on this method in a recent paper [44]; the measure is based on the events collected from June 2008 to April 2011.

The principal background is the CR hadronic component. In order to substract it, two different strategies were adopted:

- A Fit-based method. in this method a collection of real events is considered; the variable used to distinguish hadrons from leptons is the transverse shower size in the calorimeter, and the distribution of this variable is fitted with two Gaussians to separate the signal from the background.
- A MonteCarlo-based method. in this method a large set of CR MC-simulated proton is produced; the event selection is then applied to the simulation to estimate the surviving background.

The results can be seen in Fig. 5.33a, b. The fit-based method was chosen for every energy bin except the highest. It is remarkable that the positron ratio data points are in good agreement with PAMELA measure: it is an interesting independent confirmation of the rising behaviour of this ratio with energy that created much debate in the scientific community.

In these plots the data points are also compared to the models. In Fig. 5.33a the absolute electron and positron spectra are compared with our pre-existing double component model computed with DRAGON adopting the KOL (dashed lines) and KRA (solid lines) diffusion setups discussed in the above. Noticeably, the absolute positron data appear to be perfectly compatible with the extra-component scenario, and are in strong tension with the scenario in which only the secondary contribution is present (red dotted lines, referring to KOL and KRA setups). In Fig. 5.33b we plotted the positron ratio measured by Fermi-LAT compared to the same models. As

we already pointed out in the previous paragraphs, in the high-energy end the two models don't show any big difference and are both compatible with PAMELA (and now Fermi) data while at low energy the KRA model gives a better fit of PAMELA dataset.

References

- 1. T.A. Porter, A.W. Strong, A new estimate of the Galactic interstellar radiation field between 0.1 μm and 1000 μm, in *International Cosmic Ray Conference*, vol. 4 (2005), p. 77
- S.V. Bulanov, V.A. Dogel, The influence of the energy dependence of the diffusion coefficient on the spectrum of the electron component of cosmic rays and the radio background radiation of the galaxy. Astrophys. Space Sci. 29, 305–318 (1974)
- O. Adriani et al. [PAMELA collaboration], An anomalous positron abundance in cosmic rays with energies 1.5–100 GeV. Nature 458, 607–609 (2009)
- 4. P.D. Serpico, Possible causes of a rise with energy of the cosmic ray positron fraction. Phys. Rev. D **79**(2), 021302 (2009)
- J. Chang et al. [ATIC collaboration], An excess of cosmic ray electrons at energies of 300–800 GeV. Nature 456, 362–365 (2008)
- D. Hooper, P. Blasi, P.D. Serpico, Pulsars as the sources of high energy cosmic ray positrons.
 J. Cosmol. Astropart. Phys. 1, 25 (2009)
- A.M. Atoyan, F.A. Aharonian, H.J. Völk, Electrons and positrons in the galactic cosmic rays. Phys. Rev. D 52, 3265–3275 (1995)
- C.S. Shen, Pulsars and very high-energy cosmic-ray electrons. Astrophys. J. Lett. 162, L181 (1970)
- 9. A.K. Harding, R. Ramaty, The pulsar contribution to galactic cosmic ray positrons, in *International Cosmic Ray Conference*, vol. 2 (1987), p. 92
- S. Profumo, Dissecting cosmic-ray electron-positron data with Occam's Razor: the role of known pulsars. Central Eur. J. Phy. 10(1), 1–31 (2012)
- R.N. Manchester, G.B. Hobbs, A. Teoh, M. Hobbs, The Australia telescope national facility pulsar catalogue. Astron. J. 129, 1993–2006 (2005)
- 12. R.N. Manchester, G.B. Hobbs, A. Teoh, M. Hobbs, The Australia telescope national facility pulsar catalogue. http://www.atnf.csiro.au/people/pulsar/psrcat/
- M. Markevitch, A.H. Gonzalez, D. Clowe, A. Vikhlinin, W. Forman, C. Jones, S. Murray, W. Tucker, Direct constraints on the dark matter self-interaction cross section from the merging galaxy cluster 1E 0657-56. Astrophys. J. 606, 819–824 (2004)
- E. Komatsu, J. Dunkley, M.R. Nolta, C.L. Bennett, B. Gold, G. Hinshaw, N. Jarosik, D. Larson, M. Limon, L. Page, D.N. Spergel, M. Halpern, R.S. Hill, A. Kogut, S.S. Meyer, G.S. Tucker, J.L. Weiland, E. Wollack, E.L. Wright, Five-year Wilkinson microwave anisotropy probe observations: cosmological interpretation. Astrophys. J. Suppl. 180, 330– 376 (2009)
- V. Springel, C.S. Frenk, S.D.M. White, The large-scale structure of the Universe. Nature 440, 1137–1144 (2006)
- M. Cirelli, M. Kadastik, M. Raidal, A. Strumia, Model-independent implications of the positron, electron and antiproton cosmic ray spectra on properties of dark matter. Nucl. Phys. B 813, 1–21 (2009)
- M. Cirelli, R. Franceschini, A. Strumia, Minimal dark matter predictions for galactic positrons, anti-protons, photons. Nucl. Phys. B 800, 204–220 (2008)
- W.B. Atwood et al. [Fermi Collaboration], The large area telescope on the fermi gamma-ray space telescope mission. Astrophys. J. 697, 1071–1102 (2009)

- 19. A.A. Abdo et al. [Fermi Collaboration], Measurement of the cosmic ray $e^+ + e^-$ spectrum from 20GeV to 1TeV with the fermi large area telescope. Phys. Rev. Lett. **102**(18), 181101 (2009)
- M. Ackermann et al. [Fermi Collaboration], Fermi LAT observations of cosmic-ray electrons from 7 GeV to 1 TeV. Phys. Rev. D 82(9), 092004 (2010)
- M. Ackermann et al. [Fermi collaboration], Searches for cosmic-ray electron anisotropies with the fermi large area telescope. Phys. Rev. D 82(9), 092003 (2010)
- 22. D. Grasso, S. Profumo, A.W. Strong, L. Baldini, R. Bellazzini, E.D. Bloom, J. Bregeon, G. Di Bernardo, D. Gaggero, N. Giglietto, T. Kamae, L. Latronico, F. Longo, M.N. Mazziotta, A.A. Moiseev, A. Morselli, J.F. Ormes, M. Pesce-Rollins, M. Pohl, M. Razzano, C. Sgrò, G. Spandre, T.E. Stephens, On possible interpretations of the high energy electron-positron spectrum measured by the fermi large area telescope. Astropart. Phys. 32, 140–151 (2009)
- 23. C. Evoli, D. Gaggero, D. Grasso, L. Maccione, Cosmic ray nuclei, antiprotons and gamma rays in the galaxy: a new diffusion model. J. Cosmol. Astropart. Phys. **10**, 18 (2008)
- G. Di Bernardo, C. Evoli, D. Gaggero, D. Grasso, L. Maccione, Unified interpretation of cosmic ray nuclei and antiproton recent measurements. Astropart. Phys. 34, 274–283 (2010)
- M. Pohl, C. Perrot, I. Grenier, S. Digel, The imprint of Gould's Belt on the local cosmic-ray electron spectrum. Astron. Astrophys. 409, 581–588 (2003)
- T. Delahaye, R. Lineros, F. Donato, N. Fornengo, J. Lavalle, P. Salati, R. Taillet, Galactic secondary positron flux at the Earth. Astron. Astrophys. 501, 821–833 (2009)
- V.L. Ginzburg, V.S. Ptuskin, On the origin of cosmic rays: some problems in high-energy astrophysics. Rev. Mod. Phys. 48, 161–189 (1976)
- D.J. Thompson, Z. Arzoumanian, D.L. Bertsch, K.T.S. Brazier, J. Chiang, N. D'Amico, B.L. Dingus, J.A. Esposito, J.M. Fierro, C.E. Fichtel, R.C. Hartman, S.D. Hunter, S. Johnston, G. Kanbach, V.M. Kaspi, D.A. Kniffen, Y.C. Lin, A.G. Lyne, R.N. Manchester, J.R. Mattox, H.A. Mayer-Hasselwander, P.F. Michelson, C. von Montigny, H.I. Nel, D.J. Nice, P.L. Nolan, P.V. Ramanamurthy, S.L. Shemar, E.J. Schneid, P. Sreekumar, J.H. Taylor, EGRET highenergy gamma-ray pulsar studies. 1: Young spin-powered pulsars. Astrophys. J. 436, 229–238 (1994)
- F.A. Aharonian, A.M. Atoyan, T. Kifune, Inverse Compton gamma radiation of faint synchrotron X-ray nebulae around pulsars. Mon. Not. R. Astron. Soc. 291, 162–176 (1997)
- 30. A.A. Abdo et al. [Fermi Collaboration], The first fermi large area telescope catalog of gammaray pulsars. Astrophys. J. Suppl. **187**, 460–494 (2010)
- 31. F.A. Aharonian, Very high energy cosmic gamma radiation: a crucial window on the extreme Universe (World Scientific Publishing, River Edges, 2004)
- 32. I. Büsching, C. Venter, O.C. de Jager, Contributions from nearby pulsars to the local cosmic ray electron spectrum. Adv. Space Res. 42, 497–503 (2008)
- T. Delahaye, J. Lavalle, R. Lineros, F. Donato, N. Fornengo, Galactic electrons and positrons at the Earth: new estimate of the primary and secondary fluxes. Astron. Astrophys. 524, A51 (2010)
- 34. J. Diemand, M. Kuhlen, P. Madau, M. Zemp, B. Moore, D. Potter, J. Stadel, Clumps and streams in the local dark matter distribution. Nature **454**, 735–738 (2008)
- D.P. Finkbeiner, N. Weiner, Exciting dark matter and the INTEGRAL/SPI 511keV signal. Phys. Rev. D 76(8), 083519 (2007)
- M. Ahlers, P. Mertsch, S. Sarkar, Cosmic ray acceleration in supernova remnants and the FERMI/PAMELA data. Phys. Rev. D 80(12), 123017 (2009)
- 37. P. Blasi, Origin of the positron excess in cosmic rays. Phys. Rev. Lett. 103(5), 051104 (2009)
- N.J. Shaviv, E. Nakar, T. Piran, Inhomogeneity in cosmic ray sources as the origin of the electron spectrum and the PAMELA anomaly. Phys. Rev. Lett. 103(11), 111302 (2009)
- P. Blasi, P.D. Serpico, High-energy antiprotons from old supernova remnants. Phys. Rev. Lett. 103(8), 081103 (2009)
- P. Mertsch, S. Sarkar, Testing astrophysical models for the PAMELA positron excess with cosmic ray nuclei. Phys. Rev. Lett. 103(8), 081104 (2009)

References 109

41. J. Stockton, Average inhomogeneities in Milky Way SNII and The PAMELA anomaly. ArXiv e-prints (2011)

- 42. G. Di Bernardo, C. Evoli, D. Gaggero, D. Grasso, L. Maccione, M.N. Mazziotta, Implications of the cosmic ray electron spectrum and anisotropy measured with Fermi-LAT. Astropart. Phys. **34**, 528–538 (2011)
- D.A. Green, A revised Galactic supernova remnant catalogue. Bull. Astron. Soc. India 37, 45–61 (2009)
- 44. M. Ackermann et al. [Fermi Collaboration], Measurement of separate cosmic-ray electron and positron spectra with the fermi large area telescope. ArXiv e-prints (2011)

Chapter 6 Diffuse Gamma Ray Emission from the Galaxy

6.1 Outline

In this chapter

- I will briefly overview the history of the observation of the diffuse gamma ray emission from the Galaxy and the open problems related to its modellization.
- I will emphasize the role of Fermi-Lat in the understanding of Gamma-ray sky.
- I will look for a comprehensive model allowing to fit consistently both all CR observables and the gamma-ray spectrum at mid-latitude; most importantly, it provides a natural solution to the gradient problem accounting for the spatial variation of the diffusion coefficient.

6.2 Introduction

6.2.1 How Diffuse γ Rays are Produced

It has been known for a long time that the Galaxy should be bright in γ -rays due to the following processes [1, 2]:

• π^0 decay.

The *hadronic* part of the CRs interacts with the interstellar gas and produces pions (π^0, π^{\pm}) : neutral pions decay into $\gamma \gamma$.

This process traces the spatial distribution of CR protons (and heavier nuclei) together with the interstellar gas.

In fact, the π^0 emissivity¹ is a function of both quantities:

¹ The emissivity is the number of particles (neutral pions in this case) emitted per unit of volume, time, energy.

$$Q_{\pi^0}(E_{\pi^0}) = c \, n_{\text{ISM}} \int_{E_{\text{soclia, RC}}(E_{\pi^0})}^{\infty} dE_{\text{RC}} \, \frac{dn_{\text{RC}}}{dE}(E_{\text{RC}}) \, \frac{d\sigma_{pp}}{dE_{\pi^0}}$$
(6.1)

where $\frac{\mathrm{d}\sigma_{pp}}{\mathrm{d}E_{\pi^0}}$ is the differential cross section of π^0 production from p-p collisions. If a power-law with index α is assumed for the spectral dependence of cosmic rays, and the cross section is approximated with the following scaling relation:

$$\frac{d\sigma_{pp}}{dE_{\pi^0}}(E_{CR}, E_{\pi^0}) = \frac{\sigma_0}{E_{\pi^0}} \cdot f_{\pi^0}(x)$$
(6.2)

then the π^0 emissivity is given by (see e.g. [3, 4]):

$$Q_{\pi^0}(E_{\pi^0}) = \frac{2}{\alpha} c \, n_{\text{ISM}} \, \sigma_0 \, \frac{dn_{\text{RC}}}{dE}(E_{\pi^0}) \, Y_{\gamma}(\alpha)$$
 (6.3)

and the corresponding photon emissivity is given by:

$$Q_{\gamma}(E_{\gamma}) = \frac{2}{\alpha} c n_{\text{ISM}} \sigma_0 \frac{dn_{\text{RC}}}{dE}(E_{\gamma}) Y_{\gamma}(\alpha)$$
 (6.4)

where the term *Y* (the *Yield*) is a function of the spectral index of the CRs. So the photons emitted through this mechanism have—above some GeV—a power-law spectrum with the same index as the CR protons (and nuclei).

• Inverse Compton.

It is the same process described in Chap. 5: the scattering between ultra-relativistic CR electrons and ambient photons (lying in the radio, microwave, IR, optical and UV domain) results in a loss of energy for the cosmic ray and a gain for the photon which is then converted into a X or γ ray depending on the energy.

This process traces the spatial distribution of CR electrons together with the ISRF.

• Bremsstrahlung.

It is well known that Bremsstrahlung is the electromagnetic radiation produced by the deceleration of a charged particle when deflected by another charged particle. In the Galaxy CR electrons interact with the IS gas and emit Bremsstrahlung γ rays. So, this kind of emission traces the distribution of the leptonic part of CR together with the gas distribution.

It is very important to study the γ diffuse emission because, differently from CR spectra measured at Solar System positrion, they trace the overall distribution of CR protons and electrons in the Galaxy. On the other hand, the various effects that contribute to that emission, the difficulty to disentangle the real diffuse from unresolved point sources and the great number of free parameters involved in the models make this kind of study very difficult.

6.2 Introduction 113

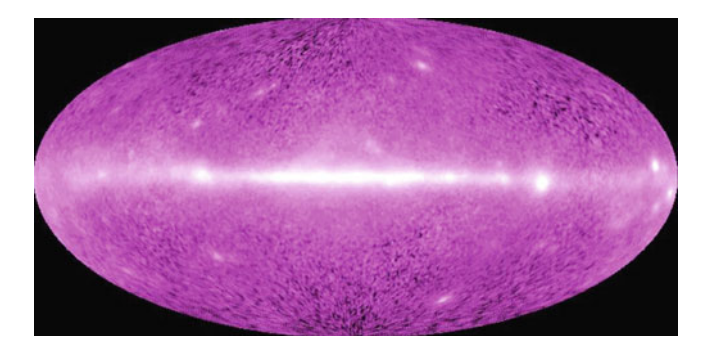


Fig. 6.1 EGRET view of gamma-ray sky. Taken from http://apod.nasa.gov/apod/ap020112.html. Credit: EGRET Team, Compton Observatory, NASA

6.2.2 Brief Overview of Pre-Fermi γ -Ray Observations

The history of the observation of this kind of emission starts in 1967 when the OSO-3 satellite obtained the first identification of high-energy cosmic gamma rays coming from both galactic and extra-galactic sources. In [5] the very first evidence of a Galactic gamma emission concentrated in a belt of directions around the Galactic equator can be found.

In the following years, the field of gamma-ray astronomy took great leaps forward with the SAS-2 (1972) and the COS-B (1975–1982) satellites that created the first low-resolution gamma ray maps of the sky.

However, the most important results in pre-Fermi era were obtained in the early 1990s by the Energetic Gamma Ray Experiment Telescope (EGRET²), one of four instruments mounted on NASAs Compton Gamma Ray Observatory satellite. EGRET was designed to collect gamma-ray from $\simeq 20$ MeV to $\simeq 30$ GeV with a $\simeq 20$ % energy resolution over the central part of the energy range and an angular resolution 5–30 arcmin depending on the nature of the source intensity, location, and energy spectrum).

EGRET observed [6] 271 sources from April 1991 to October 1995: five pulsars, several active galactic nuclei, and many (171) unidentified sources. More importantly for our purpose, EGRET produced the most accurate maps of the diffuse γ emission from the Galaxy at the time [7]; a γ -ray view of the whole sky can be seen in Fig. 6.1.

6.2.3 Open Problems After EGRET Era

The diffuse emission measured by EGRET was compared to theoretical expectations (using mainly GalProp) and some interesting discrepancies were found:

² see here: http://heasarc.gsfc.nasa.gov/docs/cgro/egret/egret_tech.html for a detailed technical description.

- The **GeV-excess**: as noted in [7] above about 1 GeV the integral intensity predicted by the model is about 60 % less than the observed intensity; this led many authors to modified CR propagation models [8] in which an enhanced CR proton flux through the Galaxy with respect to the locally observed one is considered.
- The **Gradient problem**: the predicted profile along the Galactic plane of the γ diffuse emission can be calculated with numerical codes using the CR and gas distribution as ingredients; this profile is very sensitive to the radial distribution of the source term through the Galaxy, which is inferred from SNR and pulsar catalogues; the problem is that *the computed profile appears much steeper* than the observed one [9].

This is a serious problem and several solutions were proposed; in particular we recall:

- A modified source term in which a flat CR source distribution is assumed ad hoc;
- A modified dependence of the X_{CO} upon R (galacto-centric radius). The X_{CO} is the conversion factor between the CO emissivity and the H_2 density. As we mentioned in Sect. 2.3.2 the molecular Hydrogen is not directly observable and therefore the CO molecule is used as a tracer: the emissivity of the CO line is observed and the X_{CO} factor permits to extrapolate the H_2 density. The X_{CO} is expected to vary through the Galaxy, e.g. from the measurement of a Galactic metallicity gradient combined with the strong inverse dependence of X_{CO} on metallicity in external galaxies [10, 11] but both the value at Sun position and the radial gradient are largely uncertain. Strong et al. [9] found that a X_{CO} that increases by roughly one order of magnitude from R=2 to 10 kpc permits to reproduce the γ -ray gradient: in fact, with a growing conversion factor the outer galaxy (which is seen in γ -rays at large Galactic longitude) has more gas and π^0 production is enhanced: therefore more γ are produced compensating for the rapidly falling source term and the gradient is flattened in accord with the observations.

6.3 Fermi-LAT View of Gamma-Ray Sky

Fermi-LAT was expected to give a major contribution to the field because of its incredible performance [12]:

- Energy range: 20 MeV-300 GeV (including the previously unexplored window 30-300 GeV).
- Effective area: $9,500 \, \text{cm}^2$ ($\sim 6 \, \text{times EGRET}$).
- Energy resolution: 8–9 % in the 1–10 GeV range (on-axis); decreasing to 18 % at 300 GeV.
- Angular resolution for a single photon: $\leq 0.15^{\circ}$ for $E \geq 10 \,\text{GeV}$.
- Field of view: 2.4 sr.

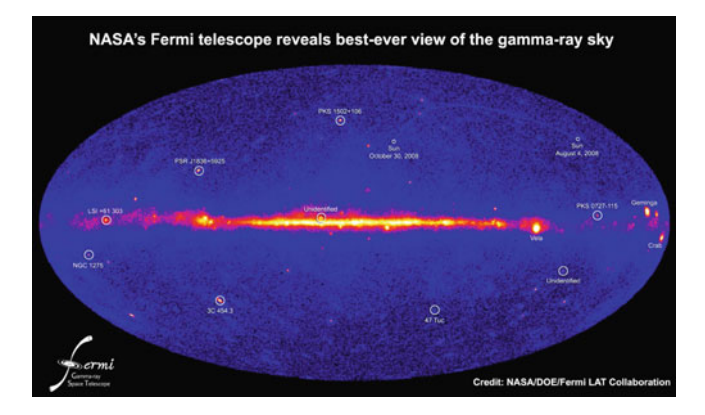


Fig. 6.2 Fermi-LAT view of gamma-ray sky after 3 months in orbit. Taken from http://apod.nasa.gov/apod/ap090321.html.Credit: NASA, DOE, Fermi LAT Collaboration

These technical specifications permitted to obtain, after only 3 months of operation, the most accurate ever γ -ray map of the whole sky (Fig. 6.2).

The fine resolution and high sensitivity allowed to expand the number of known γ emitters: the First Fermi Catalog released in 2010 [13] included 1,451 sources detected and characterized in the 100 MeV to 100 GeV range.

From the point of view of the *diffuse emission*, Fermi-LAT provided interesting responses to the open problems of EGRET era:

- The GeV excess was not confirmed: the γ -ray spectrum in the range 100 MeV to 10 GeV at intermediate Galactic latitudes (10° $\leq |b| \leq 20$ °) is reported in [14] to be "well reproduced by a diffuse Galactic gamma-ray emission model that is consistent with local CR spectra and inconsistent with the EGRET GeV excess"
- The **Gradient problem** was confirmed.

In a very recent paper [15] the Fermi Collaboration investigated the γ -ray diffuse emission measured by Fermi-LAT with a *template*-like approach.

The principle is well represented in Fig. 6.3: the γ -ray diffuse map (without point sources) provided by Fermi-LAT presents a very good spatial correlation with the H_2 and HI maps. So the idea is to model the diffuse emission as a linear combination of various templates.

The first thing to do is decompose the molecular and atomic gas maps into galactocentric *rings*. This process is described in detail in [16].

The starting points are the spectral profiles of the CO [17] and HI emission lines for each line of sight (characterized by Galactic longitude l and latitude b); since the broadening of these lines is due to Doppler effect, each λ corresponds to a relative velocity v, so these profiles are converted into (l, b, v) data cubes.

At this point by means of the rotational curve of the Galaxy (that—following IAU recommendations—is assumed to be flat with $R_{\rm Sun}=8.5\,{\rm kpc}$ and $v=220\,{\rm km/s}$ at Sun position) it is possible to convert each relative velocity into a distance.

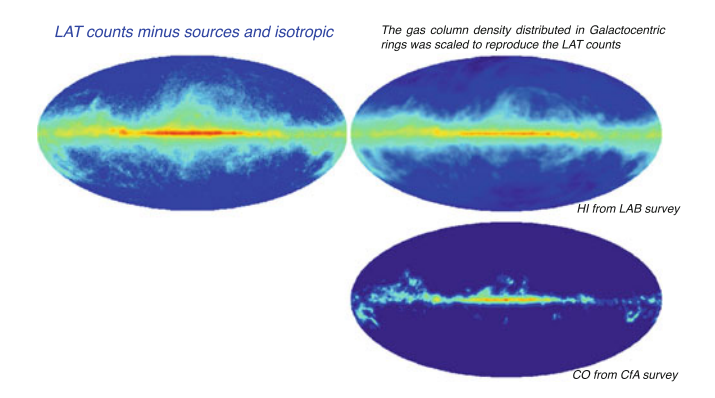


Fig. 6.3 The diffuse gamma counts map of the Galaxy is compared with CO and HI maps. Taken from J.M. Casandjan talk at Fermi Symposium 2011, http://fermi.gsfc.nasa.gov/science/symposium/2011/program/session2/Casandjian.pdf

In this way it is possible to have a map of the CO and HI emission corresponding to a particular Galacto-centric bin, i.e. a interval $R_1 < R < R_2$ where R is the Galacto-centric radius.

With such a model at hand, the template method consists in writing the γ -ray map in the following way:

$$n_{\gamma} = \sum_{\text{rings}} q_{\text{HI}} N_{\text{HI}} + \sum_{\text{rings}} q_{\text{CO}} W_{\text{CO}} + q_{\text{IC}} I_{\text{IC}} + \text{Isotropic}$$
 (6.5)

where $N_{\rm HI}$ and $W_{\rm CO}$ are the HI and CO maps corresponding to each ring, i.e. the maps containing only the emission coming from each annular region of the Galaxy.

In this way it is possible to derive—in a *model independent way*!—the HI and CO emissivities (corresponding to the set of coefficients $q_{\rm HI}$ and $q_{\rm CO}$) as functions of the Galactocentric distance R. The HI anc CO emissivities are proportional to the CR density and the CO emissivity also includes the $X_{\rm CO}$ factor.

We point out that this method can be applied because the HI and CO distributions are different and the high angular resolution of the LAT permits to discriminate between the different patterns of the two emissions.

In [16] this procedure is applied, respectively, to a region in the Second Galactic Quadrant corresponding to $100^{\circ} \le l \le 145^{\circ}; -15^{\circ} \le b \le 30^{\circ}$ and in [15] to the region $210^{\circ} \le l \le 250^{\circ}; -15^{\circ} \le b \le 20^{\circ}$. These regions allow a good kinematic separation between several regions along the line of sight: the nearby Gould Belt, the local arm, the Perseus and Outer arms.

The results are shown in Fig. 6.4. As the reader can see, the observed HI emissivity gradient appears much flatter than the predicted one (using GalProp) and a modified behaviour the $X_{\rm CO}$ can't be invoked to fix the problem since this method decouples the emission from molecular and atomic Hydrogen (this is possible

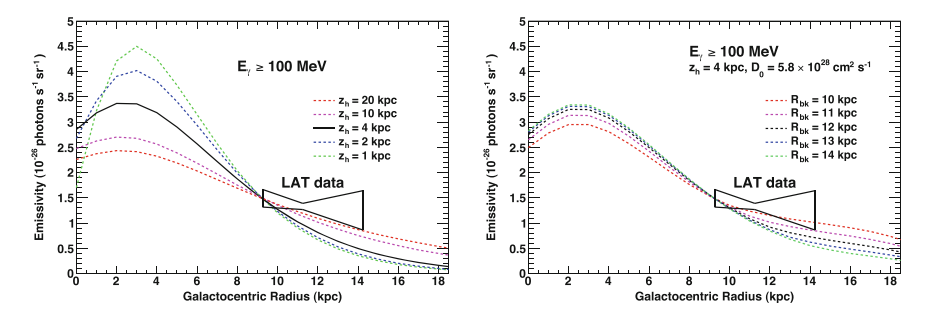


Fig. 6.4 The gamma ray emissivity gradient predicted by the models is steeper than the observed one (the band centered at Sun's position). In order to solve the problems, two solutions are proposed in [15]. (1) Adopt a thicker diffusion halo (Panel **a**): a value $z_h > 10 \,\mathrm{kpc}$ is required. (2) Adopt a source term that becomes flat for $R > R_{\mathrm{bk}}$ (Panel **b**): a value of $R_{\mathrm{bk}} < 10 \,\mathrm{kpc}$ is required

because of the different spatial distribution of the two component and to the high resolution of the LAT: it would not have been possible with EGRET data). The authors propose:

- A very large halo height (see the right panel of Fig. 6.4)
- A modified source term that becomes nearly flat at high R

as possible solutions to the problem.

6.4 Spatial-Dependent Diffusion Coefficient as a Solution to the Gradient Problem

6.4.1 The Idea

Nearly all models presented in the Literature adopt a spatially uniform diffusion coefficient throughout all the Galaxy.

Considering all that we discussed on the complexity of the insterstellar environment in Chap. 2 it is reasonable to expect instead a significant spatial dependence of this parameter: the point is if an effective model in which an average value is used may alter the prediction on some observables.

Since γ -rays—instead of CR spectra observed at Sun position—trace the *spatial distribution* of CRs through the Galaxy, it is natural to expect that a particular spatial distribution of the diffusion coefficient may reflect on different γ profiles.

From a physical point of view, it is straightforward to expect that regions where turbulence is higher correspond to a higher value of the *perpendicular* diffusion coefficient. This is supported by the following intuitive picture: in absence of any turbulence, CRs are expected to undergo spiral motion around the regular field lines (so approximately in the Φ direction, in cylindrical coordinates); if the turbulence

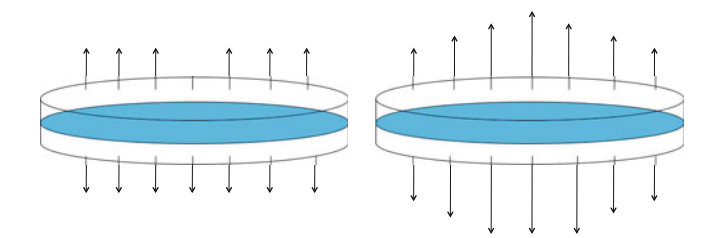


Fig. 6.5 In the regions where star formation (and hence turbulence) is higher a higher diffusion coefficient in the perpendicular direction with respect to the regular magnetic field is expected, and hence CR escape along z is faster

level increases, CRs are expected to deviate more and more from these regular trajectories and the random walk in the perpendicular direction becomes more and more effective. Since the perpendicular diffusion coefficient is the only one that matters in our framework for symmetry reasons (as pointed out at the end of Chap. 2), a higher turbulence reflects in a higher diffusion coefficient.

The consequence of this is sketched in Fig. 6.5: considering the radial dependence, the regions in which more star formation takes place (concentrated around $R \simeq 4-5\,\mathrm{kpc}$) are expected to exhibit stronger turbulence, and therefore a higher perpendicular diffusion coefficient. For this reason the CR escape along z is *favoured* in those parts of the Galaxy, and the propagated CR flux must *decrease*, smoothing in a natural way the CR gradient with *no need of any ad hoc assumption* on the source term and/or the halo height (Fig. 6.6).

6.4.2 The Method

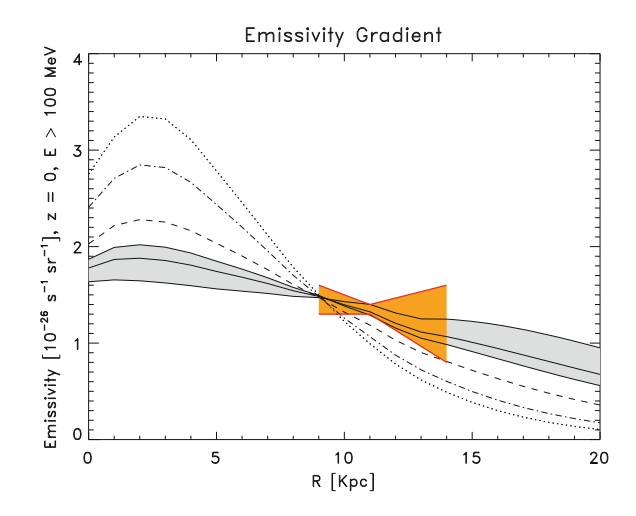
This idea was first applied by our group to interpret EGRET data and it was shown in Evoli et al. [18] that the γ ray profile observed by that experiment was nicely reproduced assuming a diffusion coefficient that varies with Galacto-centic coordinate R.

It is interesting to verify if this idea can be successfully applied to Fermi-LAT data too. I proceed in the following way, following an approach that recalls our 2008 paper [18]:

- The starting point is one of the model outlined in Sect. 5.8.2 compatible with CR spectra observed at Earth.
- Then I check if the introduction of a spatially varying diffusion coefficient allows to solve the gradient problem and hence provides a good fit of the γ -ray profile along the Galactic plane *continuing to reproduce the secondary-to-primary ratios*.

In order to calculate the γ -ray maps from which I extract the profiles I use GammaSky, a numerical package developed by us that is designed to interface with

Fig. 6.6 Here the effect of the parameter τ defined by Eq. 6.6 is explored. Dotted line no radial dependence of diffusion coefficient ($\tau=0$). Dot-dashed line $\tau=0.2$. Dashed line $\tau=0.5$. Solid lines $\tau=0.7-0.8-1.0$. The values corresponding to the solid lines within the grey band match the observed gradient



DRAGON and compute the π^0 , IC and Bremsstrahlung contributions to the γ -ray fluxes.

GammaSky works in this way:

- It takes the propagated CR distribution from DRAGON in the form of a FITS file for each particle.
- For each direction in the sky (l, b) the code scans the line of sight and in each interval $[s, s + \Delta s]$:
 - It calculates the corresponding position (R, z) in Galacto-centric coordinates.
 - It reads the CR density at that position computed by DRAGON.
 - It reads the gas density at that position.
 - It reads the ISRF.
 - It computes the π^0 IC and Bremsstrahlung contribution to the γ -ray flux.

In the following I adopt the following maps.

For the *gas*, I use the maps corresponding to each Galacto-centric *ring* adopted in GalProp public version v50p.

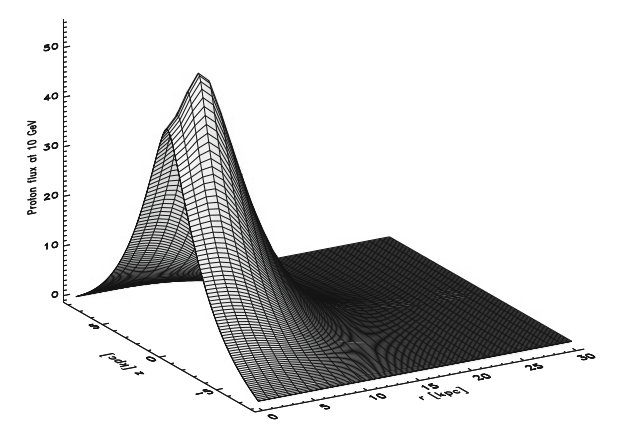
For the *ISRF* I adopt the distribution and spectrum implemented in Gal Prop [19].

6.4.3 Results

I start the analysis in a Plain Diffusion setup (See Sect. 5.8.2) with no convection and no reacceleration, in order to highlight better the effects of a spatially varying diffusion coefficient.

The CR propagation model is basically the same described in Sect. 5.8.2; the astrophysical parameters (in particular the source term, gas distribution and X_{CO}) are

Fig. 6.7 The spatial distribution of CR protons as a function of cylindrical galacto-centric coordinates *R* and *z* at 10 GeV. The map was computed with DRAGON in a Plain Diffusion setup with no radial dependence of the diffusion coefficient *D* from the galacto-centric radius *R*. This CR distribution was used to compute the gamma-ray profile shown in Fig. 6.9



also the same included in that analysis. Only a little fine tuning on the normalization of the diffusion coefficient and the proton injection spectrum was applied: these changes are needed to match recently released proton data from PAMELA collaboration [20].

The model is fully compatible with most CR observables, as the reader can see in Fig. 6.11a–f. In particular, I emphasize (see Fig. 6.11a, b) that this model is compatible within 2σ with PAMELA data from \simeq 0.4 GeV to more than 1 TeV; I also show the spatial distribution of CR protons at 10 GeV in Fig. 6.7 as a function of R and z.

A little overproduction of antiprotons must be pointed out, and this is a common problem of Plain Diffusion models with high values of δ , as extensively discussed in the above (Fig. 6.8).

The CR distributions computed with DRAGON are used as input to compute the $\gamma\text{-ray}$ profile along the Galactic plane; the $\gamma\text{-ray}$ map is evaluated with GammaSky using the gas and ISRF maps mentioned in the previous Paragraph and the same X_{CO} factor used in the CR model. The gas distribution used for the γ calculations is more accurate and contains more structures than the smooth distribution used in the DRAGON model; I checked the compatibility between the two distribution and I show the result in Fig. 6.13.

The result of the GammaSky computation is shown in Fig. 6.9. It is clear from this plot that—with this kind of setup—the predicted profile is too steep compared to the observations: in the central region the model prediction overshoots the data and in the anti-center region the model is lower than the observations by several σ .

A tuning of the $X_{CO}(R)$ could help: assuming a much lower value in the bulge and a very high value at large R helps to smooth the data (as done in several previous works such as [9]). Unfortunately, as the reader can see in Fig. 6.6 (dotted line), and as we already mentioned in the previous paragraph, the gradient problem is present especially in the *emissivity profile* that is independent on the molecular gas and only traces the actual CR distribution.

So I apply our idea and I consider a profile parametrized this way

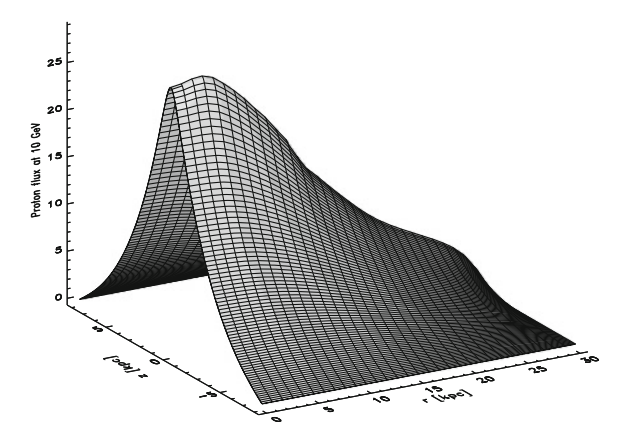


Fig. 6.8 The spatial distribution of CR protons as a function of cylindrical galacto-centric coordinates R and z at 10 GeV. The map was computed with DRAGON in a Plain Diffusion setup considering the radial variation of D from the galacto-centric radius R. This CR distribution was used to compute the gamma-ray profile shown in Fig. 6.10

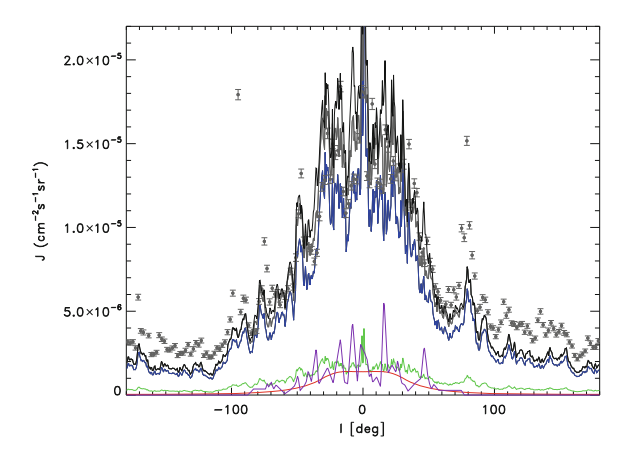


Fig. 6.9 The Gamma-ray longitudinal profile along the Galactic plane computed with GammaSky and compared to preliminary Fermi-LAT data. Integration in latitude: $-5^{\circ} < b < +5^{\circ}$. Integration in energy: $1104-1442\,\text{MeV}$. Red line IC. Green line Bremsstrahlung. Blue line π^0 decay. Purple line contribution from unresolved sources. Grey line π^0 + IC + Bremsstrahlung. Black line total. Data taken from the talk by A.W. Strong at the Workshop on Indirect Dark Matter Searches, DESY, Hamburg, June 2011 (http://www.mpe.mpg.de/ãws/talks/). The profile is computed with no radial dependence of diffusion coefficient. The gradient predicted by the model is clearly steeper than the observed one

$$D(R) \propto Q(R)^{\tau} \tag{6.6}$$

This is the parametrization already used in [18] to interpret EGRET data. From a physical point of view, it is natural—considering all that we discussed in the above—

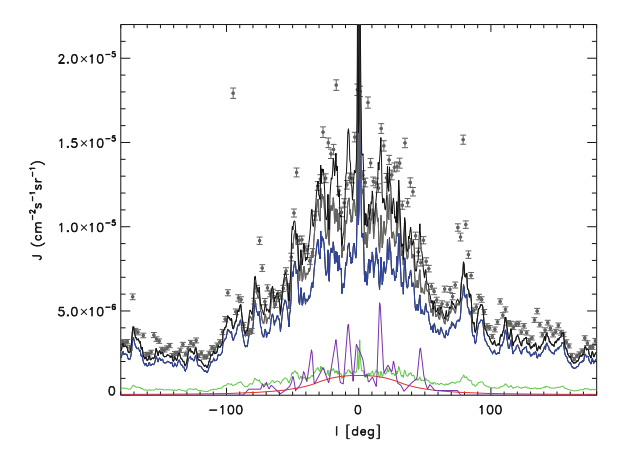


Fig. 6.10 The Gamma-ray longitudinal profile along the Galactic plane computed with Gamma-Sky and compared to preliminary Fermi-LAT data. Integration in latitude: $-5^{\circ} < b < +5^{\circ}$. Integration in energy: 1104–1442 MeV. Red line IC. Green line Bremsstrahlung. Blue line π^0 decay. Purple line contribution from unresolved sources. Grey line π^0 + IC + Bremsstrahlung. Black line total. Here the diffusion coefficient follows the source term: $D \propto Q^{\tau}$, with $\tau = 0.8$. The model shows a gradient compatible with data

to link the diffusion coefficient to the source term since the CR sources trace the regions where star formation is more active (and more turbulence is present).

The parameter τ is tuned against data: in Fig. 6.6 I show the emissivity profile for different values of τ in range [0–1]. It is evident from that figure that an increasing value of τ yields a much smoother behaviour of the emissivity as function of R. Values in the range [0.7–1] permit a good match of the data that were derived from Fermi-LAT maps [15, 16] with the method described in detail in the previous paragraph.

With this result at hand, I considered a modified version of the Plain Diffusion CR propagation setup with $D(R) = Q^{\tau}$ and $\tau = 0.8$. The smoothing in the CR distribution corresponding to such a value of τ is shown in Fig. 6.8. Noticeably, the modified model is *still compatible* with the CR observables (See Fig. 6.11a-f).

More importantly, as shown in Fig. 6.10, the γ ray profile along the Galactic plane is also nicely reproduced *with no tuning at all of the* X_{CO} . It is remarkable that a simple CR propagation setup, with only the addition of the radial dependence of D and no *ad hoc* tuning, permits to reproduce the γ -ray profile with such accuracy (Fig. 6.12).

It is also important to point out that a change of D by *less than one order of magnitude* from the Solar value to the Molecular Ring ($R \simeq 4$ –5 kpc), quite natural to expect, produces such a large effect on the γ profile: this makes us conclude that the effect is far from being negligible and must be taken into account in a propagation model (Fig. 6.13).

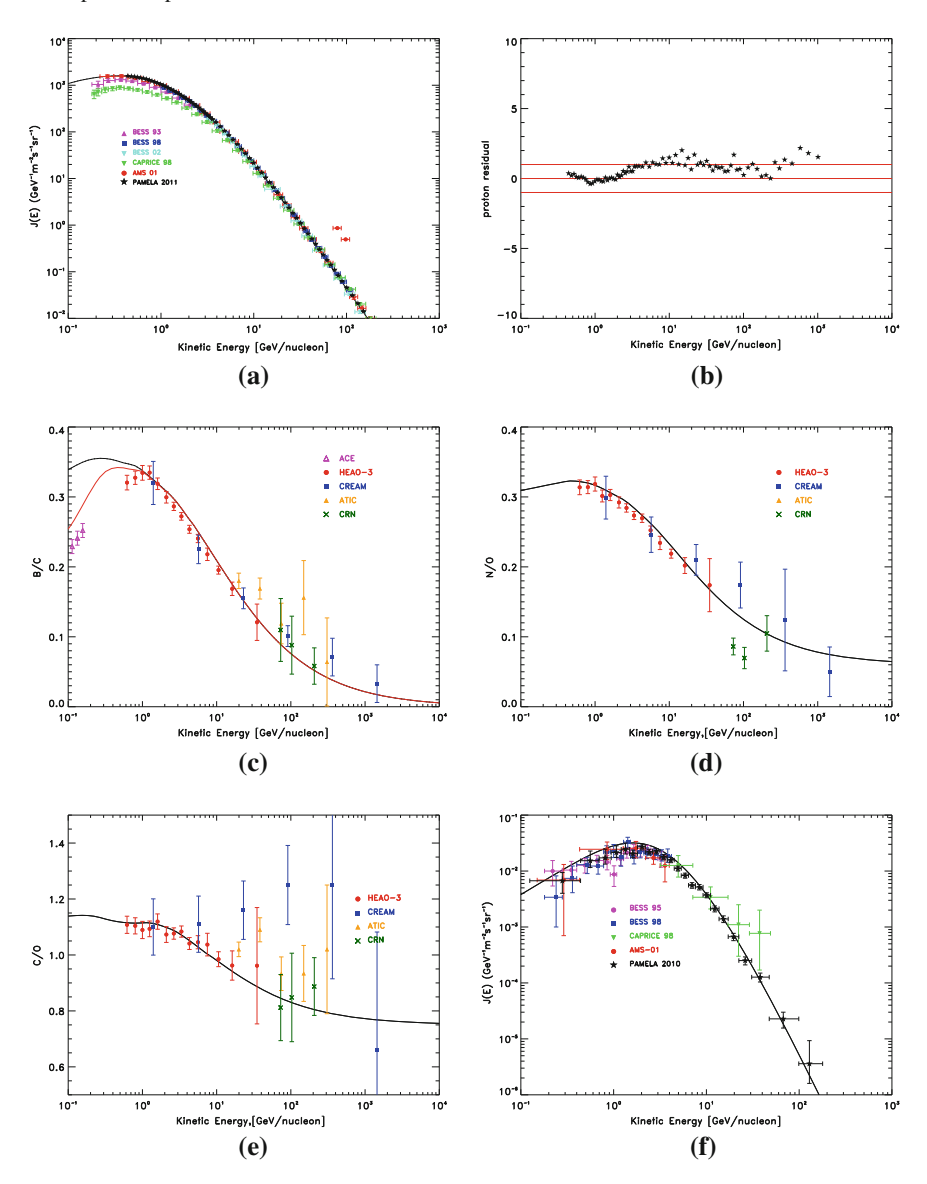


Fig. 6.11 The proton spectrum (panel \mathbf{a}), proton residuals: difference between data and theory in units of standard deviations (panel \mathbf{b}), B/C (panel \mathbf{c}), N/O (panel \mathbf{d}), C/O (panel \mathbf{e}) and antiproton spectrum (panel \mathbf{f}) computed with the Plain Diffusion model with *no spatial variation of the diffusion coefficient* (the same model used to evaluate the gamma profile shown in Fig. 6.9)

This set of *preliminary results* was partly shown in the 2011 Fermi Symposium.³ More work is needed and a more complete analysis will be performed in the

³ http://fermi.gsfc.nasa.gov/science/symposium/2011/

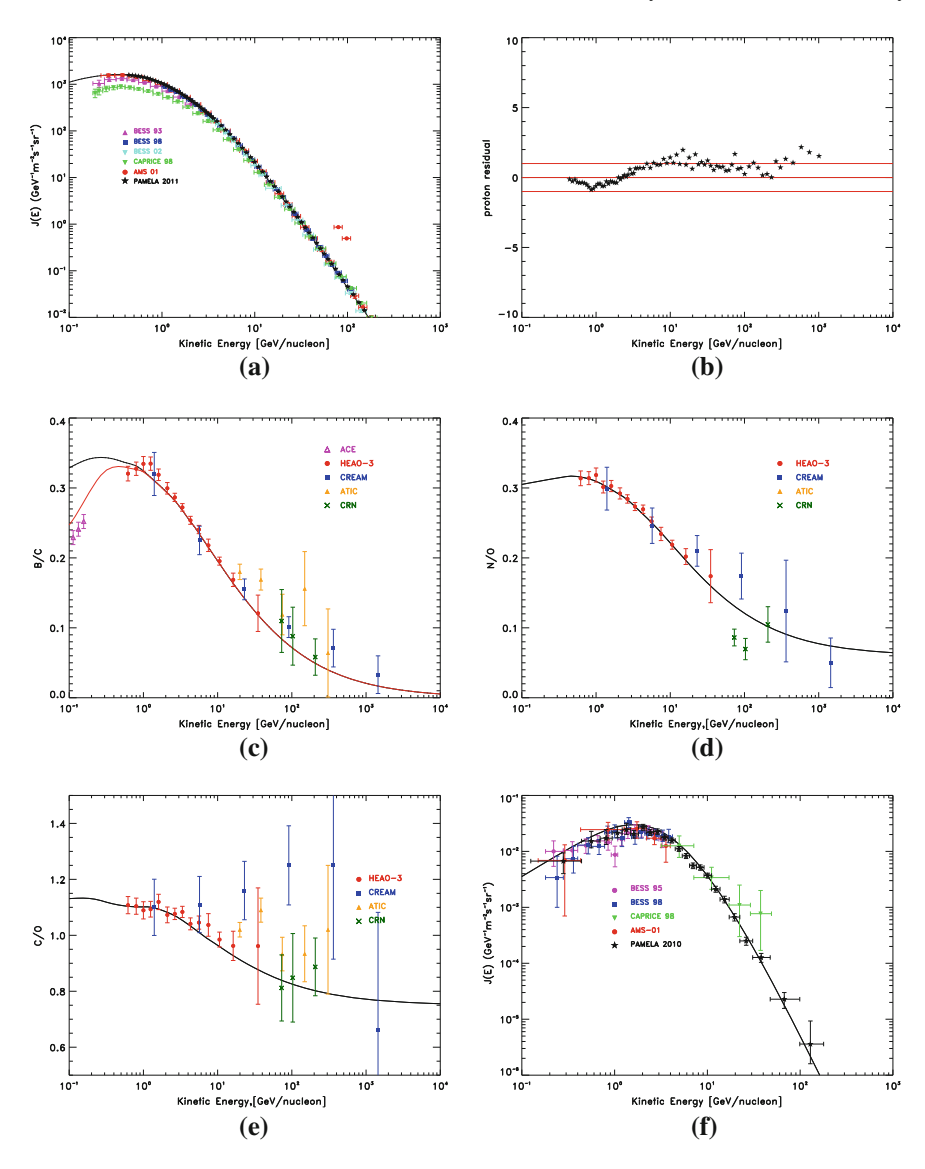


Fig. 6.12 The proton spectrum (panel **a**), proton residuals (panel **b**), B/C (panel **c**), N/O (panel **d**), C/O (panel **e**) and antiproton spectrum (panel **f**) computed with the *modified Plain Diffusion model that takes into account the radial variation of the diffusion coefficient* (the model used to reproduce the gamma-ray profile in Fig. 6.10)

future, making use of different astrophysical parameters and diffusion setups. At the moment, it is remarkable that our simple model appears to be compatible with the most important CR spectra and secondary-to-primary ratios as well as with the γ ray longitudinal profile observed by the Fermi-LAT collaboration.

References 125

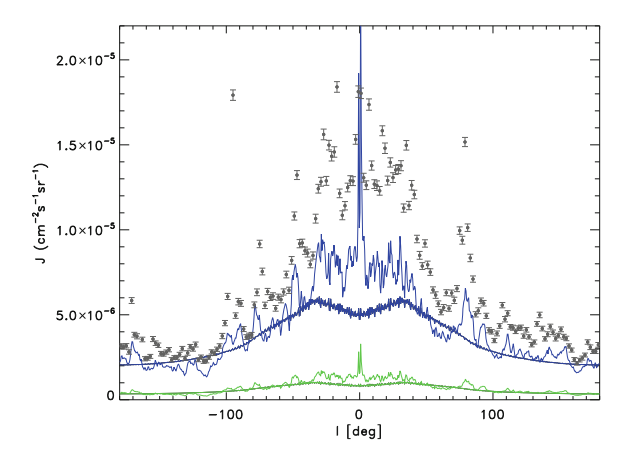


Fig. 6.13 The γ ray profile from π^0 decay computed using the Ring Model ($light\ blue$) is compared to the π^0 γ ray profile computed using the smooth gas distribution used in the DRAGON run ($dark\ blue$). The same comparison is shown for the Bremsstrahlung contribution to the γ profile ($green/dark\ green$). This ckeck is required to see if the gas model implemented in DRAGON ans used to compute the CR distributions is compatible with the model implemented in GammaSky and used to compute the γ -ray map using the CR distributions as inputs

References

- I.V. Moskalenko, A.W. Strong, Production and propagation of cosmic-ray positrons and electrons. Astrophys. J. 493, 694 (1998)
- A.W. Strong, I.V. Moskalenko, O. Reimer, Diffuse continuum gamma rays from the Galaxy. Astrophys. J. 537, 763–784 (2000)
- 3. D. Grasso, L. Maccione, Sgr A East as a possible high energy neutron factory in the Galactic centre. Astropart. Phys. 24, 273–288 (2005)
- V. Cavasinni, D. Grasso, L. Maccione, TeV neutrinos from supernova remnants embedded in giant molecular clouds. Astropart. Phys. 26, 41–49 (2006)
- W.L. Kraushaar, G.W. Clark, G.P. Garmire, R. Borken, P. Higbie, V. Leong, T. Thorsos, Highenergy cosmic gamma-tay observations from the OSO-3 satellite. Astrophys. J. 177, 341 (1972)
- R.C. Hartman, D.L. Bertsch, S.D. Bloom, A.W. Chen, P. Deines-Jones, J.A. Esposito, C.E. Fichtel, D.P. Friedlander, S.D. Hunter, L.M. McDonald, P. Sreekumar, D.J. Thompson, B.B. Jones, Y.C. Lin, P.F. Michelson, P.L. Nolan, W.F. Tompkins, G. Kanbach, H.A. Mayer-Hasselwander, A. Mücke, M. Pohl, O. Reimer, D.A. Kniffen, E.J. Schneid, C. von Montigny, R. Mukherjee, B.L. Dingus, The third EGRET catalog of high-energy gamma-ray sources. Astrophys. J. Suppl. Ser. 123, 79–202 (1999)
- S.D. Hunter, D.L. Bertsch, J.R. Catelli, T.M. Dame, S.W. Digel, B.L. Dingus, J.A. Esposito, C.E. Fichtel, R.C. Hartman, G. Kanbach, D.A. Kniffen, Y.C. Lin, H.A. Mayer-Hasselwander, P.F. Michelson, C. von Montigny, R. Mukherjee, P.L. Nolan, E. Schneid, P. Sreekumar, P. Thaddeus, D.J. Thompson, EGRET observations of the diffuse gamma-ray emission from the Galactic plane. Astrophys. J. 481, 205 (1997)
- A.W. Strong, I.V. Moskalenko, O. Reimer, Diffuse Galactic continuum gamma rays: a model compatible with EGRET data and cosmic-ray measurements. Astrophys. J. 613, 962–976 (2004)

- A.W. Strong, I.V. Moskalenko, O. Reimer, S. Digel, R. Diehl, The distribution of cosmicray sources in the Galaxy, gamma-rays and the gradient in the CO-to-H2 relation. Astron. Astrophys. 422, L47–L50 (2004)
- 10. F.P. Israel, H2 and its relation to CO in the LMC and other magellanic irregular galaxies. Astron. Astrophys. **328**, 471–482 (1997)
- F.P. Israel, Extragalactic H2 and Its Variable Relation to CO. In *Molecular Hydrogen in Space*, ed. by F. Combes, G. Pineau Des Forets (Cambridge University Press, Cambridge, 2000), p. 293
- 12. W.B. Atwood et al., [Fermi Collaboration]. The large area telescope on the Fermi gamma-ray space telescope mission. Astrophys. J. **697**, 1071–1102 (2009)
- A.A. Abdo et al. [Fermi Collaboration]. Fermi large area telescope first source catalog. Astrophys. J. Suppl. 188, 405–436 (2010)
- A.A. Abdo et al., [Fermi Collaboration]. Fermi large area telescope measurements of the diffuse gamma-ray emission at intermediate Galactic latitudes. Phys. Rev. Lett. 103(25), 251101 (2009)
- M. Ackermann et al., [Fermi Collaboration]. Constraints on the cosmic-ray density gradient beyond the solar circle from Fermi gamma-ray observations of the third Galactic quadrant. Astrophys. J. 726, 81 (2011)
- A.A. Abdo et al., [Fermi Collaboration]. Fermi observations of Cassiopeia and Cepheus: diffuse gamma-ray emission in the outer Galaxy. Astrophys. J. 710, 133–149 (2010)
- 17. T.M. Dame, D. Hartmann, P. Thaddeus, The Milky way in molecular Clouds: a new complete CO survey. Astrophys. J. **547**, 792–813 (2001)
- C. Evoli, D. Gaggero, D. Grasso, L. Maccione, Cosmic ray nuclei, antiprotons and gamma rays in the Galaxy: a new diffusion model. J. Cosmol. Astropart. Phys. 10, 18 (2008)
- 19. T.A. Porter, A.W. Strong, A new estimate of the Galactic interstellar radiation field between 0.1 um and 1000 um. In *Proceeding of the International Cosmic Ray Conference*, Pune, August 2005. Vol. 4, p. 77
- 20. O. Adriani et al., [PAMELA Collaboration]. PAMELA measurements of cosmic-ray proton and Helium spectra. Science **332**, 69 (2011)

Chapter 7 Conclusions and Future Plans

The past three years were very exciting in the field of Cosmic Ray physics: the interesting measurements by ATIC and PAMELA collaborations triggered a hot debate on possible new sources of electrons and positrons, and called for a careful modelization of both the "conventional" CR production and propagation and of the possible "extra" components of astrophysical or exotic nature; in particular the possibility that CR spectra could bring a signature of Dark Matter annihilation or decay fascinated the scientific community and was investigated by a large number of authors.

The Fermi-LAT experiment had a crucial role in this context: this cosmic observatory provided the most accurate ever view of the γ ray sky and, from the charged CRs point of view, a systematic-limited measure of unprecedented accuracy of the electron+positron spectrum from the GeV to the TeV region.

In this very stimulating period I was involved in several projects related to the interpretations of these data.

I contributed to the development and testing of a new numerical package that calculates the propagation of the most relevant CR species through the Galaxy. This code is called DRAGON and is now public and available online. Our code is written in C++ and takes fully advantage of the benefits offered by object-oriented programming: it is very easy to expand and interface with other programs and performs very quickly. DRAGON is designed to solve numerically a diffusion-loss equation starting from the heavier nucleus down to protons and to electrons/positrons; for each particle the contribution due to spallation from heavier species is considered, and many physical effects are taken into account (energy losses, reacceleration, convection). It was extensively tested against existing codes (namely GalProp) and found to reproduce the same results if the same astrophysical inputs are inserted.

We used DRAGON to perform a maximum likelihood analysis on recently released data on both light nuclei ratios and antiprotons. It was the first analysis of this kind that used a numerical code and it followed a different approach with respect to previous works present in the Literature: it exploited the recently released

¹ http://www.desy.de/~maccione/DRAGON/

high-energy B/C and antiproton data by CREAM and PAMELA and permitted to restrict the number of physical effects involved and to investigate the propagation-related parameters, in particular the energy dependence of the diffusion coefficient δ . We found that the joint analysis on B/C and \bar{p}/p ratios points toward $\delta \simeq 0.5$ and a moderate reacceleration. This value of δ corresponds, in the quasi-linear theory, to a Kraichnan-like turbulence cascade in the Interstellar Medium, although recent works on non-linear turbulence found that also a Kolmogorov turbulence may give rise to such an exponent. Noticeably our best-fit model permits to reproduce all observed light nuclei ratio and the absolute antiproton spectrum measured by PAMELA with no need to adopt a spectral break in the injection spectrum. In order to fit sub-GeV B/C data we needed to tune the rigidity dependence of the diffusion coefficient; this method was already adopted in previous works and may find a physical motivation in non-linear interplay between CRs and MHD turbulence.

In the near future AMS experiment will provide even more accurate data on light nuclei and antiprotons, and, more importantly, will expand the energy range and explore the TeV region. Our technique will be suitable for a new dedicated analysis and will permit to put more stringent constraints on the propagation parameters. Our energy-dependent method will allow to disentangle low-energy effects (convention, solar modulation) from pure diffusion and will permit to better exploit the new AMS high energy data.

Moreover, we plan to investigate more deeply the systematic uncertainties involved in this kind of analysis, in particular the influence of the astrophysical inputs (gas and source distribution, interstellar radiation field) on the results.

On the leptonic side, I worked within the Fermi-LAT collaboration on the interpretation of electron and positron data and actively contributed to the Fermi-LAT publications on the electrons.

We released two interpretative papers in which both Fermi-LAT $e^+ + e^-$ spectrum and the positron ratio by PAMELA were reproduced in a consistent scenario based on a conventional component (in which electrons are accelerated in the SNRs and positrons are entirely of secondary origin) plus an extra component with a harder spectrum and an exponential cutoff arount the TeV.

The nature of these extra sources was investigated and we found that known nearby middle-aged pulsars could be considered as natural candidates. We considered the pulsars listed in the ATNF database, we assumed that—as theoretical arguments suggest—they are $e^+ + e^-$ pair emitters and we treated analitically the propagation of the emitted pairs in the nearby ISM. We performed several analyses varying the parameters involved (efficiency, spectral index, cutoff) and the propagation setup and found our results to be quite robust. Of course an exotic scenario in which the excess with respect to the conventional component is due to annihilation or decay of Dark Matter particles is still viable (and we showed some possible DM models that fit the Fermi dataset), although for several reasons it appeared less natural to us. In particular the absence of an unexplained excess in the antiproton data forces to consider *leptophilic* models, i.e. models in which DM particles only annihilate into leptons; moreover, in order to reproduce the data, higher values of the annihilation cross section are required than expected from theory. More recently, some analyses

have shown that the inclusion of electroweak corrections can be very relevant for DM models: if these effects are taken into account, all stable particles (including antiprotons) are present in the final spectrum, independently of the primary annihilation/decay channel: this poses a tough challenge to leptophilic models.

We discussed in detail how these scenarios, together with other possible interpretations (secondary production in the accelerator, role of nearby structures such as Galactic arms etc.), can be disentangled. In particular we found that the CR electron anisotropy can be an interesting probe for the pulsar scenario, since—under favourable conditions—it predicts an observable anisotropy of order $\sim\!\!1\%$ in the direction of nearby middle-aged pulsars such as Monogem and Geminga. Currently Fermi-LAT collaboration only released upper limits on anisotropy, and we checked the compatibility of our models with these limits.

Very recently Fermi-LAT confirmed the rise of the positron fraction with energy observed by PAMELA. This is a very important result, and it strengthened the evidence for the presence of a primary source of positrons in the nearby interstellar medium. Noticeably, the preliminary absolute electron and positron spectra measured by Fermi-LAT are consistent with the models we developed previously to interpret the $e^+ + e^-$ spectrum.

In the future AMS experiment will provide very accurate measurements of the $e^+/(e^++e^-)$ ratio so a new effort will be required to interpret these data.

In order to provide the most accurate interpretation of these forthcoming data we are working to develop our code and calculate CR propagation in 3D (so far nearly all calculations assumed a cylindrical symmetry so the propagation was computed in R and z). This will allow to consider and implement more realistic models for the source and gas distribution, and to study with precision the effects of the Galactic arms and other structures on our findings.

All interpretative scenarios should fit into a multi-messenger framework.

In fact, both γ ray and synchrotron maps and spectra provide useful information and give the unique opportunity to study the distribution of Cosmic Rays through the Galaxy, a task that is not possible if one only looks at the CR spectra observed at the Solar System position.

Fermi-LAT has again a key role in this field since its γ ray maps are the most accurate ever and permitted to have an impressively deep insight on the high energy sky. In particular we were interested on Fermi results on *diffuse emission*: Fermi did not confirm the existence of the GeV excess reported by EGRET and the mid-latitude spectra were found to be consistend with numerical models prediction; instead, it confirmed the presence of the Gradient problem, i.e. the discrepancy between the observed γ emissivity longitude gradient through the Galaxy and the expected one based on the source distribution taken from SNR and pulsar catalogues.

We attacked this problem from a different point of view. DRAGON permits to compute CR propagation with a spatial dependent diffusion coefficient and our GammaSky code permits to compute γ ray maps including all known effects (π^0 decay, Inverse Compton, Bremsstrahlung). So we considered the previously unexplored hypothesis that a spatially varying diffusion coefficient could help to solve the problem. In fact, from a physical point of view, it is reasonable to assume that

the turbulence level—and therefore the effectiveness of diffusion perpendicularly to the regular magnetic field—is higher in regions where star formation is more active: this may favour the CR escape in the vertical direction, since the regular field is mainly oriented along the galactic plane, and smooth the gradient. We successfully applied this idea for the first time in 2008 to EGRET data and I showed that also Fermi-LAT data are consistently matched in this way. Noticeably, a scenario with a diffusion coefficient that follows the CR source term permits to reproduce the correct γ gradient and is also consistent with all other CR observables.

In the future we plan to go on with this work that is still in progress and to analyse the whole γ sky to see if our models match Fermi-LAT observations.

On the synchrotron side, we also plan to do some work to see if these maps may allow to infer interesting constraints on CR electron and positron propagation models. Synchrotron and γ maps are useful tools and may bring interesting features that reveal exotic or new astrophysical effects. In particular, in Synchrotron a spherical haze has been observed by WMAP and was argued to indicate the on-going annihilation of Dark Matter; on the γ side, Fermi reported the existence of two lobes ("Fermi bubbles") of unpredicted emission symmetric with respect to the Galactic center. The nature of these features remain unknown and we plan to investigate these emissions in the future.

Appendix A The Diffusion Equation in Cylindrical Coordinates

The starting point is a diffusion equation of this kind:

$$\frac{\partial f}{\partial t} = \frac{\partial}{\partial x_i} D_{ij} \frac{\partial f}{\partial x_i} = \frac{\partial}{\partial x_i} J_i \tag{A.1}$$

where D_{ij} is the diffusion tensor and we introduced the flux J_i .

We want to write the equation in cylindrical coordinates. The gradient in these coordinates is:

$$\frac{\partial}{\partial x_i} = \left(\frac{\partial}{\partial r}\hat{r}, \frac{\partial}{r\partial \phi}\hat{\phi}, \frac{\partial}{\partial z}\hat{z}\right) \tag{A.2}$$

It is convenient to decompose the diffusion tensor (neglecting anti-symmetric terms that are relevant at higher energies) in this way:

$$D_{ij} \equiv (D_{\parallel} - D_{\perp})b_i b_j + D_{\perp} \delta_{ij} \tag{A.3}$$

where b_i are the components of the regular magnetic field.

So the three components of the flux J_i become:

$$\begin{split} J_{r} &= D_{rr} \frac{\partial}{\partial r} f + D_{r\phi} \frac{\partial}{r \partial \phi} f + D_{rz} \frac{\partial}{\partial z} f \\ &= \left[(D_{\parallel} - D_{\perp}) b_{r}^{2} + D_{\perp} \right] \frac{\partial}{\partial r} f \\ &+ \left[(D_{\parallel} - D_{\perp}) b_{r} b_{\phi} \right] \frac{\partial}{r \partial \phi} f \\ &+ \left[(D_{\parallel} - D_{\perp}) b_{r} b_{z} \right] \frac{\partial}{\partial z} f \end{split} \tag{A.4}$$

$$J_{\phi} = D_{\phi r} \frac{\partial}{\partial r} f + D_{\phi \phi} \frac{\partial}{r \partial \phi} f + D_{\phi z} \frac{\partial}{\partial z} f$$

$$= \left[(D_{\parallel} - D_{\perp}) b_{\phi} b_{r} \right] \frac{\partial}{\partial r} f$$

$$+ \left[(D_{\parallel} - D_{\perp}) b_{\phi}^{2} + D_{\perp} \right] \frac{\partial}{r \partial \phi} f$$

$$+ \left[(D_{\parallel} - D_{\perp}) b_{\phi} b_{z} \right] \frac{\partial}{\partial z} f$$
(A.5)

$$J_{z} = D_{zr} \frac{\partial}{\partial r} f + D_{z\phi} \frac{\partial}{r \partial \phi} f + D_{zz} \frac{\partial}{\partial z} f$$

$$= \left[(D_{\parallel} - D_{\perp}) b_{z} b_{r} \right] \frac{\partial}{\partial r} f$$

$$+ \left[(D_{\parallel} - D_{\perp}) b_{z} b_{\phi} \right] \frac{\partial}{r \partial \phi} f$$

$$+ \left[(D_{\parallel} - D_{\perp}) b_{z}^{2} + D_{\perp} \right] \frac{\partial}{\partial z} f$$
(A.6)

It is clear at this point why we called D_{\parallel} and D_{\perp} the components of the diffusion tensor.

For example, if one assumes that the regular field is directed along $\hat{\phi}$, then the components are $(b_r, b_\phi b_z) = (0, 1, 0)$ and the flux becomes:

$$J_{r} = D_{\perp} \frac{\partial}{\partial r} f$$

$$J_{\phi} = D_{\parallel} \frac{\partial}{r \partial \phi} f$$

$$J_{z} = D_{\perp} \frac{\partial}{\partial z} f$$
(A.7)

So the meaning of D_{\parallel} and D_{\perp} as diffusion coefficients in the parallel and perpendicular direction with respect to the regular magnetic field is evident.

Coming back to the general case, in order to write the diffusion equation in cylindrical coordinates it is necessary to compute the divergence of \vec{J} :

$$\frac{\partial}{\partial x_i} J_i = \frac{1}{r} \partial_r (r J_r) + \frac{1}{r} \partial_\phi (J_\phi) + \partial_z J_z \tag{A.8}$$

Using the expression calculated above for J_i the diffusion equation becomes:

$$\begin{split} \frac{\partial f}{\partial t} &= \frac{1}{r} \partial_r \left[(D_{\parallel} - D_{\perp}) r b_r^2 \partial_r + r D_{\perp} \partial_r + (D_{\parallel} - D_{\perp}) r b_r b_{\phi} \partial_{\phi} + (D_{\parallel} - D_{\perp}) r b_r b_z \partial_z \right] \\ &\quad + \frac{1}{r} \partial_{\phi} \left[(D_{\parallel} - D_{\perp}) b_{\phi} b_r \partial_r + (D_{\parallel} - D_{\perp}) b_{\phi}^2 (1/r) \partial_{\phi} + D_{\perp} (1/r) \partial_{\phi} + (D_{\parallel} - D_{\perp}) b_{\phi} b_z \partial_z \right] \\ &\quad + \partial_z \left[(D_{\parallel} - D_{\perp}) b_z b_r \partial_r + (D_{\parallel} - D_{\perp}) b_z b_{\phi} \partial_{\phi} + (D_{\parallel} - D_{\perp}) b_z^2 \partial_z + D_{\perp} \partial_z \right] \end{split} \tag{A.9}$$

Now we can do some approximations: (1) assume cylindrical symmetry (i.e. $\partial_{\phi} = 0$) and (2) assume a regular field directed along $\hat{\phi}$ (i.e. $(b_r, b_{\phi} b_z) = (0, 1, 0)$). With simple calculations Eq. (A.9) simplifies to:

$$\frac{\partial f(r,z,p)}{\partial t} = \phi \frac{\partial f}{\partial r} + \psi \frac{\partial f}{\partial z} + \alpha \frac{\partial^2 f}{\partial r^2} + \beta \frac{\partial^2 f}{\partial z^2} + \frac{1}{p^2} \frac{\partial}{\partial p} p^2 D_{pp} \frac{\partial}{\partial p} f_0 + Q$$
(A.10)

where $\alpha=\beta=D_\perp, \phi=\frac{1}{r}D_\perp+\frac{\partial D_\perp}{\partial r}$ and $\psi=\frac{\partial D_\perp}{\partial z}$.

Appendix B DRAGON Code: A Description

DRAGON is designed to compute in a very efficient way the solution of the CR diffusion-loss equation for all desired nuclear and leptonic species. The physics involved in this project is described in detail in Chap. 2 of this thesis. Here we want to describe technically the architecture of the code.

DRAGON consists of 34 C++ classes. Here is a short description of the most relevant ones. For a detailed list of all classes, method and attributes I refer to the DRAGON documentation page.

- The main class is itself called DRAGON; the constructor of this class takes care of reading user input and settings, creating the galactic structure (stored in a object of type Galaxy called gal), initializing the algorithm to solve the diffusion equation (or the vector of algorithms, if the user has selected more than one), and creating the structure to contain the propagated nuclear densities and the output. The input parameters are mostly contained in a file called constants.h, although the most important ones (resolution, normalization and energy dependence of diffusion coefficient, halo height, Alfvén velocity, convective velocity, etc.) are passed to the program via command line. This permits to create rapidly shell scripts that execute large number of runs varying the most relevant parameters involved in CR propagation.
- The class Galaxy contains important information about the galactic properties, e.g. a map associating to each nucleus its corresponding injection index, a map associating to each nucleus its corresponding source abundance, the spatial distribution and energy spectrum of the source term and diffusion coefficient, and so on; as usual in good C++ programming, in this class, as well as the other ones, the data are stored in *protected attributes* and the access to them is guaranteed via appropriate methods, i.e. Galaxy::GetDiffCoeff() or Galaxy::GetSource().
- The class TParticle is the prototype of how the properties of a nucleus, its spatial distribution and energy spectrum are described in DRAGON: the protected attributes of this class contain mass and charge, a unique ID computed from

them, the distribution in physical space and in momentum which has to be found after propagation, stored in the vector density, and other properties.

- TCREvolutorBasis is the class that defines all the methods needed to solve the transport equation. The structure of the code allows to use several algorithm in cascade, and each of them is implemented in a derived class that inherits from TCREvolutorBasis the main methods. For example, in TCREvolutor the fast GalProp-like Operator Splitting method with Cranck—Nicholson scheme is implemented: it permits to obtain very quickly a decent approximation to the solution; the more reliable, but slower, ADI version of this method is implemented instead in TCREvolutorADI.
- TXSecBase is the abstract class that describe spallation cross sections. It provides basic routines such as GetXSec(int,int,int,int) that can used to obtain the value of the spallation cross section of a heavy nucleus characterized by atomic mass and number (iA, iZ) on IS gas that produces a lighter nucleus (jA, jZ). Various cross section models may be implemented. We considered the GalProp cross section database and the alternative Webber model. Each model is implemented in a derived class that inherits from TXsecBase the basic methods.
- TSpallationNetwork provides the complete network of spallation used to compute secondary CR source terms. The most important attribute implemented in this class is map< pair< int, int >, vector< double > > TSpallationNetwork::spall, i.e. a map that associates to a pair (parent heavy nucleus—light product) the vector of spallation cross section as a function of energy. An instance of this class is associated as an attribute to each TParticle object, and it contains all the spallation cross sections from nuclei heavier than the current one.

Now let us see how these class interact with each other and what happens when a run of DRAGON starts.

At the beginning, an instance of DRAGON class is created and all the initializations described above are performed by the class constructor; Moreover, a list of nuclei is created and ordered properly from the heavier to the lightest.

Then, the method DRAGON::Run() is called and the main cycle starts:

```
for (vector<int>::iterator inuc = list_nuc.begin(); inuc != list_nuc.end(); ++inuc) {
    (...)
    cout << "Starting with nucleus A = " << A << " Z = " << Z << endl;
    cout << "Starting propagation..." << endl;
    (...)

DECMODE decay_mode = list->GetDecayMode(*inuc);
    double life = list->GetLifeTime(*inuc);
    if (decay_mode != STABLE) cout << "Lifetime = " << life/year << " y" << endl;
    else cout << "Stable nucleus" << endl;
    if (decay_mode == EC) cout << "Nucleus may attach an electron and decay via EC" << endl;
    (...)
    particles.push_back(new TParticle(A, Z, gal, in, prev_uid, xsecmodel, list, 0));
    particles.back()->Evolve(particles, alg, spallnet, xsecmodel);
}
```

As the reader can see from this portion of code, a vector called particles is created and filled with pointers to instances of TParticle.

For each object of particles the method Particle::Evolve() is called.

The main tasks of Particle::Evolve() are the following:

• Invoke the method TParticle::ComputeSecondarySource that computes the source term coming from spallation from heavier nuclei for each position and energy of the grid. This routine makes use of the previously propagated particles contained in the vector particles. The most important portion of code involved in this computation is:

```
for(vector<TParticle*>::iterator ipart=part.begin();ipart!=part.end()-1;++ipart) {
  vector<double> spall_spectrum( spnet->GetXSec( (*ipart)->GetUid(), uid ) );
  if (spall_spectrum.size() == dimE || (*ipart)->GetDaughter() == uid) {
    for (int k = 0; k < dimr; ++k) {
      for (int 1 = 0; 1 < dimz; ++1) {
        int indspat = coord->index(k,1);
        double Afactorgasdensity = Afactor*totalgas->GetGas(indspat);
        for (int i = 0; i < dimE; ++i) {
          int ind = indspat*dimE+i;
          if (spall_spectrum.size() == dimE)
          result[ind]+=Afactorgasdensity*spall_spectrum[i]*(*ipart)->GetDensity(ind);
           // (spallation)
          if ((*ipart)->GetDaughter() == uid)
           result[ind] += (*ipart) -> GetDensity(ind) / (*ipart) -> GetLifetime() / gamma[i];
           // (decay)
       }
     }
   }
 }
}
```

In this portion of code the object spnet, instance of the class TSpallationNetwork associated to the particle is used: this object contains all the spallation cross sections, that are accessible through the routine GetXSec. Making use of these data, the source term is stored in the vector result.

• Call the routine TCREvolutor::Run() and/or TCREvolutorADI:: Run() according to which algorithm or set of algorithms is selected by the user (this setting can be modified in constants.h). The standard case is the GalProp-like Operator Splitting implemented in TCREvolutor. That I will now describe in detail.

The method TCREvolutor::Run() is the heart of the code: it contains the actual solution of the matricial problem. (If the user has selected the ADI method, the corresponding routine is of course TCREvolutorADI::Run()).

The relevant parts are the following:

```
while (dt > dtmin) {
  dtbar = dt/p;
  halfdtbar = 0.5*dtbar;
  halfdt = 0.5*dt;
  halfdtdperpfactor = halfdt*dperpfactor;
  for (int Niter = 0; Niter < Nrept; ++Niter) {</pre>
```

This portion of the code shows how the algorithm is structured.

For each Δt , starting from the longer one, the code computes a number (Nrept) of time steps; at the end of a set of time steps the Δt is halved, and the process goes on until the minimum Δt is reached. This method permits to take care in a proper way of all the physical processes that are involved in CR propagation (energy losses, reacceleration...), each one with its own different time scale.

```
// Here propagation in Z direction starts.
for (int k = 0; k < dimE; k++) {
  (\ldots)
 for (int j = 0; j < dimr-1; j++) {
   for (int i = 0; i < dimz; i++) {
   (\ldots)
   uodzz[i] = halfdtcoeffrdp - halfdtdperpfactorpsi - vCi1;
   lodzz[i] = halfdtcoeffrdp + halfdtdperpfactorpsi - vC1i;
   dzz[i] = 1.0 + dtbarcoeffrdptotgalxsecklifetime;
   Rzz[i] = N[ind] * (1.0 - dtbarcoeffrdptotgalxsecklifetime)
    + source->GetSource(indspat)*dtbarinjfactorspeck
    + dtbar*SecSource_[ind];
   if (i < dimz-1) Rzz[i] -= N[ind+dimE] * uodzz[i] ;</pre>
   if (i > 0) Rzz[i] -= N[ind-dimE] * lodzz[i];
   // **************
   Utility::solve_tridag(lodzz, dzz, uodzz, Rzz, yy);
   // **************
   for (int i = dimz-2; i > 0; --i) {
     value = yy[i];
     N[index(j,i,k)] = (value > 0) ? value : 0.0;
 } //for j
} //for k
```

Here the OS scheme has started. The time step is subdivided in three substeps. The first corresponds to propagation in z direction. As we discussed in Chap. 3, the discretization of the equation leads to a tridiagonal matricial problem. The main diagonal, upper and lower diagonals are stored in vectors dzz, uodzz and lodzz; the routine $Utility::solve_tridag()$ does the necessary computations.

In the following portion the reader can see how the terms involving momentum derivatives (reacceleration + loss) and propagation along r are treated:

```
// Here propagation in Momentum direction starts: Reacceleration and/or energy losses
for (int i = 0; i < dimr-1; i++) {
 for (int j = 1; j < dimz-1; j++) {
   Utility::solve_tridag(oded, de, odeu, Re, ee);
   for (int k = 0; k < dimE; k++) {
     value = ee[k];
     N[ind+k] = (value > 0) ? value : 0.0;
 }
// Here propagation in R direction starts.
for (int k = 0; k < dimE; k++) {
 (...)
 for (int j = 1; j < dimz-1; j++) {
   for (int i = 0; i < dimr; i++) {
     drr[i] = 1.0 + dtbarcoeffzdpgaslifetime;
     if (i == 0) uodrr[i] = -2.0*halfdtcoeffzdp; // i == 0, Symmetry condition at R = 0
     else uodrr[i] = -halfdtcoeffzdp - halfdtdperpfactorphi;
     lodrr[i] = -halfdtcoeffzdp + halfdtdperpfactorphi;
     Rrr[i] = N[ind] * (1.0-dtbarcoeffzdpgaslifetime)
       + source->GetSource(indspat)*dtbarinjfactorspeck
        + dtbar*SecSource_[ind];
     if (i < dimr-1) Rrr[i] -= N[ind+dimE*dimz]*uodrr[i];</pre>
     if (i > 0) Rrr[i] -= N[ind-dimE*dimz]*lodrr[i];
   Utility::solve_tridag(lodrr, drr, uodrr, Rrr, xx);
   for (int i = dimr-2; i >= 0; --i) {
     value = xx[i];
     N[index(i,j,k)] = (value > 0) ? value : 0.0;
 }
}
         } // for Niter
         dt *= dtfactor;
       } // while (dt > dtmin)
```

Once the propagation has terminated, the output, consisting in the CR density as a function of energy and position for each nucleus, (stored in the vector density, protected attribute of each TParticle object) is written to disk.

The output consists in two FITS files.

The FITS format is nowadays a standard as far as astrophysical and astronomical data are concerned: the major feature is that it makes possible to store metadata in one or more human-readable ASCII *headers*, so that an interested user can just examine them to investigate a file of unknown provenance.

A FITS file is composed of a sequence of *Header Data Units* (HDUs). Each HDU has a header that contains keyword = value statements describing size, format and structure of the data; the data follow, organized as the header specifies.

The first file that DRAGON creates is written by the routine TParticle:: Print() and prints in a different HDU all the information relevant to each nucleus: in the header the user can find charge, mass, source abundance, injection spectrum and other information; in the data block the propagated density is stored for each momentum of the p grid and each position (r,z) in the Galaxy.

The second output file is created by the routine TParticle:: PrintSpectrum() and stores the same information, but related to Sun position only. The corresponding FITS file is of course much smaller and suitable for fast reading of data and quick plotting by external procedures, e.g. IDL or MATLAB routines.

We recently added in the code a new feature: the possibility to consider the K capture. This process is treated like in GalProp. A nucleus that may decay via K capture¹ is propagated twice:

- First the "bare" nucleus is propagated with an infinite lifetime (if the cosmic ray has no electrons at all it can't decay via electron capture) and a loss term due to the possible transformation—via interaction with interstellar gas—into a "dressed" nucleus;
- Then the "dressed" nucleus—i.e. the nucleus that attached an electron—is propagated with finite lifetime due to the possible electron capture decay.

DRAGON is highly optimized: its architecture takes full advantage of the complexity of C++ and is therefore highly modular and easy to upgrade with new features. Memory is managed in a very efficient way: data are always passed from a routine to another through pointers, and all quantities that are function of r, z and p (source distribution, diffusion coefficient, CR density...) are not stored in multi-dimensional matrices but in vectors: this allows a very quick access to the desired location. Moreover, for all the quantities that are factorizable as independent functions of position and energy, the spatial and energy dependence is separated: so instead of using a vector with (dimr*dimz*dimE) elements we use a (dimr* dimz + dimE)-long vector. This permits to save memory and also

¹ The electron capture or K capture is the process in which a proton-rich nuclide absorbs an inner atomic electron (changing a nuclear proton to a neutron) and simultaneously emits a neutrino.

execution time because the program does not waste time allocating too many data and looking in a big vector for the desired point.

We are now planning to expand the code in several ways. In particular we are going to add the possibility to perform full three-dimensional simulation. The structure of the three-dimensional routines is already implemented, and a class TCREvolutor3D is currently under development. The 3D simulations will require to partly rewrite the algorithm since the equation and therefore the discretization is slightly altered. Moreover, we are going to organize the input in a more efficient and flexible way, making use of simple XML input files.

Appendix C Solution of the Transport Equation for a Pulsar-Like Source

We have to solve the following equation:

$$\frac{\partial N_e(E,t,\vec{r})}{\partial t} - D(E)\nabla^2 N_e - \frac{\partial}{\partial E}(b(E)N_e) = Q(E,t,\vec{r})$$
 (C.1)

where $N_e(E, t, \vec{r})$ is the number density of e^{\pm} per unit energy, D(E) is the diffusion coefficient (assumed to be spatially uniform), b(E) the rate of energy loss and $Q(E, t, \vec{r})$ the source term.

This equation describes the transport of CR electrons in absence of convection and reacceleration. Only energy-dependent spatial diffusion and energy losses are taken into account.

The source term is written this way:

$$Q(E,t,\vec{r}) = Q(E)\delta(t-t_0)\delta(\vec{r})$$
 (C.2)

This source term describe a point-source that emits a single *burst* of electrons (and positrons) in the ISM; in the equation above t_0 is the injection time (the instant in which the particles are released from the source into the ISM), and \vec{r} is the distance to the source.

The solution is (Ginzburg and Putskin [1], Atoyan et al. [2]):

$$N_e(E, t, \vec{r}) = \frac{Q(E_i)b(E_i)}{\pi^{3/2}b(E)r_{\text{diff}}^3(E, t)}e^{-(r/r_{\text{diff}}(E, t))^2}$$
(C.3)

where E_i is the initial energy of particles which are cooled down to energy E during time $t - t_0$, and r_{diff} is the diffusion distance (i.e. the propagation distance over which the electron lose half of its energy).

At this point, we need to to specify the energy dependence of the source term. We adopt a general form: a power–law with exponential cutoff:

$$Q(E, t, \vec{r}) = Q_0 \left(\frac{E}{1 \text{GeV}}\right)^{-\Gamma} e^{(-E/E_{\text{cut}})} \delta(t - t_0) \delta(\vec{r})$$
 (C.4)

D. Gaggero, Cosmic Ray Diffusion in the Galaxy and Diffuse Gamma Emission, Springer Theses, DOI: 10.1007/978-3-642-29949-0.

The energy loss rate b(E), since only syncrotron and IC losses are relevant, is expressed as $b(E) = b_0 E^2$, where $b_0 = 1.4 \times 10^{-16} \text{ GeV}^{-1} \text{s}^{-1}$ which is taken to be same as in GalProp at the Sun position.

Therefore, we obtain—in our particular case—that the solution is:

$$N_{e}(E, t, \vec{r}) = \frac{Q_{0}}{\pi^{3/2} r_{\text{diff}}^{3}} (1 - E/E_{\text{max}})^{\Gamma - 2} \left(\frac{E}{1 \text{ GeV}}\right)^{-\Gamma} e^{-\frac{E}{(1 - E/E_{\text{max}})E_{\text{cut}}}} e^{-(r/r_{\text{diff}}(E))^{2}}$$
(C.5)

for $E < E_{\text{max}}$, and 0 otherwise, where the diffusion distance is given by

$$r_{\text{diff}}(E,t) \approx 2\sqrt{D(E)(t-t_0)\frac{1-(1-E/E_{\text{max}}(t))^{1-\delta}}{(1-\delta)E/E_{\text{max}}(t)}}$$
 (C.6)

and

$$E_{\text{max}}(t) = \frac{1}{b_0(t - t_0)} \tag{C.7}$$

It should be noted that sources injecting electrons at a time t_0 with $t - t_0 \ll \tau_{\text{diff}} \simeq r^2/D(E)$ cannot contribute to the electron flux reaching the observer.

References

- V.L. Ginzburg, V.S. Ptuskin, On the origin of cosmic rays: some problems in high-energy astrophysics. Rev. Mod. Phys. 48, 161–189 (1976)
- 2. A.M. Atoyan, F.A. Aharonian, H.J. Völk, Electrons and positrons in the galactic cosmic rays. Phys. Rev. D **52**, 3265–3275 (1995)

Index

| A | G |
|----------------------------------------|-------------------------------|
| Alfvén waves, 23 | GALPROP code, 31 |
| ankle, 1 | gamma ray emission, 111 |
| ATIC experiment, 3, 64 | GeV excess, 114, 115 |
| | gradient problem, 4, 114, 115 |
| | |
| В | |
| bremsstrahlung, 112 | I |
| | interstellar gas, 10 |
| ~ | interstellar radiation |
| C | field, 2, 38 |
| confidence levels, 48 | inverse compton, 61, 112 |
| convection, 2, 32 | |
| Cosmic Ray spectrum, 1, 36 | _ |
| Cosmic Rays, 1 | J |
| Cranck-nicholson method, 30 | joint statistical nalysis, 50 |
| | |
| D | K |
| dark matter, 3, 69 | knee, 1 |
| diffusion coefficient, 25 | Rice, 1 |
| diffusion equation, 1, 24, 26, 32, 131 | |
| DRAGON code, 31, 135 | L |
| 2111001 (0000, 21, 100 | leaky box models, 22 |
| | |
| E | |
| EGRET experiment, 4, 8, 113 | M |
| electron anisotropy, 104 | magnetic field, 19 |
| energy losses, 2, 32 | modulation, 3, 38 |
| | molecular clouds, 11 |
| | |
| F | |
| Fermi acceleration, 8 | O |
| Fermi-LAT experiment, 3, 74 | operator Splitting, 33 |
| | |

146 Index

| P PAMELA experiment, 3, 64 pion decay, 111 positron excess, 65, 66 | semi-analytical models, 54 spallation, 2, 21 statistical analysis, 43 supernova remnants, 17 |
|--------------------------------------------------------------------|-------------------------------------------------------------------------------------------------------|
| pulsar, 17, 67, 83 pulsar models, 83, 143 | synchrotron radiation, 60, 111 |
| Q quasi-linear theory, 22 | T turbulence, 20 turbulence, kolmogorov spectrum, 20 turbulence, kraichnan spectrum, 21 |
| R reacceleration, 24 rotation measure, 19 | X X _{CO} , 114 |
| S secondary-to-primary ratio, 40 semi-analytical models, 29, 54 | |